Doctoral Thesis

STUDY ON KALMAN FILTERS FOR MOTION CONTROL APPLICATIONS:
DUAL-RATE – TIME-DELAY COMPENSATION – PARAMETER ESTIMATION

モーションコントロールへの応用のためのカルマンフィルタに関する研究：
デュアルレート ・ 時間遅延補償 ・ パラメータ推定

グエン ビン ミン

NGUYEN BINH MINH

Doctoral Thesis

STUDY ON KALMAN FILTERS FOR MOTION CONTROL APPLICATIONS:
DUAL-RATE – TIME-DELAY COMPENSATION – PARAMETER ESTIMATION

モーションコントロールへの応用のためのカルマンフィルタに関する研究：
デュアルレート ・ 時間遅延補償 ・ パラメータ推定

THESIS
Submitted to the Graduate School of Frontier Sciences of
The University of Tokyo
In Partial Fulfillment
Of the Requirements
For the Degree of
DOCTOR OF SCIENCE

By

NGUYEN BINH MINH
(グエン ビン ミン)

Supervisor

Professor Yoichi Hori, Ph.D.
Professor Hiroshi Fujimoto, Ph.D.

Department of Advanced Energy
THE UNIVERSITY OF TOKYO
December 2014

Acknowledgement

First of all, I want to express my deeply-felt thanks to my supervisor, Prof. Hori. I appreciate his guidance and encouragement to me so that I could find my own way of research. I would also like to thank Prof. Hori for giving me the opportunity to work in the industrial projects and practice the teaching assistant.

I would like to thank Prof. Fujimoto for not only taking care of my experiments but also giving many critical and helpful comments on my research for years.

From the bottom of my heart, I thank Prof. Ta Cao Minh for his encouragement that I decided to pursue the study in the graduate level in Japan. Thanks to Prof. Ta Cao Minh's guidance, I knew for the first time the definition of the academic works.

I would like to express my sincere thanks to Ms. Hiromori. Working as the secretary of our lab, she has kindly supported me for three years that I could focus on my study.
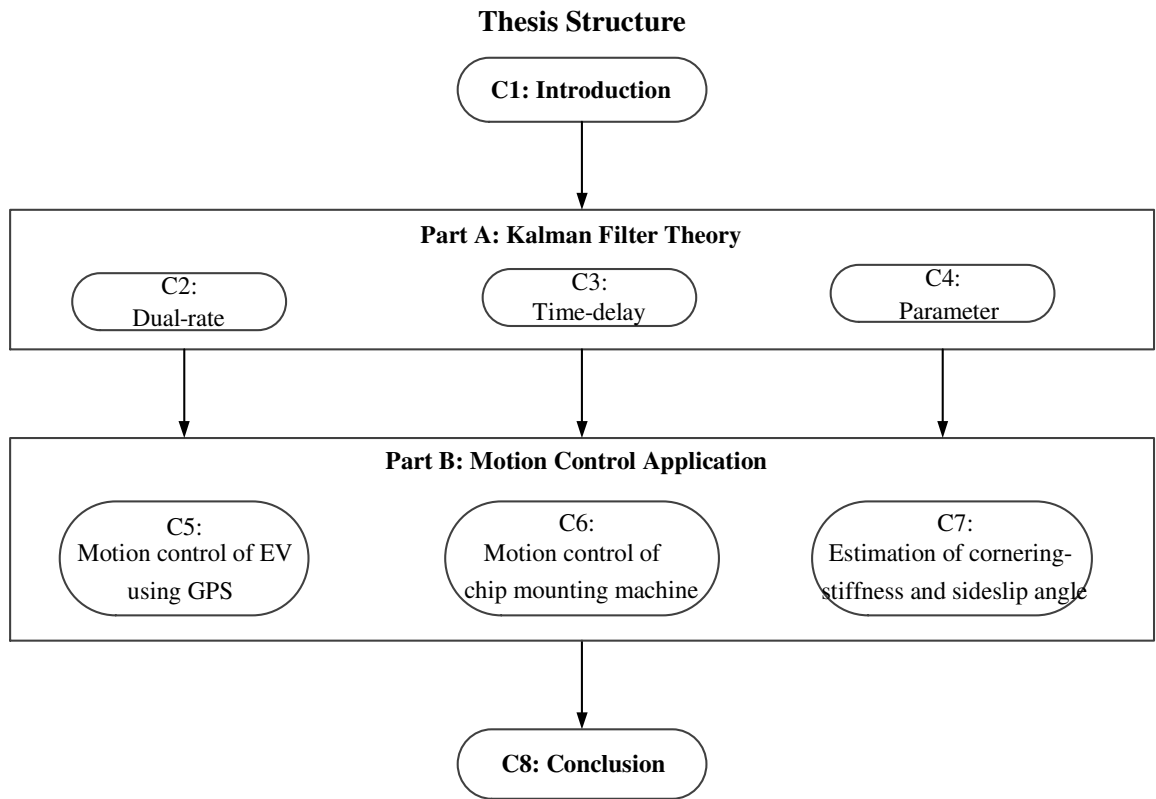
I am grateful for the supports and the friendship of my lab-mates. Without their helps, it would be so hard to finish my works. I also thank my Vietnamese friends in Kashiwa campus who gave me unforgettable memory.

I would like to thank Kobayashi International Scholarship Foundation, not only for their financial support during my PhD course, but also for organizing memorable activities and events that made my life colorful. I also appreciate the supports of Honda Foundation and Panasonic Scholarship Foundation.

I appreciate the supports of Hitachi Research Laboratory for my works in the project of visual servo system which is a useful experience for me.

Last but not least, for their emotional support and encouragement through my life, I would like to thank my family, special thanks to my mom and my wife. They always take care of me and believe in me.

Abstract

Thesis Structure

C1: Introduction

Part A: Kalman Filter Theory

C2:
Dual-rate

C3:
Time-delay

C4:
Parameter

Part B: Motion Control Application

C5:
Motion control of EV
using GPS

C6:
Motion control of
chip mounting machine

C7:
Estimation of cornering-
stiffness and sideslip angle

C8: Conclusion

The main contributions of this thesis are the developments of the dual-rate Kalman filters and the time-delay compensation Kalman filters to improve the accuracy of the state estimations for motion control applications. Besides that, we introduce the unscented Kalman filter which is a nonlinear filter algorithm for estimating the states and the parameters simultaneously. As shown in the figure of the "Thesis Structure," the thesis is organized as follows.

Chapter 1 introduces the background and the motivation of the thesis. In this chapter, the definition of motion control is presented. Then, three main problems studied in this thesis are stated.

1) *Robust estimation of dual-rate system:* In this thesis, we propose the disturbance accommodation Kalman filter to improve the robustness of dual-rate estimation in which the sampling time of the output measurement equals to multiple times of the control period.

2) *Estimation considering the large time-delay of the measurement*: Based on the upper-bound of the estimation error covariance and the μ-gains, a new algorithm for handling the large-time-delay measurement in Kalman filter is proposed.

3) *Simultaneous estimation of state and parameter*: In adaptive estimation, the parameters are estimated along with the states. To improve the estimation convergence and simplify the estimation configuration, we introduce the idea such that the parameters are also considered as the

extended states. By constructing the extension state system, the states and parameters are estimated simultaneously using the unscented Kalman filter algorithm.

Part A, including Chapter 2, Chapter 3, and Chapter 4, presents the Kalman filter theories developed and used in this thesis. Chapter 2 presents the robust dual-rate KF based on disturbance accommodation. Chapter 3 presents the Kalman filter for delayed measurement based on the upper-bound scheme. The unscented Kalman filter and the simultaneous estimation of parameter and state are introduced in Chapter 4.

Part B, including Chapter 5, Chapter 6, and Chapter 7, presents the motion control applications of the Kalman filter theories presented in Part A.

Chapter 5 presents the motion control of electric vehicle using GPS based on the robust dual-rate Kalman filter. In this system, the fusion of GPS receiver with inertia sensors is utilized to obtain the motion variable of the vehicle, such as the sideslip angle, yaw angle, velocity. Three types of motion controls of electric vehicle are demonstrated: lateral stability control, autonomous attitude control, and wheel slip-ratio control.

Chapter 6 presents the chip-mounting system in which the time-delay Kalman filter is used to fuse the delayed measurement from the image processing unit with the linear encoder measurement to estimate the position of the target. By compensating the delay and improve the update frequency of the information of the target position, accurate target tracking control is achieved.

The minor contribution of this thesis is presented in Chapter 7 in which the augmented system and the unscented Kalman filter are applied to estimate the cornering stiffness and the sideslip angle simultaneously. The key sensors used in this estimation design are the tire lateral force sensors.

Finally, the summary and the future works are given in Chapter 8.

(*A Japanese translation of the above abstract is presented in the next page*).

論 文 の 内 容 の 要 旨

　　本論文の主たる貢献はデュアルレートカルマンフィルタ及び時間遅延補償カルマンフィルタの構築によるモーションコントロールにおける状態推定の精度向上である。その他に、動的なシステムにおける状態とパラメータを同時推定する非線形アルゴリズムである無香カルマンフィルタ(Unscented Kalman Filter)についても述べる。論文の構造図に示すように、本論文の構成は以下のようになる。

　　第1章では本論文の背景と動機について紹介する。始めにモーションコントロールを定義し、本論文で解決する三つの主要問題を述べる。

　1. デュアルレート系におけるロバスト推定：本論文では、出力のサンプリング周期が制御周期の数倍となるデュアルレート推定のロバスト性改善のため Disturbance Accommodation カルマンフィルタを提案する。

　2. 測定の大幅な遅れを考慮した推定：推定誤差共分散の上界を基に、カルマンフィルタにおける測定の大幅な遅延に対応できる新たなアルゴリズムを提案する：[Upper-bound Kalman filter with the μ-gains]。

　3. パラメータと状態の同時推定：観測器・推定器と RLS 同定の組み合わせに基づく様々な推定構成が提案されてきた。推定の収束を改善し、推定構成を簡単にするために、パラメータは拡張状態とみなされるような考えを導入する。拡張状態のシステムを構築することにより、状態およびパラメータが同時に無香カルマンフィルタアルゴリズムを用いて推定される。

　　パートAに含まれる第2章・第3章・第4章では、この論文で開発し使用されるカルマンフィルタ理論を提示する。第2章では Disturbance Accommodation に基づくロバストなデュアルレートカルマンフィルタを紹介し、第3章では上界に基づく測定遅延を考慮したカルマンフィルタについて述べる。第4章では無香カルマンフィルタおよびパラメータと状態の同時推定を紹介する。

　　パートBに含まれる第5章・第6章・第7章では、パートAで示されたカルマンフィルタ理論のモーションコントロール応用を提示する。

　　第5章ではロバストなデュアルレートカルマンフィルタを利用した、GPS を搭載する電気自動車の運動制御について述べる。このシステムでは、GPS の情報を車載の諸センサの情報と融合させる事によって横滑り角、ヨー角、速度といった車両の状態を得る。

　　第6章ではチップ実装において、リニアエンコーダと測定遅延が生じる画像処理ユニットの情報を時間遅延補償カルマンフィルタを使って融合させ、目標からみた制御対象の位置を推定するシステムを示す。

　　第7章では本論文のマイナーな貢献として拡張状態と無香カルマンフィルタを適用した状態とパラメータの同時推定について述べる。例として車両のコーナリングスティフネスと横滑り角の推定を行い、提案手法の有効性を実証する。この推定設計で使用される主要センサーはタイヤ横力センサである。

　　最後に、第8章で本論文のまとめ、結論、そして今後の課題を述べる。

Table of contents

Part B: Motion Control Application 52

Chapter 1:

Introduction

"To the person who does not know where he wants to go there is no favorable wind."

Lucius Annaeus Seneca

1.1 Motion control system and state estimation

Soon after the discovery of the negative feedback of Harold Black in 1927, the first pneumatic motion control products arrived in 1930s [1]. Since then, motion control has attracted tremendous interests in both control theory and practical applications. Until now, motion control plays the important roles in various motion systems, such as trains, automotives, industrial machines, industrial robots, flights, quadcopter, submarine watercrafts, etc. Thanks to the development of electric motors design, motor drives and power electronics, networking, and digital controllers, advance and precision motion control are realized [2]. For instance, Ethernet Power Link (EPL) – an Ethernet extension of CANopen with high connectivity rates and robust communication capabilities, enables the high performance and convenience of motion control [3]. New methods of torque ripple cancellation and speed range extension control of electric motors enables the smooth and accurate actuators for motion control systems [4], [5].

As the definition of Ohnishi *et al* [6], the motion control system includes the mechanical system, the motion reference generator, the controller, the actuators, and the sensors (Fig. 1.1). Through the sensors, motion states are measured and fed back to the controller. The controller computes the control signal to manage the actuators such that the motion of the mechanical system can follows the desired motion from the reference generator. Common motion controls are velocity control, position control, force or acceleration control. Typical actuators are the hydraulic pump, the air cylinder, the linear motors, or the rotational motors. Motion measurement sensors can be the optical encoders, the Hall-effect devices, and the inertia sensors such as gyroscopes or accelerometers. Various control algorithms have been introduced to motion control, such as the proportional-integral-derivative (PID) [7], the disturbance observer (DOB) [8], and the sliding-mode control [9].

However, the fundamental motion control configuration in Fig. 1.1 is not always applicable. To maintain the state feedback, the state estimator is required in various motion control system due to the following reasons. Firstly, in the motion control system, there exist motion states that cannot be measured directly. Secondly, some sensors cannot be used in mass production because of their very high cost. For instance, the noncontact optical sensor can be used to measure the sideslip angle of a vehicle [10]. However, it is too expensive for commercial cars. Therefore, the sideslip angle estimators
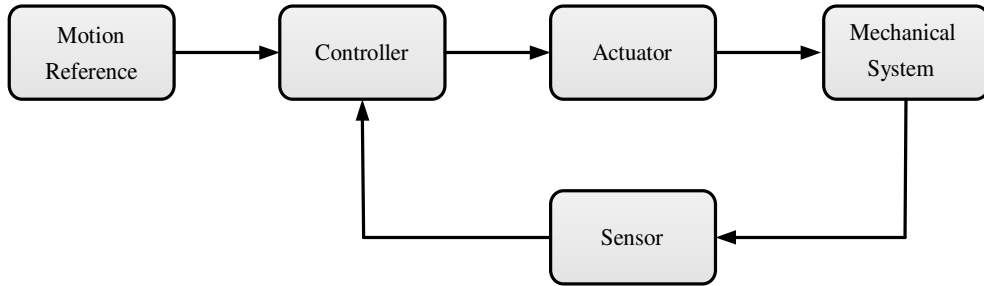
Fig. 1.1 Motion control system – a fundamental definition by Ohnishi (1996).
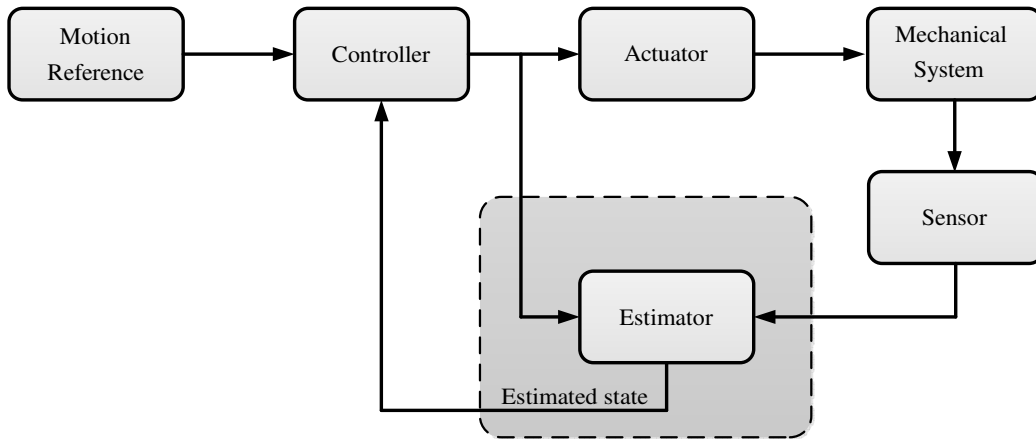
Fig. 1.2 State estimation in the motion control system.

using lower cost sensor such as inertia measurement units (IMUs) are implemented in every vehicle stability control system. The motion control system with the state estimator is shown in Fig. 1. 2.

1.2 Fundamental tools for state estimation

In order to estimate the state, it is necessary to establish the state space model including the dynamic equations and the measurement equations. In the discrete-time domain, the linear state space model is expressed as follows:

Dynamic equation:

$$x_{k+1} = A_k x_k + B_k u_k + w_k \tag{1.1}$$

Measurement equation:

$$y_k = C_k x_k + v_k \tag{1.2}$$

where x_k is the state vector, u_k is the input vector, y_k is the measurement vector, A_k is the state matrix, B_k is the input matrix, C_k is the measurement matrix, w_k and v_k are the process and measurement noises, respectively.

There are two fundamental tools for estimation design, the Observer and the Kalman filter:

1- Observer [11]:

$$\hat{x}_{k+1} = A_k \hat{x}_k + B_k u_k + L_k \left(y_k - C_k \hat{x}_k \right) \tag{1.3}$$

where $\hat{x}_k$ is the observed stated, L_k is the observer gain matrix designed by pole-placement considering the desired eigenvalues of the estimation error dynamics:

$$\tilde{x}_{k+1} = x_{k+1} - \hat{x}_{k+1} = (A_k - L_k C_k)\tilde{x}_k + (w_k - L_k v_k) \tag{1.4}$$

    2-Kalman filter [12]:

    Prediction:

$$\hat{x}_{k|k-1} = A_{k-1}\hat{x}_{k-1|k-1} + B_{k-1}u_{k-1} \tag{1.5}$$

    Correction:

$$\hat{x}_{k|k} = \hat{x}_{k|k-1} + L_k\left(y_k - C_k\hat{x}_{k|k-1}\right) \tag{1.6}$$

where $\hat{x}_{k|k-1}$ is the predicted state, $\hat{x}_{k|k}$ is the corrected state, L_k is the filter gain matrix solved by minimizing the correction error covariance:

$$\tilde{P}_{k|k} = E\left[\left(x_k - \hat{x}_{k|k}\right)\left(x_k - \hat{x}_{k|k}\right)^T\right] \to \min \Leftrightarrow \frac{\partial \tilde{P}_{k|k}}{\partial L_k} = 0 \tag{1.7}$$

Based on the above fundamental tools, many other estimation algorithms are developed, such as nonlinear observer [13], sliding mode observer [14], extended Kalman filter [15], and unscented Kalman filter [16].

1.3 Practical problems

In this section, three practical problems in motion control are discussed for establishing the research background and motivation of this thesis.

1.3.1 Estimation of vehicle's sideslip angle using GPS and yaw-rate sensor

Sideslip angle is defined as the angle between the vehicle's velocity vector at the center of gravity and the longitudinal axis (Fig. 1.3). To stabilize the lateral motion, for instance on cornering road, sideslip angle must be controlled [17]. Otherwise, the sideslip angle might increase considerably even if the yaw-rate is controlled. In this situation, the vehicle cannot maintain the desired path and the serious accidents might happen.

Unluckily, current commercial vehicles are not equipped with an ability to measure the sideslip angle directly. Using the noncontact optical sensor produced by Corrsys-Datron, the longitudinal and the lateral velocity of the vehicle can be measured. Thus, sideslip angle can be calculated as:

$$\beta = \tan^{-1}\left(\frac{v_y}{v_x}\right) \tag{1.8}$$

Because of the very high cost, this optical sensor is not affordable for mass production. Sideslip angle estimation has been an important topic in motion control of vehicle. From literature reviews, many sideslip angle estimation methods using inertia sensors (IMU) have been proposed, such as in [18], [19], [20].
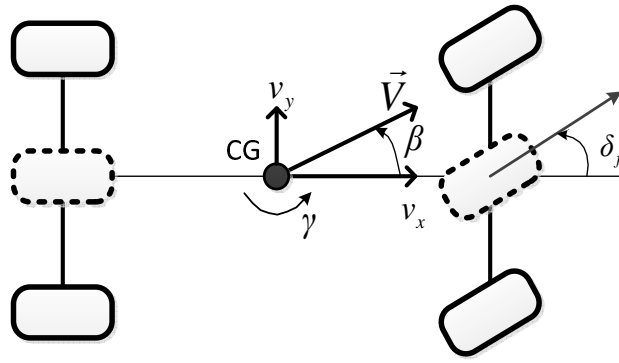
Fig. 1.3 Sideslip angle of the vehicle.
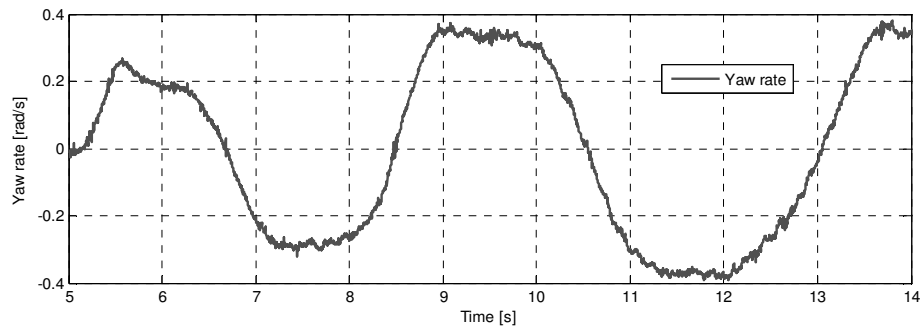
(a)
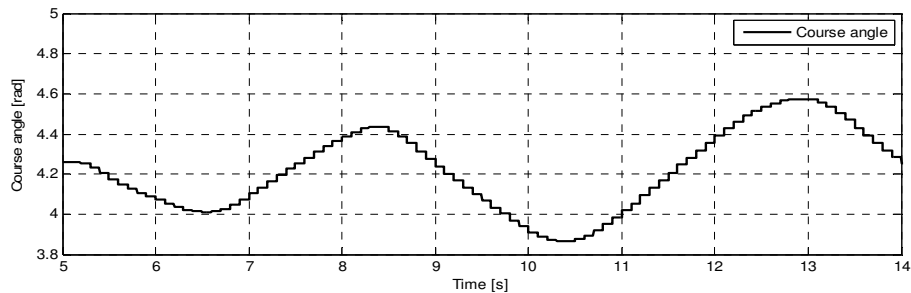
(b)

Fig. 1.4 High-rate yaw-rate measurement (a) and low-rate GPS course angle measurement (b).

However, IMUs (yaw-rate sensor or acceleration sensor) are always suffered from strong noises, sensor bias, scale error, and the change of the temperature. Moreover, the influences of the external forces (strong wind or gravity) are not accurately captured by IMUs. In recent years, GPS becomes a candidate for sideslip angle estimation. Besides the position and the velocity, the on-board GPS receiver can provide the measurement of the course angle of the vehicle [21] or the sideslip angle calculation [22]. The motion measurement using GPS is obtained at high accuracy in long term, thanks to the development of GPS technology such as the Real time kinematic GPS (RTK GPS) [23]. It is also possible to estimate the sideslip angle using the fusion of GPS and IMUs, such as single antenna GPS and yaw-rate sensor [24].

There are two main problems in sideslip angle estimation using GPS. First, while the yaw-rate can be measured at high rate using the IMU, the GPS data's update rate is very poor, usually less than 50 Hz. Fig. 1. 4 shows the experimental results in which the yaw-rate sensor's update frequency is 1 kHz while the GPS's rate is only 10 Hz. This means that between two consecutive updates of the GPS measurement, the sideslip angle estimation only relies on the yaw-rate. Moreover, the dynamic model of the vehicle contains the time varying parameters such as the cornering stiffness which depends on the road condition. Therefore, the fundamental tools introduced in the previous section are not applicable to estimate sideslip angle accurately. In other words, it is desirable to design the robust filter considering the dual-rate measurements of GPS and yaw-rate sensor.

1.3.2 Estimation of the target position in chip-mounting machine

Chip-mounting machine is a type of industrial machines based on surface mount technology (SMT) such that an actuator system is used to pick and place the surface-mount devices (SMDs) onto a printed circuit board (PCB). The photo of a chip-mounting machine produced by Hitachi Ltd. is shown in Fig. 1. 5. Although the motion trajectory can be programmed in advances, position error might occur due to the influences of the environment and the operation process to the mechanical system. To improve the mounting accuracy, the pick and place motion can be handled by visual servo control. In this system, the relative position between the target on the PCB and the object (the chip device) is obtained from the image processing unit (IPU). Then, the controller generates the control signal to drives the linear motor to move the object to the target as fast and accurate as possible [25].

However, the problem is that the position measurement from the IPU is delayed due to the time required for exposure, image processing, and data transferring. The time delay of few milliseconds is very large in comparison with the control period of 0.1 millisecond of the linear motor [25]. Moreover, current image processing technique cannot provide the relative position at high rate. A standard NTSC camera frequency which is often used in visual sensing has the sampling frequency of 30 Hz. To the best of our knowledge, the maximum visual processing capability using high speed camera is only 1 kHz [26] which is still smaller than the linear motor control frequency of 10 kHz [25]. The time-delay and the low-rate of the position measurement using IPU through a real-time experiment is expressed in Fig. 1. 6.

Fig. 1.5 Hitachi GXH-1S-Direct drive modular mounter (http://www.smtnet.com).
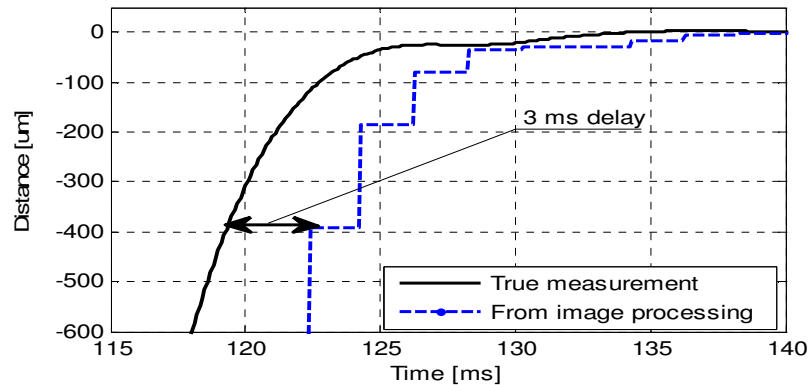
Fig. 1.6 Target position through image processing unit (data of a real-time experiment).

If the delayed measurement is fed back, not only the tracking performance but also the stability of the control system is degraded. Thus, it is essential to design the estimation method that can compensate the large-time-delay and improve the rate of the IPU.

1.3.3 On-line estimation of the parameter

The parameters of the dynamics system can be the total mass, the moment of inertia, the height of the system's center of gravity, etc. It is very important to understand the system's parameters precisely to design the controller. For instance, the feed-forward controller is designed by inversing the system dynamics. If the parameters are inaccurate, the feed-forward control signal cannot satisfy the desired motion. Many parameters are constant and they can be measured or identified before designing the controller. However, there exists parameters that vary during the operation and they cannot be measured directly. For different control purposes, it is useful to perform on-line identification of system parameters. The estimated parameters can be used for designing adaptive feedback controller [27] or adaptive feed-forward controller [28].

A typical configuration for on-line estimation of the state and the parameter is shown in Fig. 1. 7 including two parallel components. The estimator (observer or filter) outputs the estimated state $\hat{x}_k$. The estimated state is fed to the recursive least square (RLS) identification to obtain $\hat{C}_k$ which is again fed to the estimator to update the estimation model in the next estimation period. For instance, this model is used to estimate the sideslip angle and the cornering stiffness of an electric vehicle in [29].

However, the effectiveness of the above estimation configuration is still questionable. *Firstly*, the design of the structure in Fig. 1.7 is complex because it is required to design the estimator and RLS identification separately. *Secondly*, the tuning process may be not flexible. We just can vary the forgetting factor of the identification in a narrow range. If the forgetting factor is close to 1, the convergence performance is too slow. If the forgetting factor is smaller than a threshold, vibration will happen in parameter identification and the quality of state estimation is also degraded considerably. *Thirdly*, the convergence under the very sharp and sudden change of system parameter may be not fast
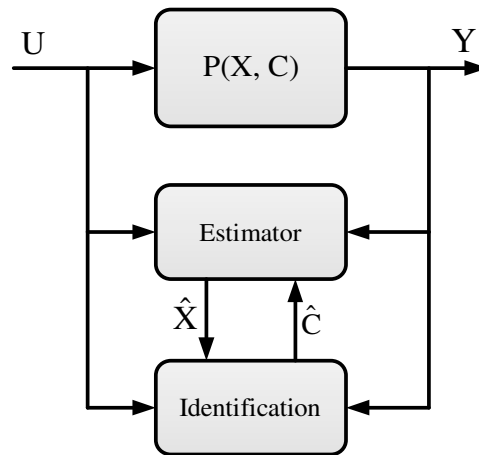
Fig. 1.7 Conventional adaptive estimator.

enough, due to the limitation of the tuning range that we cannot reduce the forgetting factor too much.

From the above discussion, our goal is to seek a simpler but effective estimation configuration. A possible solution is to estimate both the states and the parameters simultaneously using only one model, instead of using the mutual feedback configuration with the estimator and the identification. If the parameters are considered as the extension states, the extension system might be nonlinear and the nonlinear estimation theory is required.

1.4 Literature review on estimation theory

To solve the aforementioned practical problems, we need to look at the estimation theory. In this section, a literature review of estimation theory considering dual-rate issue and delayed measurement issue are presented. The nonlinear estimation is not presented in this section but in the Chapter 4.

1.4.1 Dual-rate estimation

Considering the different rates in an estimation model, it is essential to study the multi-rate estimation. In this thesis, we will focus on the dual-rate estimation. A dual-rate system can be defined as follows:

Dynamic equation:

$$x_{k+1} = A_k x_k + B_k u_k + w_k \tag{1.9}$$

Measurement equation:

$$y_k = C_k x_k + \delta_k v_k \tag{1.10}$$

where

$$C_k = \begin{cases} C & if \ k = jr \\ 0 & if \ k \neq jr \end{cases} \tag{1.11}$$

$$\delta_k = \begin{cases} 1 & if \ k = jr \\ 0 & if \ k \neq jr \end{cases} \tag{1.12}$$
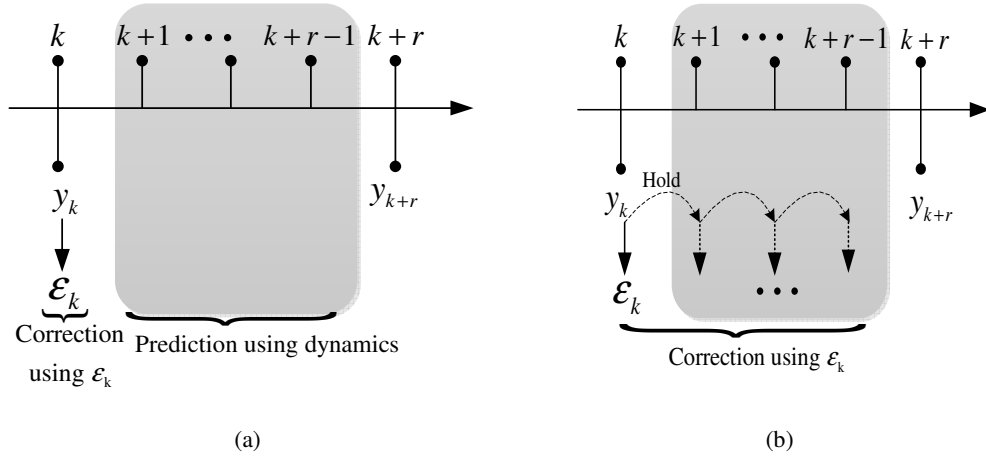
Fig. 1.8 Dual-rate estimation: a) conventional method, b) innovation holding method.

where j is the integer and r is the dual-rate ratio between the sampling time of the measurement T_s and the control period T_c (in this thesis r is assumed to be a constant).

$$r = \frac{T_s}{T_c} \tag{1.13}$$

Literature review shows that there are two main methods for dual-rate estimation (see Fig. 1. 8).

1- Conventional dual-rate estimation (CDRE).

$$\begin{cases} \hat{x}_{k+1} = A_k \hat{x}_k + B_k u_k + L_k \left(y_k - C_k \hat{x}_k \right) & \text{if } k = jr \\ \hat{x}_{k+1} = A_k \hat{x}_k + B_k u_k & \text{if } k \neq jr \end{cases} \tag{1.14}$$

When the measurement is unavailable, the state is only predicted using the dynamic model. This method is widely utilized in various applications. For instance, Hori named the method "instantaneous speed observer" to estimate the motor speed from low precision shaft encoder [30] for motion control using motor servo. When generalizing the multi-rate control framework, Fujimoto proposed the intersample observer which is essential equivalent to the instantaneous speed observer [107], [108]. This method is improved by a dual-rate observer with observer gain matrix varying according to the time interval between two consecutive encoder pulses [31]. In [32] and [33], the cascade dual-rate observers are introduced. This method is also represented by the lifting technique in which all the state between two consecutive measurement updates are placed into an extension state vector as follows

[34], [35], [36]: $\quad X_k = \begin{bmatrix} x_k & x_{k+1} & \cdots & x_{k+m-2} & x_{k+m-1} \end{bmatrix}^T$.

The *CDRE* is certainly very simple to be implemented. However, between two consecutive measurements, the state is only predicted without any correction. Therefore, the estimated state may be non-smooth and the estimation accuracy might be seriously degraded due to the influence of the model uncertainties and the unknown disturbances.

2- Innovation holding dual-rate estimation (IHDRE).

Assume that $k = jr$, the measurement is unavailable during the period $k+i$ where $i \in [1, r-1]$. The

IHDRE is performed as follows:

$$\begin{cases} \hat{x}_{k+1} = A_k\hat{x}_k + B_ku_k + L_k\left(y_k - C_k\hat{x}_k\right) & \text{for } k = jr \\ \hat{x}_{k+i+1} = A_{k+i}\hat{x}_{k+i} + B_{k+i}u_{k+i} + L_{k+i}\left(y_k - C_k\hat{x}_k\right) & \text{for } i \in [1, r-1] \end{cases} \tag{1.15}$$

The key idea of this method is to hold the innovation $\varepsilon_k = y_k - C_k\hat{x}_k$ for estimating the state when the measurement is still unavailable. Hara *et al* proposed this method for motion control of the hard disk drives in which the sampling frequency of the position sensor is one-quarter of the control updating frequency [37]. Thanks to the innovation holding, smoother position estimation and control is achieved. On the other hand, Oh *et al* utilized the innovation holding to improve the instantaneous speed observer in motion control of the electric wheelchair [38]. However, Hara and Oh used the conventional pole-placement scheme to obtain the observer gain L_{k+i} in (1.15). No consideration on model uncertainties and unknown disturbances is taken into account when designing the estimation gain. This is also our problem in the first attempt to deal with dual-rate estimation using Kalman filter and innovation holding [39].

Discussion: *CDRE* and *IHDRE* might be suitable for the applications in which the model uncertainty is small. In case of considerable model uncertainties and strong external disturbances, it is essential to develop the robustness of dual-rate estimation.

1.4.2 Estimation with time-delay measurement

A system with delayed measurement can be expressed as:

$$x_{k+1} = A_kx_k + B_ku_k + w_k \tag{1.16}$$

$$y_k = C_{k-d}x_{k-d} + v_k \tag{1.17}$$

where d is the number of delayed samples. In this thesis, we assume that d is a constant.

Literature review shows that there are following methods for state estimation with delayed measurement.

1-Cascade estimation

This estimation algorithm is explained in Fig. 1. 9. The input signal is intentionally stored for

$d+1$ periods $[u_{k-(d+1)}, u_{k-d}, u_{k-(d-1)}, ..., u_{k-2}, u_{k-1}]$. In the first stage, the past time state $\hat{x}^*_{k-d|k-d}$ is

estimated by standard Kalman filter using the delayed measurement y_k and the input u_{k-d}. Then, in the second stage, the present time state is obtained through a d-step prediction as follows:

$$\begin{cases} \hat{x}^*_{k-(d-1)|k-(d-1)} = A_{k-d}\hat{x}^*_{k-d|k-d} + B_{k-d}u_{k-d} \\ \hat{x}^*_{k-(d-2)|k-(d-2)} = A_{k-(d-1)}\hat{x}^*_{k-(d-1)|k-(d-1)} + B_{k-(d-1)}u_{k-(d-1)} \\ ... \\ \hat{x}^*_{k|k} = A_{k-1}\hat{x}^*_{k-1|k-1} + B_{k-1}u_{k-1} \end{cases} \tag{1.18}$$
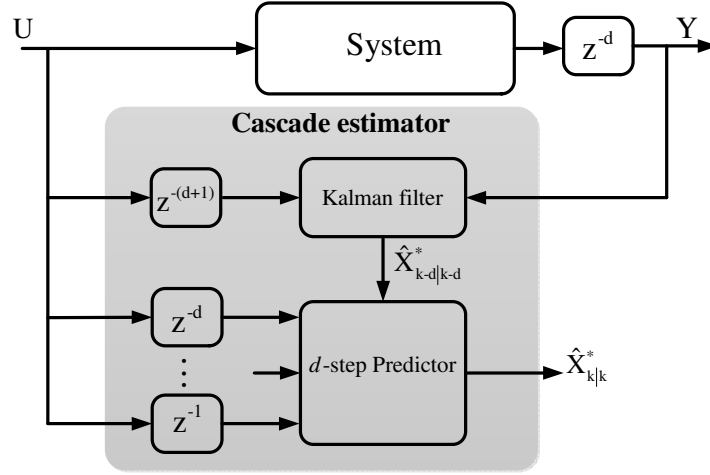
Fig. 1.9 Cascade configuration for estimation with delayed measurement.

This algorithm is very simple and it is introduced in [40] to estimate the state of the system with the delayed and non-delayed measurements. If the model is ideally precise, this method seems to be a good solution. However, if the number of the delayed samples is big, huge computational effort is required. Moreover, if the model contains uncertainty, the d-step prediction process cannot provide the accurate estimated state.

2-State augmentation

The key idea of this method is to organize the augmented system using the extended state vector

$$X_k = \begin{bmatrix} x_k^T & x_{k-1}^T & \dots & x_{k-d}^T \end{bmatrix}^T$$ where d is the number of delayed samples [41], [42], [43]. Then, the

estimation problem becomes the design of the standard Kalman filter for the augmented system. If the time delay stands for few samples, this method would be a suitable solution. However, the time delay is big, the size of the augmented system will be increased considerably along with the computational cost. Moreover, the design and the tuning procedure will become a complex task due to the huge size of the process noise covariance matrix associated with the extended state X_k.

3-Measurement extrapolation

This is a popular method proposed by Larsen *et al* [44]. Application of this method can be found in the vehicle state estimation using GPS and magnetometer [45]. The key idea of this method is to extrapolate the measurement y_k^* from the delayed measurement y_k:

$$y_k^* = y_k + C_k \hat{x}_{k|k-1} - C_{k-d} \hat{x}_{k-d|k-d-1} \tag{1.19}$$

The extrapolated measurement is proved to be equivalent to a non-delayed measurement:
$$y_k^* = C_k x_k + v_k^* \tag{1.20}$$
where

$$v_k^* = v_k + C_{k-d} \tilde{x}_{k-d|k-d-1} - C_k \tilde{x}_{k|k-1} \tag{1.21}$$
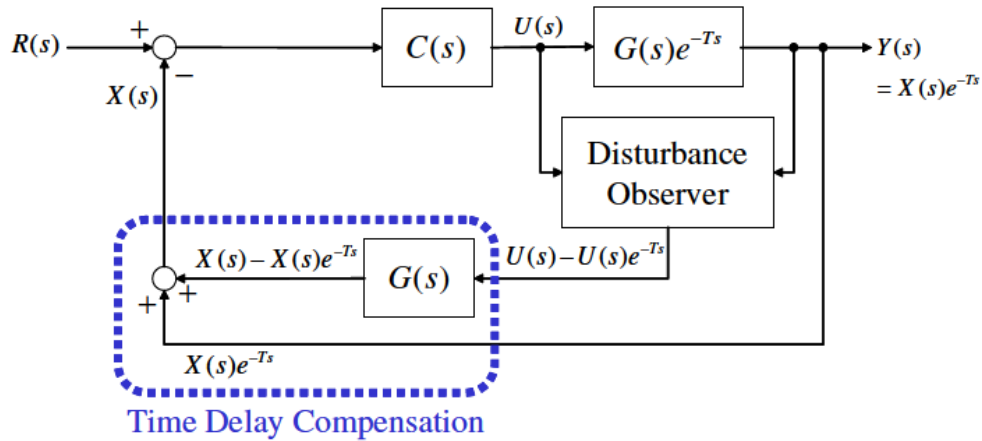
Fig. 1.10 Feedback control of time delay system based on Communication Disturbance Observer.

In comparison with the state augmentation method, this method has the advantage of maintaining the dimension of the system. However, it is hard to know the covariance of the noise v_k^* associating with y_k^*. Therefore, Larsen *et al* proposed to compute the prediction/correction error covariance approximately. Consequently, the solution of the Kalman gain is sub-optimal. As stated by Larsen, the algorithm is only applicable if there is no other measurement fused during the delay period [k-d, k].

4-Innovation reorganization

This method has been studied since the last decade [46], [47], [48], [49]. For instance, in [46], the algorithm for the fusion of a non-delayed measurement $y_1(t)$ with a delayed measurement $y_2(t)$ is proposed. The key idea of this method is to organize two new measurement sequences $Y_1(t) = y_1(t)$ and $Y_2(t) = [y_1(t) \quad y_2(t+t_d)]^T$ where t_d is the delay time. The algorithm includes the solving of two Riccati equations or two Kalman filters associated with $Y_1(t)$ and $Y_2(t)$ in real-time, one followed by the other. Therefore, this method requires the high computational cost, especially when the time delay t_d is large. Moreover, this method is only demonstrated by simulations without any experiment or practical application.

5-Inter-sample observer

In case of multi-rate sampling system with delayed measurement, Fujimoto improved the inter-sample observer to estimate the unknown state [109], [110]. Fujimoto introduced the extended state $\bar{x} = \begin{bmatrix} x^T & x_u^T \end{bmatrix}^T$ and the extended measurement $\bar{y} = \begin{bmatrix} y^T & x_u^T \end{bmatrix}^T$ where x is the state, y is the delayed measurement, and x_u is a vector composed of the intersample control inputs. By this way, a non-delayed augmented system is established and the delay-compensation is solved easily. This method is beautiful from the view of mathematic formulation. However, it has three problems. First, it is required to increase the size of the system. Secondly, it is the observer which cannot assure the optimality of the observer gain. In other words, we do not know if we can minimize the estimation error covariance at a given control period. Thirdly, the observation matrix of the augmented system is

obtained by calculating $C_c e^{A_c v_y T_f}$ where A_c is the state matrix of the original system in continuous time form, C_c is the observation matrix of the original system, and $v_y = -T_d / T_f$, T_f is the fundamental sampling time and T_d is the delay time. If matrix A_c contains big model uncertainty, the accuracy of the extended measurement and the robustness of the observer might be degraded.

6-Communication Disturbance Observer (CDOB)

The delay in the feedback control system is handled using CDOB, as shown in Fig. 1.10 [119]. The key idea of this method is very interesting such that the original system with time delay is represented as a non-delayed system with network disturbance. The advantage of the method is that it can be implemented even if the system contains time varying delay without any change in the algorithm. However, there are several questions for this method. The first is how to apply this method to a multi input-multi output system and obtain other internal state rather than the output? The second question is how much the delay is compensated? The quality of delay compensation depends on how we can know the model transfer function *G(s)* precisely? Will this method still effective if *G(s)* suffers from strong uncertainty?

Besides the above studies, a number of works have been done in the topic of state estimation with delayed measurement, such as *nonlinear estimation with delayed measurement* [50], [51], [52]; *robust estimation with delayed measurement* [53], [54]; *estimation with random time delay measurement* [55], [56], etc. For instance, in [55], the random time delay problem is solved under the assumption that the probability density function of the time delay is known.

Discussion: Literature review shows that estimation with delayed measurement is not a new topic. Many works and methods have been conducted for two decades. However, it is still desirable to design the practical algorithm for estimation with large-time-delay measurement, such that: a) The algorithm does not requires the innovation reorganization and the solving of multiple Riccati equations. b) The algorithm does not increase the system's dimension. c) The optimality and the stability of the algorithm are assured to a certain extent. The random time delay is not the main goal of this study, but a little discussion on this issue will be given in the Chapter 3.

1.5 Research motivation

1.5.1 Theory contribution

1-Robust dual-rate filter

Objective: Consider the dual-rate system in which the measurement is updated at low-rate and the control signal stands for the fast-rate. The estimation is designed with the constant nominal parameter C_n. Due to the model uncertainty, the real parameter of the system is $C_n + \Delta C$. We aim to design the robust dual-rate filter and compare the proposed filter with other dual-rate estimation methods.

Solution: Firstly, we will propose the disturbance accommodation dual-rate Kalman filter in which the disturbance term is the extended state. This method is applied in the practical application. Then, we will design the robust dual-rate Kalman filter by considering the bound uncertainty in the

system dynamics through the upper-bound of the estimation error covariance.

2-Time-delay compensation filter

<u>Objective:</u> Consider the system in which the measurement is delayed. Assume that the number of the delayed sample *d* is a *large* constant. We aim to design the filter to handle the delayed measurement and estimate the state accurately and compare the proposed filter with other time-delay estimation methods. Then, we will discuss the case such that the number of delayed sample is a random number.

<u>Solution:</u> As it is very complex to derive the estimation error covariance in the filter algorithm with large-time-delay measurement, we propose the method to obtain the upper-bound of estimation error covariance. The filter gains are simply designed by minimizing the upper-bound.

3-Simultaneous estimation of state and parameter

<u>Objective:</u> Consider the system which includes the state *X* and parameter *C*. We will establish the augmented system with the augmented state vector $[X \quad C]^\mathrm{T}$. We aim to estimate the state and the parameter simultaneously using the augmented system and compare the proposed method with the estimation configuration in Fig. 1. 7.

<u>Solution:</u> Even if the original system is linear, the augmented system is usually nonlinear. Therefore, we will apply a sigma-point-transformation based tool, the unscented Kalman filter (UKF) [104] to estimate the augmented system.

1.5.2 Application contribution

The estimation theories are developed through three applications as follows:

1-Electric vehicle motion control using GPS

Using the proposed dual-rate filter, GPS, and other sensors, we design the estimator to obtain the following motion variables of the electric vehicles: sideslip angle, yaw angle, and longitudinal velocity. They are applied to three motion controls, lateral stability motion control, attitude control, and slip ratio control, respectively.

2-Chip-mounting machine

Using the proposed time-delay filter and the fusion of IPU and linear encoder, we design the estimator to estimate the relative position of the target. The estimated position is used for target tracking control.

3-Estimation of sideslip angle and tire cornering stiffness of the vehicles

Consider the lateral dynamics of the vehicle, we establish the augmented system with the state vector $\begin{bmatrix} \beta & \gamma & C_f & C_r \end{bmatrix}^T$ where β is the sideslip angle, γ is the yaw-rate, C_f and C_r are the front and rear tire cornering stiffness. Two sources of measurements are used: yaw-rate sensor and tire lateral force sensors. We will use the unscented Kalman filter to estimate the tire cornering stiffness with the sideslip angle simultaneously. In addition, we will prove that the proposed estimation is more effective than the conventional estimation shown in Fig. 1. 7.

Part A

Kalman Filter Theory

Chapter 2:
Robust Dual-rate Kalman Filter

"The quality of your life is in direct proportion to the amount of uncertainty you can comfortably deal with."

Tony Robbins

2.1 Introduction

One of our motivations is to enhance the accuracy of the dual-rate estimation in which the sampling time of the output equals to multiple times of the control period (example: Fig. 2.1). In this chapter, we will try to design the robust dual-rate Kalman filter from two points of view as follows:

1) Dual-rate disturbance accommodation Kalman filter

The idea of disturbance accommodation was proposed by Johnson in [83] for linear regulator. By introducing a disturbance term and its dynamics, an augmented state system is established. The estimated disturbance can be fed back to improve the robustness of the control system. In this thesis, we will utilize this idea to enhance the dual-rate estimation. During the periods that the measurement is unavailable, the correction is still maintained by the estimated disturbance.

2) Dual-rate Kalman filter considering the norm-bounded model uncertainty

The model may contain uncertainties due to the following reasons:

+ The error of parameter identification.

+ The parameter is time-varying and cannot be known precisely (for instance the tire cornering stiffness of the vehicle).

In many motion control system, the estimator/controller is designed using the constant nominal parameters because the on-line parameter identification increases the cost of the system. In addition, more hardware or computational efforts may be needed. Therefore, it is essential to improve the robustness of the control system with constant nominal parameters. For instance, the upper-bound scheme has been utilized for robust filter design in [97], [98], [99], [100]. Due to the model uncertainty, it is impossible to exactly derive the estimation error covariance P_k. To overcome this obstacle, linear matrix inequality is utilized to find the upper-bound Ω_k of the estimation error covariance under the assumption that the uncertainty is norm-bounded. The estimation gain L_k can be designed such that it minimizes the upper-bound Ω_k. In other words, the estimation gain is obtained by solving the following equation:

$$\frac{\partial \Omega_k}{\partial L_k} = 0 \qquad\qquad (2.1)$$
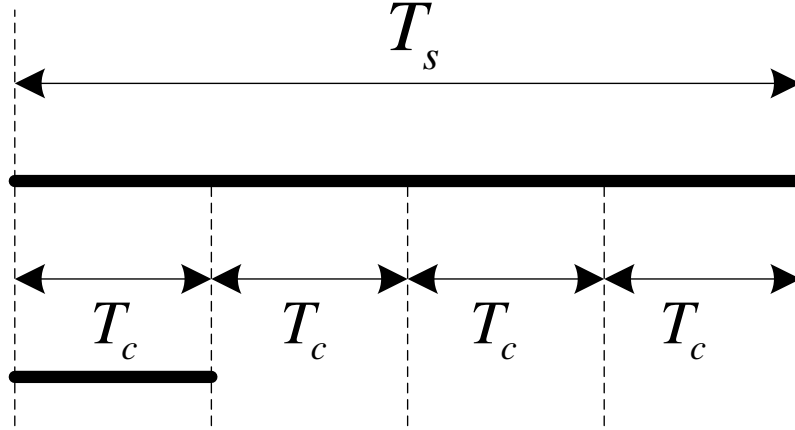
Fig. 2.1 Example of the dual-sampling-time: $T_s = rT_c$ where $r = 4$.

Literature review also shows that almost the robust filters based on upper-bound (such as [97] ~ [100]) do not deal with the unknown input due to the external disturbance or the uncertainty in the input matrix. For this reason, we will propose the robust dual-rate filter considering not only the model uncertainty but also the unknown input. A possible solution is to combine the disturbance accommodation scheme with the upper-bound scheme. This is the last effort in this Chapter to enhance the dual-rate estimation.

2.2 Dual-rate disturbance accommodation Kalman filter
2.2.1 System modeling

The discrete-time stochastic dual-rate system can be expressed as follows:

$$\begin{cases} x_{k+1} = A_k x_k + B_k u_k + w_k \\ y_k = C_k x_k + \delta_k v_k \end{cases} \tag{2.2}$$

where x_k is the state vector, u_k is the input vector, y_k is the output vector. A_k is the state matrix, B_k is the input matrix, and C_k is the measurement matrix. w_k is the process noise, v_k is the measurement noise.

The size of the vectors and the matrices are as follows: $x_k \in \mathrm{R}^{\mathrm{m}}$, $u_k \in \mathrm{R}^{\mathrm{p}}$, $y_k \in \mathrm{R}^{\mathrm{q}}$, $w_k \in \mathrm{R}^{\mathrm{m}}$, $v_k \in \mathrm{R}^{\mathrm{q}}$,

$\dim[A_k] = m \times m$, $\dim[B_k] = m \times p$, $\dim[C_k] = q \times m$.

Define the dual-rate ratio as:

$$r = \frac{T_s}{T_c} \tag{2.3}$$

where T_s is the sampling time of the output, and T_c is the control input's period.

<u>Assumptions:</u>

- The process noise and the measurement noise are Gaussian noises with zero means and they are uncorrelated with each other.

$$w_k \sim (0, R_{w,k}); \quad v_k \sim (0, R_{v,k}); \quad E\left[w_k v_k^T\right] = 0 \tag{2.4}$$

- The dual-rate ratio r is a constant integer.
- The system is fully observable.

The output's sampling time equals to r times of the control period. Thus, the switching of the output measurement is expressed as:

$$C_k = \begin{cases} C & \text{if } k=jr \\ [0]_{q \times m} & \text{if } k \neq jr \end{cases}; \quad \delta_k = \begin{cases} [I]_{q \times q} & \text{if } k=jr \\ [0]_{q \times q} & \text{if } k \neq jr \end{cases} \tag{2.5}$$

where j is the integer.

2.2.2 Disturbance accommodation

To deal with model uncertainty and disturbance, we introduce the disturbance term $x_{d,k}$ and its dynamics:

$$x_{k+1} = A_k x_k + B_k u_k + x_{d,k} + w_k \tag{2.6}$$

$$x_{d,k+1} = A_{d,k} x_{d,k} + w_{d,k} \tag{2.7}$$

where $A_{d,k}$ is the state matrix of the disturbance process. $w_{d,k}$ is a Gaussian noise with zero means. $x_{d,k}$ $\in R^m$, $w_{d,k} \in R^m$, dim$[A_{d,k}] = m \times m$. The noise $w_{d,k}$ is assumed to be uncorrelated with w_k and v_k:

$$w_{d,k} \sim (0, R_{wd,k}), \quad E\left[w_{d,k} w_k^T\right] = 0, \quad E\left[w_{d,k} v_k^T\right] = 0 \tag{2.8}$$

If $A_{d,k}$ is selected as the unity matrix, the disturbance term becomes a random-walk process.

From (2.6) and (2.7), we can establish the augmented system:

$$\begin{cases} \bar{X}_{k+1} = \bar{A}_k \bar{X}_k + \bar{B}_k \bar{U}_k + \bar{W}_k \\ \bar{Y}_k = \bar{C}_k \bar{X}_k + \bar{\delta}_k \bar{V}_k \end{cases} \tag{2.9}$$

where:

$$\bar{X}_k = \begin{bmatrix} x_k \\ x_{d,k} \end{bmatrix}, \quad \bar{U}_k = u_k, \quad \bar{Y}_k = y_k, \quad \bar{W}_k = \begin{bmatrix} w_k \\ w_{d,k} \end{bmatrix}, \quad \bar{V}_k = v_k \tag{2.10}$$

$$\bar{A}_k = \begin{bmatrix} A_k & [I]_{m \times m} \\ [0]_{m \times m} & A_{d,k} \end{bmatrix}, \quad \bar{B}_k = \begin{bmatrix} B_k \\ [0]_{m \times p} \end{bmatrix}, \quad \bar{C}_k = \begin{bmatrix} C_k & [0]_{q \times m} \end{bmatrix}, \quad \bar{\delta}_k = \delta_k \tag{2.11}$$

$A_{d,k}$ is selected such that the augmented system is full observable. The covariance matrices associated with the process noise and measurement noise of the augmented system is expressed as:

$$\bar{R}_{w,k} = \begin{bmatrix} R_{w,k} & [0]_{m \times m} \\ [0]_{m \times m} & R_{wd,k} \end{bmatrix}, \quad \bar{R}_{v,k} = R_{v,k} \tag{2.12}$$

2.2.3 Kalman filter algorithm

Standard Kalman filter can be applied to estimate the state of the augmented system. The algorithm is presented as follows:

Initial condition:

$$\hat{\bar{X}}_{0|0} = \begin{bmatrix} \hat{x}_{0|0} \\ \hat{x}_{d,0|0} \end{bmatrix}; \quad \bar{P}_{0|0} = diag\left(P_{11}, ..., P_{m \times m}, ..., P_{2m \times 2m} \right) \tag{2.13}$$

Prediction stage:

- Predicted state:

$$\hat{\bar{X}}_{k|k-1} = \bar{A}_{k-1} \hat{\bar{X}}_{k-1|k-1} + \bar{B}_{k-1} \bar{U}_{k-1} \tag{2.14}$$

- Prediction error covariance:

$$\bar{P}_{k|k-1} = \bar{A}_{k-1} \bar{P}_{k-1|k-1} \bar{A}_{k-1}^{T} + \bar{R}_{w,k} \tag{2.15}$$

Correction stage:

- Estimation gain:

$$\bar{L}_{k} = \bar{P}_{k|k-1} \bar{C}_{k}^{T} \left(\bar{C}_{k} \bar{P}_{k|k-1} \bar{C}_{k}^{T} + \bar{\delta}_{k} \bar{R}_{v,k} \bar{\delta}_{k}^{T} \right)^{-1} \tag{2.16}$$

- Corrected state:

$$\hat{\bar{X}}_{k|k} = \hat{\bar{X}}_{k|k-1} + \bar{L}_{k} \left(\bar{Y}_{k} - \bar{C}_{k} \hat{\bar{X}}_{k|k-1} \right) \tag{2.17}$$

- Correction error covariance:

$$\bar{P}_{k|k} = \left(I - \bar{L}_{k} \bar{C}_{k} \right) \bar{P}_{k|k-1} \tag{2.18}$$

where $\hat{\bar{X}}_{k|k-1}$ is the predicted state, $\hat{\bar{X}}_{k|k}$ is the corrected state (the estimated value which is output from the Kalman filter), $\bar{L}_{k}$ is the estimation gain, $\bar{P}_{k|k-1}$ is the prediction error covariance, and $\bar{P}_{k|k}$ is the correction error covariance. $\hat{x}_{0|0}$ and $\hat{x}_{d,0|0}$ are the initial vectors of the state and the disturbance term, $\bar{P}_{0|0}$ is the initial matrix of the correction error covariance which is assume to be diagonal matrix.

2.2.4 Discussion

The correction stages of the proposed algorithms is examined for the periods that the measurement is unavailable ($k \neq jr$). Because the measurement matrix is set to zero, the estimation gains of the augmented system will be zero during these periods. The correction stage is performed as:

$$\begin{bmatrix} \hat{x}_{k|k} \\ \hat{x}_{d,k|k} \end{bmatrix} = \begin{bmatrix} \hat{x}_{k|k-1} \\ \hat{x}_{d,k|k-1} \end{bmatrix} \tag{2.19}$$

or:

$$\begin{bmatrix} \hat{x}_{k|k} \\ \hat{x}_{d,k|k} \end{bmatrix} = \begin{bmatrix} \hat{x}_{k|k-1} \\ \hat{x}_{d,k|k-1} \end{bmatrix} = \begin{bmatrix} A_{k-1} & [I]_{m \times m} \\ [0]_{m \times m} & A_{d,k-1} \end{bmatrix} \begin{bmatrix} \hat{x}_{k-1|k-1} \\ \hat{x}_{d,k-1|k-1} \end{bmatrix} + \begin{bmatrix} B_k \\ [0]_{m \times p} \end{bmatrix} u_{k-1} \tag{2.20}$$

From (2/20) the estimated state equations are re-written as:

$$\begin{cases} \hat{x}_{k|k} = A_{k-1}\hat{x}_{k-1|k-1} + B_k u_{k-1} + \hat{x}_{d,k-1|k-1} \\ \hat{x}_{d,k|k} = A_{d,k-1}\hat{x}_{d,k-1|k-1} \end{cases} \tag{2.21}$$
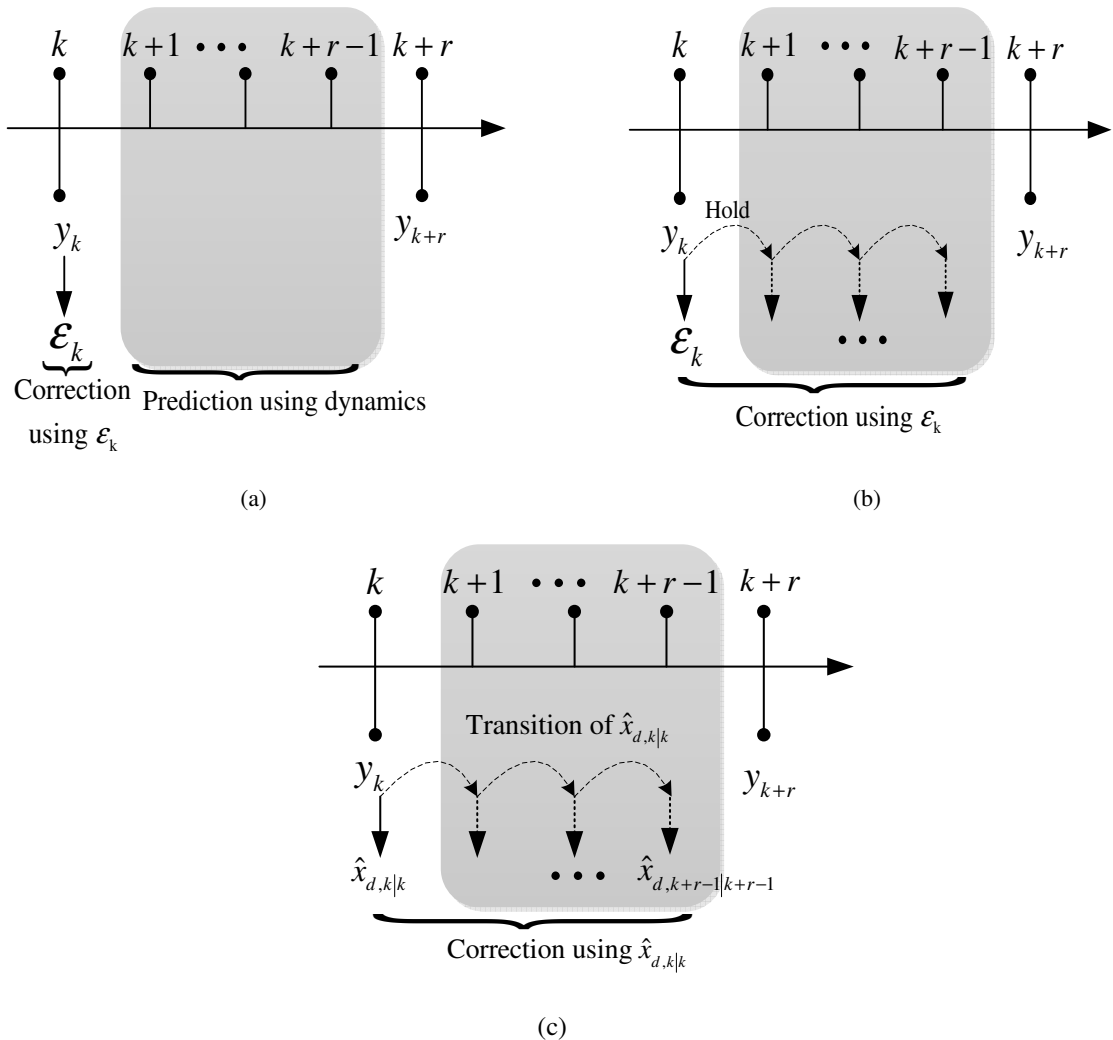

(a)

(b)

(c)

Fig. 2.2 Dual-rate estimation: a) conventional method, b) innovation holding method,

c) disturbance accommodation method.

From (2.21) we can see that: Even though the measurement is unavailable, the estimate of the disturbance term $\hat{x}_{d,k|k}$ serves as the "virtual" innovation to fulfill the correction stage. Therefore, the estimation accuracy can be improved. In practical applications, tuning process is required to select the suitable matrices $A_{d,k}$ and $R_{wd,k}$.

Fig. 2.2 is to compare the key ideas of three dual-rate estimation methods. The "conventional dual-rate estimation" has no correction during the periods that the measurement is unavailable. The "innovation holding dual-rate estimation" holds the innovation ε_k to perform the correction stage. On the other hand, the "disturbance accommodation dual-rate estimation" utilizes the transition of the estimated disturbance $\hat{x}_{d,k|k}$ to perform the correction stage. This also means that the uncertainty and disturbance are treated by "disturbance accommodation dual-rate estimation". Another advantage of this method is that it can provide more tuning parameters which are the matrix matrices $A_{d,k}$ and $R_{wd,k}$.

2.3 Dual-rate filter considering the norm-bounded uncertainty

In the previous section, the disturbance accommodation dual-rate Kalman filter is proposed. However, the model uncertainty is not taken into account in the design procedure. In this section, we will design the robust dual-rate filter from another point of view: the model uncertainties are assumed to be norm-bounded. For the sake of simplicity, the uncertainty is only placed in the state matrix and the system has no input. The upper-bound scheme is applied to obtain the filter parameters $\Delta A_{e,k}$ and $L_{e,k}$.

2.3.1 System modeling and the idea of robust estimation

The discrete-time stochastic dual-rate system with model uncertainty in the state matrix can be expressed as follows:

$$\begin{cases} x_{k+1} = \left(A_k + \Delta A_k \right) x_k + w_k \\ y_k = C_k x_k + \delta_k v_k \end{cases} \tag{2.22}$$

$$C_k = \begin{cases} C & \text{if } k=jr \\ [0]_{q \times m} & \text{if } k \neq jr \end{cases}; \quad \delta_k = \begin{cases} [I]_{q \times q} & \text{if } k=jr \\ [0]_{q \times q} & \text{if } k \neq jr \end{cases} \tag{2.23}$$

The definitions of the vectors and the matrices in (2.22) are the same as in the previous section: x_k is the state vector, u_k is the input vector, y_k is the output vector. A_k is the state matrix, B_k is the input matrix, and C_k is the measurement matrix. w_k is the process noise, v_k is the measurement noise. The size of the vectors and the matrices are as follows: $x_k \in \mathrm{R}^m$, $u_k \in \mathrm{R}^p$, $y_k \in \mathrm{R}^q$, $w_k \in \mathrm{R}^m$, $v_k \in \mathrm{R}^q$, $\dim[A_k] = m \times m$, $\dim[B_k] = m \times p$, $\dim[C_k] = q \times m$.

Assumptions:

-   The process noise and the measurement noise are Gaussian noises with zero means and they are

uncorrelated with each other.

$$w_k \sim \left(0, R_{w,k}\right) ; \quad v_k \sim \left(0, R_{v,k}\right) ; \quad E\left[w_k v_k^T\right] = 0 \tag{2.24}$$

- The dual-rate ratio r is a constant integer.
- The system is fully observable.
- The uncertainty is assumed to be written as:

$$\Delta A_k = H_k F_k E_k \tag{2.25}$$

where H_k and E_k are known matrices with appropriate dimensions, F_k is a bounded matrix, for instance $F_k F_k^T \leq I$.

The robust filter is proposed as follows:

$$\hat{x}_{k+1} = \left(A_k + \Delta A_{e,k}\right)\hat{x}_k + L_{e,k}\left(y_k - C_k \hat{x}_k\right) \tag{2.26}$$

where $\Delta A_{e,k}$ and $L_{e,k}$ are filter parameters to be designed such that the filter is optimal to some extent, $\hat{x}_k$ is the estimated state.

2.3.2 Upper-bound of the estimation error covariance

The estimation error of the filter (2.26) is defined as:

$$\tilde{x}_k = x_k - \hat{x}_k \tag{2.27}$$

From (2.22), (2.25), (2.26) and (2.27), the following dynamics system is established:

$$\overline{Z}_{k+1} = \left(\overline{A}_k + \overline{H}_k F_k \overline{E}_k\right)\overline{Z}_k + \overline{G}_k \overline{W}_k \tag{2.28}$$

$$\overline{Z}_k = \begin{bmatrix} \tilde{x}_k \\ \hat{x}_k \end{bmatrix}; \quad \overline{W}_k = \begin{bmatrix} w_k \\ \delta_k v_k \end{bmatrix} \tag{2.29}$$

$$\overline{A}_k = \begin{bmatrix} A_k - L_{e,k}C_k & -\Delta A_{e,k} \\ L_{e,k}C_k & A_k + \Delta A_{e,k} \end{bmatrix} \tag{2.30}$$

$$\overline{G}_k = \begin{bmatrix} I & -L_{e,k} \\ 0 & L_{e,k} \end{bmatrix} \tag{2.31}$$

$$\overline{E}_k = \begin{bmatrix} E_k & E_k \end{bmatrix} \tag{2.32}$$

$$\overline{H}_k = \begin{bmatrix} H_k \\ 0 \end{bmatrix} \tag{2.33}$$

The covariance matrix of the augmented noise $\overline{W}_k$ is:

$$\overline{R}_{w,k} = \begin{bmatrix} R_{w,k} & 0 \\ 0 & \delta_k R_{v,k} \delta_k^T \end{bmatrix} \tag{2.34}$$

The covariance of the augmented state is expressed as:

$$\overline{\Sigma}_{k+1} = \left(\overline{A}_k + \overline{H}_k F_k \overline{E}_k\right)\overline{\Sigma}_k \left(\overline{A}_k + \overline{H}_k F_k \overline{E}_k\right)^T + \overline{G}_k \overline{R}_{w,k} \overline{G}_k^T \tag{2.35}$$

Apply the **lemma L2** (see the Appendix), if at the estimation period k there exists α_k that satisfies $\alpha_k^{-1} I - \bar{E}_k \bar{\Sigma}_k \bar{E}_k^T > 0$, then the following inequality holds true:

$$\bar{\Sigma}_{k+1} \le \bar{A}_k \bar{\Sigma}_k \bar{A}_k^T + \bar{G}_k \bar{R}_{w,k} \bar{G}_k^T + \alpha_k^{-1} \bar{H}_k \bar{H}_k^T + \bar{A}_k \bar{\Sigma}_k \bar{E}_k^T \left(\alpha_k^{-1} I - \bar{E}_k \bar{\Sigma}_k \bar{E}_k^T \right)^{-1} \bar{E}_k \bar{\Sigma}_k \bar{A}_k^T \tag{2.36}$$

Define the following sequence (assume that the initial state is zero):

$$\bar{\Omega}_0 = \bar{\Sigma}_0 = \begin{bmatrix} P_0 & 0 \\ 0 & 0 \end{bmatrix} \tag{2.37}$$

$$\bar{S}_k = \bar{\Omega}_k + \bar{\Omega}_k \bar{E}_k^T \left(\alpha_k^{-1} I - \bar{E}_k \bar{\Omega}_k \bar{E}_k^T \right)^{-1} \bar{E}_k \bar{\Omega}_k \tag{2.38}$$

$$\bar{\Omega}_{k+1} = \bar{A}_k \bar{S}_k \bar{A}_k^T + \bar{G}_k \bar{R}_{w,k} \bar{G}_k^T + \alpha_k^{-1} \bar{H}_k \bar{H}_k^T \tag{2.39}$$

where P_0 is the initial estimation error covariance.

From the inequality (2.36), it is transparent that the above sequence is an upper-bound of the augmented system:

$$\bar{\Sigma}_{k+1} \le \bar{\Omega}_{k+1} \tag{2.40}$$

On the other hand, we have the following relationship:

$$\tilde{x}_{k+1} = \begin{bmatrix} I & 0 \end{bmatrix} \bar{Z}_{k+1} \tag{2.41}$$

From (2.40) and (2.41), the upper-bound of the estimation error covariance is obtained as:

$$E\left[\tilde{x}_{k+1} \tilde{x}_{k+1}^T \right] \le \begin{bmatrix} I & 0 \end{bmatrix} \bar{\Omega}_{k+1} \begin{bmatrix} I & 0 \end{bmatrix}^T = \Omega_{11,k+1} \tag{2.42}$$

2.3.3 Design of the filter parameters

From (2.30) ~ (2.34), (2.38) ~ (2.39), and (2.42), the dynamics of the upper-bound is obtained as follows:

$$\Omega_{11,k+1} = \bar{L}_k \bar{M}_k \bar{L}_k^T - \bar{L}_k \bar{N}_k^T - \bar{N}_k \bar{L}_k^T + A_k S_{11,k} A_k^T + \alpha_k^{-1} H_k H_k^T + R_{w,k} \tag{2.43}$$

where

$$\bar{L}_k = \begin{bmatrix} L_{e,k} & \Delta A_{e,k} \end{bmatrix} \tag{2.44}$$

$$\bar{M}_k = \begin{bmatrix} C_k S_{11,k} S_k^T + \delta_k R_{v,k} \delta_k^T & C_k S_{12,k} \\ S_{21,k} C_k^T & S_{22,k} \end{bmatrix} \tag{2.45}$$

$$\bar{N}_k = \begin{bmatrix} A_k S_{11,k} C_k^T & A_k S_{12,k} \end{bmatrix} \tag{2.46}$$

$S_{11,k}, \ldots, S_{22,k}$ are the components of the matrix $\bar{S}_k$:

$$\bar{S}_k = \begin{bmatrix} S_{11,k} & S_{12,k} \\ S_{21,k} & S_{22,k} \end{bmatrix} \tag{2.47}$$

The filter parameters $\bar{L}_k = \begin{bmatrix} L_{e,k} & \Delta A_{e,k} \end{bmatrix}$ are designed such that they minimize the upper-bound of the estimation error covariance, in other words:

$$\frac{\partial \Omega_{11,k+1}}{\partial \bar{L}_k} = 0 \tag{2.48}$$

Substitute (2.43) into (2.48) and solve this equation, the filter parameters are obtained as:

$$\begin{bmatrix} L_{e,k} & \Delta A_{e,k} \end{bmatrix} = \bar{N}_k \bar{M}_k^{-1} = \begin{bmatrix} A_k S_{11,k} C_k^T & A_k S_{12,k} \end{bmatrix} \times \begin{bmatrix} C_k S_{11,k} C_k^T + \delta_k R_{v,k} \delta_k^T & C_k S_{12,k} \\ S_{21,k} C_k^T & S_{22,k} \end{bmatrix}^{-1} \tag{2.49}$$

Comment: Consider a dual-rate system with model uncertainty. It is hard to derive exactly the estimation error covariance. Luckily, it is possible to obtain the upper-bound of the estimation error. The set of the filter parameter $\bar{L}_k = \begin{bmatrix} L_{e,k} & \Delta A_{e,k} \end{bmatrix}$ can be designed to minimize the upper-bound of the estimation error covariance.

2.4 Dual-rate filter considering model uncertainty and unknown input

2.4.1 System modeling and the idea of robust estimation

In this section, we extend robust filter by consider not only the model uncertainty but also unknown input. The system with dual-rate ratio r is expressed as follows:

$$\begin{cases} x_{k+1} = (A_k + \Delta A_k) x_k + d_k + w_k \\ y_k = C_k x_k + \delta_k v_k \end{cases} \tag{2.50}$$

$$C_k = \begin{cases} C & if \ k=jr \\ [0]_{q \times m} & if \ k \neq jr \end{cases}; \quad \delta_k = \begin{cases} [I]_{q \times q} & if \ k=jr \\ [0]_{q \times q} & if \ k \neq jr \end{cases} \tag{2.51}$$

The term d_k is the unknown input which can be the disturbance to the system. The definition of the vectors and matrices in (2.50) and other assumptions can be followed the previous section: x_k is the state vector, u_k is the input vector, y_k is the output vector. A_k is the state matrix, B_k is the input matrix, and C_k is the measurement matrix. w_k is the process noise, v_k is the measurement noise. The size of the vectors and matrices are as follows: $x_k \in \mathrm{R}^m$, $d_k \in \mathrm{R}^m$, $u_k \in \mathrm{R}^p$, $y_k \in \mathrm{R}^q$, $w_k \in \mathrm{R}^m$, $v_k \in \mathrm{R}^q$, dim$[A_k] = m \times m$, dim$[B_k] = m \times p$, dim$[C_k] = q \times m$.

Assumptions:

- The process noise and the measurement noise are Gaussian noises with zero means and they are uncorrelated with each other.

$$w_k \sim (0, R_{w,k}); \quad v_k \sim (0, R_{v,k}); \quad E[w_k v_k^T] = 0 \tag{2.52}$$

- The dual-rate ratio r is a constant integer.
- The system is fully observable.
- The uncertainty is assumed to be written as:

$$\Delta A_k = H_k F_k E_k \tag{2.53}$$

where H_k and E_k are known matrices with appropriate dimensions, F_k is a bounded matrix, $F_k F_k^T \leq I$.

The following robust filter is proposed to the dual-rate system:

$$\hat{x}_{k+1} = \left(A_k + \Delta A_{e,k} \right) \hat{x}_k + L_{e,k} \left(y_k - C_k \hat{x}_k \right) + \hat{d}_k \tag{2.54}$$

where $\Delta A_{e,k}$ and $L_{e,k}$ are filter parameters to be designed such that the filter is optimal to some extent. $\hat{x}_k$ is the estimated state, $\hat{d}_k$ is the estimated unknown input.

2.4.2 Disturbance accommodation for unknown input estimation

In this section, utilizing the idea of "disturbance accommodation", we assume that:

$$d_{k+1} = A_{d,k} d_k + w_{d,k} \tag{2.55}$$

where $A_{d,k}$ is the state matrix of the disturbance process. $w_{d,k}$ is a Gaussian noise with zero means. $x_{d,k}$ $\in R^m$, $w_{d,k} \in R^m$, $\dim[A_{d,k}] = m \times m$. The noise $w_{d,k}$ is assumed to be uncorrelated with w_k and v_k:

$$w_{d,k} \sim \left(0, R_{wd,k} \right); \quad E\left[w_{d,k} w_k^T \right] = 0; \quad E\left[w_{d,k} v_k^T \right] = 0 \tag{2.56}$$

If $A_{d,k}$ is selected as the unity matrix, the disturbance term becomes a random-walk process.

From (2.50) and (2.55) the following augmented system is established:

$$\begin{cases} X_{k+1}^* = \left(A_k^* + \Delta A_k^* \right) X_k^* + W_k^* \\ Y_k^* = C_k^* X_k^* + \delta_k^* V_k^* \end{cases} \tag{2.57}$$

$$X_k^* = \begin{bmatrix} x_k \\ d_k \end{bmatrix}, \quad Y_k^* = y_k, \quad W_k^* = \begin{bmatrix} w_k \\ w_{d,k} \end{bmatrix}, \quad V_k^* = v_k \tag{2.58}$$

$$A_k^* = \begin{bmatrix} A_k & I \\ 0 & A_{d,k} \end{bmatrix}, \quad \Delta A_k^* = \begin{bmatrix} \Delta A_k & 0 \\ 0 & 0 \end{bmatrix}, \quad C_k^* = [C_k \quad 0], \quad \delta_k^* = \delta_k \tag{2.59}$$

We can see that the system with unknown input in (2.50) is transformed to the system (2.57) which has the same form as the system expressed in (2.22). Therefore, the problem of this section can be solved by the filtering scheme in the previous section as follows:

$$\hat{X}_{k+1}^* = \left(A_k^* + \Delta A_{e,k}^* \right) \hat{X}_k^* + L_{e,k}^* \left(Y_k^* - C_k^* \hat{X}_k^* \right) \tag{2.60}$$

From (2.58) and (2.59), the state x_k is estimated as follows:

$$\hat{x}_{k+1} = \left(A_k + \Delta A_{e,k} \right) \hat{x}_k + L_{e,k} \left(y_k - C_k \hat{x}_k \right) + \hat{d}_k \tag{2.61}$$

The disturbance d_k is estimated as:

$$\hat{d}_{k+1} = A_{d,k} \hat{d}_k + L_{ed,k} \left(y_k - C_k \hat{x}_k \right) \tag{2.62}$$

where $L_{e,k}$ and $L_{ed,k}$ are the estimation gains associating with the state and the disturbance, respectively.

We have $L_{e,k}^* = \begin{bmatrix} L_{e,k}^T & L_{ed,k}^T \end{bmatrix}^T$.

2.5 Discussion

In this chapter we study the Kalman filter for dual-rate estimation. The algorithms are developed through two points of view: 1) Disturbance accommodation. 2) Minimization of the estimation error covariance considering the norm-bounded uncertainty model. After studying each issue separately, we pay the effort to combine two schemes together to design the dual-rate estimation of a system with both the model uncertainty and the unknown input.

Instead of holding the innovation, the disturbance accommodation Kalman filter uses the estimated disturbance to maintain the correction when the low-rate measurement is unavailable. This estimation method will be verified and compared with other dual-rate estimations in Chapter 5 – motion control of electric vehicle using GPS in which the measurements from GPS receiver are updated at low-rate in comparison with the control period of the electric motors.

Chapter 3:
Time-delay Compensation Kalman Filter

"Delay is preferable to error."

Thomas Jefferson

3.1 Introduction

In this chapter, we will study the Kalman filter for handling the delayed-measurement. To deal with the large-time-delay while maintaining the affordable computational cost of the algorithm, the goals of the study are as follows:

- The algorithm does not increase the dimension of the system.
- The algorithm does not require to solve a series of Riccati equations in real-time.
- The algorithm does not include a cascade configuration as the Kalman filter followed by a d-step predictor.
- The estimation gain is optimal to some extent to assure the optimality and the stability.

In order to achieve the above goals, we propose the upper-bound Kalman filter in which the upper-bound of the estimation error covariance is derived using the μ-gain to obtain the estimation gains. The filter algorithm is almost the same as the standard Kalman filter.

Two cases of study are examined. The upper-bound Kalman filter is firstly applied to the system with delayed measurements, and then, the system with both delayed and non-delayed measurement. A simulation study is performed to verify the proposed algorithm.

3.2 Estimation with delayed measurements
3.2.1 System modeling and problem statement

We consider the following linear discrete-time system:

$$x_{k+1} = A_k x_k + B_k u_k + w_k \tag{3.1}$$

$$y_k = C x_{k-d} + v_k \tag{3.2}$$

where $x_k \in R^n$, $u_k \in R^m$, and $y_k \in R^p$. They represent the state, the input and the output vector,

respectively. A_k, B_k, and C are the state matrix, the input matrix, and the measurement matrix with appropriate dimensions. w_k and v_k are the process noise and the measurement. They are assumed to be Gaussian noises with zero means, their covariance matrices are $R_{w,k}$ and $R_{v,k}$. It is assumed that w_k and v_k are uncorrelated with each other. We also assume that the number of the delayed samples d is a known constant integer.

The estimation algorithm can be preliminarily proposed as follows:

- If $k < d$, the output (because it is delayed) is still unavailable. Therefore, the estimation is trivially performed by predicting from the given initial state through the dynamics expressed in (3.1).

- If $k \geq d$, the following filter is proposed including two stages as the Kalman filter:

    Prediction:

$$\hat{x}_{k|k-1} = A_{k-1}\hat{x}_{k-1|k-1} + B_{k-1}u_{k-1} \tag{3.3}$$

    Correction:

$$\hat{x}_{k|k} = \hat{x}_{k|k-1} + L_k\left(y_k - C\hat{x}_{k-d|k-d-1}\right) \tag{3.4}$$

where $\hat{x}_{k|k-1}$ is the predicted state, $\hat{x}_{k|k}$ is the corrected state, L_k is the estimation gain. The predicted state at the period k-d is stored to calculate the innovation at the present period.

Define the prediction error, the correction error, and their covariance matrices as:

$$\tilde{x}_{k|k-1} = x_k - \hat{x}_{k|k-1} \tag{3.5}$$

$$\tilde{x}_{k|k} = x_k - \hat{x}_{k|k} \tag{3.6}$$

$$\tilde{P}_{k|k-1} = E\left[\tilde{x}_{k|k-1}\tilde{x}_{k|k-1}^T\right] \tag{3.7}$$

$$\tilde{P}_{k|k} = E\left[\tilde{x}_{k|k}\tilde{x}_{k|k}^T\right] \tag{3.8}$$

Problem P.3.1: Given the filter expressed in (3.3) and (3.4), find the upper-bound of the correction error covariance and the estimation gain L_k to minimize the upper-bound.

3.2.2 Upper-bound of the estimation error covariance

From (3.1) ~ (3.8), at period k, the following dynamics are obtained:

$$\tilde{x}_{k|k-1} = A_{k-1}\tilde{x}_{k-1|k-1} + w_{k-1} \tag{3.9}$$

$$\tilde{x}_{k|k} = \tilde{x}_{k-1|k-1} - L_k C\tilde{x}_{k-d|k-d-1} - L_k v_k \tag{3.10}$$

$$\tilde{P}_{k|k-1} = A_{k-1}\tilde{P}_{k-1|k-1}A_{k-1}^T + R_{w,k-1} \tag{3.11}$$

$$\tilde{P}_{k|k} = \tilde{P}_{k|k-1} + L_k C\tilde{P}_{k-d|k-d-1}C^T L_k^T + L_k R_{v,k}L_k^T - E\left[\tilde{x}_{k|k-1}\tilde{x}_{k-d|k-d-1}^T\right]C^T L_k^T - L_k C E\left[\tilde{x}_{k-d|k-d-1}\tilde{x}_{k|k-1}^T\right] \tag{3.12}$$

In the same way we can write the dynamics of the prediction errors and the correction errors from the period k-d up to the period k. From all of these equations, $\tilde{P}_{k|k}$ is derived as:

$$\tilde{P}_{k|k} = \tilde{P}_{k|k-1} + L_k C \tilde{P}_{k-d|k-d-1} C^T L_k^T + L_k R_{v,k} L_k^T - \left(\prod_{j=1}^{d} A_{k-j}\right) \tilde{P}_{k-d|k-d-1} C^T L_k^T - L_k C \tilde{P}_{k-d|k-d-1}^T \left(\prod_{j=1}^{d} A_{k-j}\right)^T$$

$$+ \sum_{i=0}^{d-1} \left[\left(\prod_{j=1}^{d-i} A_{k-j}\right) L_{k-d+i} C E\left[\tilde{x}_{k-2d+i|k-2d-1+i} \tilde{x}_{k-d|k-d-1}^T\right] C^T L_k^T \right]$$

$$+ \sum_{i=0}^{d-1} \left[L_k C E\left[\tilde{x}_{k-d|k-d-1} \tilde{x}_{k-2d+i|k-2d-1+i}^T\right] C^T L_{k-d+i}^T \left(\prod_{j=1}^{d-i} A_{k-j}\right)^T \right]$$

$$(3.13)$$

It is very complex to obtain the covariance $E\left[\tilde{x}_{k-2d+i|k-2d-1+i} \tilde{x}_{k-d|k-d-1}^T\right]$ precisely (*i* from 0 to *d*-1).

Therefore, it is hard to derive the prediction error covariance. However, in Kalman filter, the update equation of the prediction covariance is desirable to design the estimation gain. To overcome this problem, we will try to find the upper-bound of the correction error covariance. Then, if we can design the estimation gain to minimize this upper-bound, we can say that the filter is "optimal" to some extent.

Apply the **lemma L1** (see the Appendix) to the last two terms in (3.13), we can always find the positive number $\mu_{k,i}$ such that:

$$\tilde{P}_{k|k} \leq \tilde{P}_{k|k-1} + \left(1 + \sum_{i=0}^{d-1} \frac{1}{\mu_{k,i}}\right) L_k C \tilde{P}_{k-d|k-d-1} C^T L_k^T + L_k R_{v,k} L_k^T$$

$$- \left(\prod_{j=1}^{d} A_{k-j}\right) \tilde{P}_{k-d|k-d-1} C^T L_k^T - L_k C \tilde{P}_{k-d|k-d-1}^T \left(\prod_{j=1}^{d} A_{k-j}\right)^T$$

$$+ \sum_{i=0}^{d-1} \left[\mu_{k,i} \left(\prod_{j=1}^{d-i} A_{k-j}\right) L_{k-d+i} C \tilde{P}_{k-2d+i|k-2d-1+i} C^T L_{k-d+i}^T \left(\prod_{j=1}^{d-i} A_{k-j}\right)^T \right]$$

$$(3.14)$$

Define the following covariance sequence:

Initial covariance:

$$\Omega_{0|0} = \tilde{P}_{0|0} \tag{3.15}$$

Update equations of the sequence:

$$\Omega_{k|k-1} = A_{k-1} \Omega_{k-1|k-1} A_{k-1}^T + R_{w,k-1} \tag{3.16}$$

$$\Omega_{k|k} = \Omega_{k|k-1} + \left(1 + \sum_{i=0}^{d-1} \frac{1}{\mu_{k,i}}\right) L_k C \Omega_{k-d|k-d-1} C^T L_k^T + L_k R_{v,k} L_k^T$$

$$- \left(\prod_{j=1}^{d} A_{k-j}\right) \Omega_{k-d|k-d-1} C^T L_k^T - L_k C \Omega_{k-d|k-d-1}^T \left(\prod_{j=1}^{d} A_{k-j}\right)^T$$

$$+ \sum_{i=0}^{d-1} \left[\mu_{k,i} \left(\prod_{j=1}^{d-i} A_{k-j}\right) L_{k-d+i} C \Omega_{k-2d+i|k-2d-1+i} C^T L_{k-d+i}^T \left(\prod_{j=1}^{d-i} A_{k-j}\right)^T \right]$$
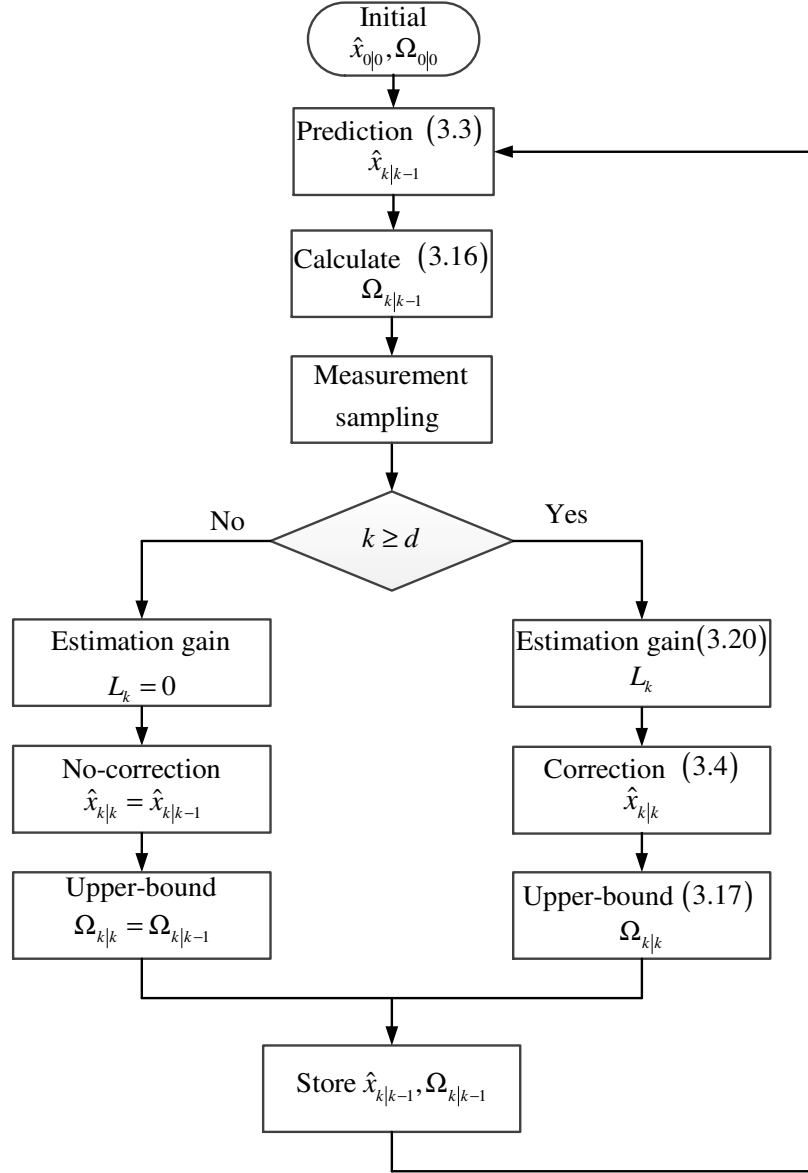
$$(3.17)$$

Fig. 3.1 Flow chart of the Kalman filter for system with delayed measurements.

From the inequality (3.14), it is transparent that the above sequence makes an upper-bound of the correction error covariance. In other words:

$$\tilde{P}_{k|k} \leq \Omega_{k|k} \tag{3.18}$$

The estimation gain L_k is design such that it minimizes the upper-bound:

$$\frac{\partial \Omega_{k|k}}{\partial L_k} = 0 \tag{3.19}$$

Substitute (3.17) into (3.19) and solve this equation, the estimation gain is obtained as:

$$L_k = \left(\prod_{j=1}^{d} A_{k-j} \right) \Omega_{k-d|k-d-1} C^T \left[\left(1 + \sum_{i=0}^{d-1} \frac{1}{\mu_{k,i}} \right) C\Omega_{k-d|k-d-1} C^T + R_{v,k} \right]^{-1} \tag{3.20}$$

The **problem P.3.1** is solved completely.

3.2.3 Algorithm and discussion

The flow chart of the estimation algorithm is shown in Fig. 3.1. When k is still smaller than d, the state is obtained by only the prediction. Since k is equal to d, the state is estimated through both the prediction and correction stages.

In (3.20), if d is zero or the measurement is non-delayed, (3.20) becomes formulation of the standard Kalman filter:

$$L_k = \Omega_{k|k-1} C^T \left[C\Omega_{k|k-1} C^T + R_{v,k} \right]^{-1} \tag{3.21}$$

If $\mu_{k,i} = \mu_k$ for $i \in [0, d\text{-}1]$, the estimation gain formulation can be rewritten as:

$$L_k = \left(\prod_{j=1}^{d} A_{k-j} \right) \Omega_{k-d|k-d-1} C^T \left[\left(1 + \frac{d}{\mu_k} \right) C\Omega_{k-d|k-d-1} C^T + R_{v,k} \right]^{-1} \tag{3.22}$$

In the proposed upper-bound Kalman filter, the gains $\mu_{k,i}$ are introduced as the tuning parameters. With more tuning degree, we can flexibly design the estimation gain to achieve the good performance of the estimation. This is an advantage of the proposed filter.

3.3 Estimation with delayed and non-delayed measurements

3.3.1 System modeling and problem statement

We examine the following linear discrete-time state space model with two measurement vectors:

$$x_{k+1} = A_k x_k + B_k u_k + w_k \tag{3.23}$$
$$y_{1,k} = C_1 x_k + v_{1,k} \tag{3.24}$$
$$y_{2,k} = C_2 x_{k-d} + v_{2,k} \tag{3.25}$$

where other terms can be defined as in Case 1, $y_{1,k} \in R^{p1}$ and $y_{2,k} \in R^{p2}$ represent the non-delayed and delayed measurement, respectively. $v_{1,k}$ an and $v_{2,k}$ are Gaussian noises with zero means. Their covariance matrices are $R_{v1,k}$ and $R_{v2,k}$. They are assumed to be uncorrelated with each other and with the process noise w_k.

The estimation algorithm can be preliminarily proposed as follows:

- If $k < d$, the delayed measurement is still unavailable. Therefore, the estimation is trivially performed by using the non-delayed measurement through the standard Kalman filter.

- If $k \geq d$, the following filter is proposed:

  Prediction:

$$\hat{x}_{k|k-1} = A_{k-1}\hat{x}_{k-1|k-1} + B_{k-1}u_{k-1} \tag{3.26}$$

Correction:

$$\hat{x}_{k|k} = \hat{x}_{k|k-1} + L_{1,k}\left(y_{1,k} - C_1\hat{x}_{k|k-1}\right) + L_{2,k}\left(y_{2,k} - C_2\hat{x}_{k-d|k-d-1}\right) \tag{3.27}$$

where $\hat{x}_{k|k-1}$ is the predicted state, $\hat{x}_{k|k}$ is the corrected state, $L_{1,k}$ is the estimation gain associated with the non-delayed measurement, and $L_{2,k}$ is the estimation gain associated with the delayed measurement. The predicted state at the period k-d is stored to calculate the innovation associated with the delayed measurement at the present period.

Problem P.3.2: Given the filter expressed in (3.26) and (3.27), find the upper-bound of the correction error covariance and the estimation gain $L_{1,k}$ and $L_{2,k}$ to minimize the upper-bound.

3.3.2 Upper-bound of estimation error covariance

From (3.23)~(3.27), at the period k, the dynamics of the prediction error, correction error, and their covariance matrices are derived as:

$$\tilde{x}_{k|k-1} = A_{k-1}\tilde{x}_{k-1|k-1} + w_{k-1} \tag{3.28}$$

$$\tilde{x}_{k|k} = \left(I - L_{1,k}C_1\right)\tilde{x}_{k-1|k-1} - L_{2,k}C_2\tilde{x}_{k-d|k-d-1} - L_{1,k}v_k - L_{2,k}v_k \tag{3.29}$$

$$\tilde{P}_{k|k-1} = A_{k-1}\tilde{P}_{k-1|k-1}A_{k-1}^T + R_{w,k-1} \tag{3.30}$$

$$\tilde{P}_{k|k} = \left(I - L_{1,k}C_1\right)\tilde{P}_{k|k-1}\left(I - L_{1,k}C_1\right)^T + L_{2,k}C_2\tilde{P}_{k-d|k-d-1}C_2^T L_{2,k}^T + L_{1,k}R_{v1,k}L_{1,k}^T + L_{2,k}R_{v2,k}L_{2,k}^T$$
$$- \left(I - L_{1,k}C_1\right)E\left[\tilde{x}_{k|k-1}\tilde{x}_{k-d|k-d-1}^T\right]C_2^T L_{2,k}^T - L_{2,k}C_2 E\left[\tilde{x}_{k-d|k-d-1}\tilde{x}_{k|k-1}^T\right]\left(I - L_{1,k}C_1\right)^T \tag{3.31}$$

In the same way, we can derive the prediction error and the correction error from the period k-d up to the period k. Combine all these equations together, we can derive the covariance of the correction error as:

$$\tilde{P}_{k|k} = \left(I - L_{1,k}C_1\right)\tilde{P}_{k|k-1}\left(I - L_{1,k}C_1\right)^T + L_{2,k}C_2\tilde{P}_{k-d|k-d-1}C_2^T L_{2,k}^T + L_{1,k}R_{v1,k}L_{1,k}^T + L_{2,k}R_{v2,k}L_{2,k}^T$$
$$+ \left(I - L_{1,k}C_1\right)\Gamma_k C_2^T L_{2,k}^T + L_{2,k}C_2\Gamma_k^T\left(I - L_{1,k}C_1\right)^T \tag{3.32}$$
$$- \left(I - L_{1,k}C_1\right)\left(\prod_{j=1}^{d}\Psi_{1,k-j}\right)\tilde{P}_{k-d|k-d-1}C_2^T L_{2,k}^T - L_{2,k}C_2\tilde{P}_{k-d|k-d-1}\left(\prod_{j=1}^{d}\Psi_{1,k-j}\right)^T\left(I - L_{1,k}C_1\right)^T$$

where

$$\Psi_{1,k-j} = A_{k-j}\left(I - L_{1,k-j}C_1\right) \tag{3.33}$$

$$\Gamma_k = \sum_{i=0}^{d-1}\left[\left(\prod_{j=1}^{d-i-1}\Psi_{k-j}\right)A_{k-d+i}L_{2,k-d+i}C_2 E\left[\tilde{x}_{k-2d+i|k-2d-1+i}\tilde{x}_{k-d|k-d-1}^T\right]\right] \tag{3.34}$$

Again, it is very complicated to derive the covariance $E\left[\tilde{x}_{k-2d+i|k-2d-1+i}\tilde{x}_{k-d|k-d-1}^T\right]$. Utilizing the **lemma L1** and the same scheme as in the previous section, the upper-bound of the estimation error

covariance is obtained as:

    Initial covariance:

$$\Omega_{0|0} = \tilde{P}_{0|0} \tag{3.35}$$

    Update equations of the sequence:

$$\Omega_{k|k-1} = A_{k-1}\Omega_{k-1|k-1}A_{k-1}^T + R_{w,k-1} \tag{3.36}$$

$$\Omega_{k|k} = \bar{L}_k\bar{M}_k\bar{L}_k^T - \bar{L}_k\bar{N}_k^T - \bar{N}_k\bar{L}_k^T + \Omega_{k|k-1} + Q_k \tag{3.37}$$

where

$$\bar{L}_k = \begin{bmatrix} L_{1,k} & L_{2,k} \end{bmatrix} \tag{3.38}$$

$$\bar{M}_k = \begin{bmatrix} C_1\left(\Omega_{k|k-1} + Q_k\right)C_1^T + R_{v1,k} & C_1 S_k \Omega_{k-d|k-d-1}C_2^T \\[2mm] C_2\Omega_{k-d|k-d-1}^T S_k^T C_1^T & \left(1 + \sum_{i=0}^{d-1}\frac{1}{\mu_{k,i}}\right)C_2\Omega_{k-d|k-d-1}C_2^T + R_{v2,k} \end{bmatrix} \tag{3.39}$$

$$\bar{N}_k = \begin{bmatrix} \left(\Omega_{k|k-1} + Q_k\right)C_1^T & S_k\Omega_{k-d|k-d-1}C_2^T \end{bmatrix} \tag{3.40}$$

$$S_k = \prod_{j=1}^{d}\Psi_{1,k-j} \tag{3.40}$$

$$Q_k = \sum_{i=0}^{d-1}\left[\mu_{k,i}\left(\prod_{j=1}^{d-i-1}\Psi_{k-j}\right)A_{k-d+i}L_{2,k-d+i}C_2\Omega_{k-2d+i|k-2d-1+i}C_2^T L_{2,k-d+i}^T A_{k-d+i}^T\left(\prod_{j=1}^{d-i-1}\Psi_{k-j}\right)^T\right] \tag{3.41}$$

    The estimation gains are designed such that they minimize the upper-bound of the estimation error covariance:

$$\frac{\partial \Omega_{k|k}}{\partial \bar{L}_k} = 0 \tag{3.42}$$

    Solving (3.42) we obtain:

$$\bar{L}_k = \bar{N}_k\bar{M}_k^{-1} \tag{3.43}$$

    The estimation gains can be written in the detailed form as:

$$\begin{bmatrix} L_{1,k} & L_{2,k} \end{bmatrix} = \begin{bmatrix} \left(\Omega_{k|k-1} + Q_k\right)C_1^T & S_k\Omega_{k-d|k-d-1}C_2^T \end{bmatrix}$$
$$\times \begin{bmatrix} C_1\left(\Omega_{k|k-1} + Q_k\right)C_1^T + R_{v1,k} & C_1 S_k \Omega_{k-d|k-d-1}C_2^T \\[2mm] C_2\Omega_{k-d|k-d-1}^T S_k^T C_1^T & \left(1 + \sum_{i=0}^{d-1}\frac{1}{\mu_{k,i}}\right)C_2\Omega_{k-d|k-d-1}C_2^T + R_{v2,k} \end{bmatrix}^{-1} \tag{3.44}$$

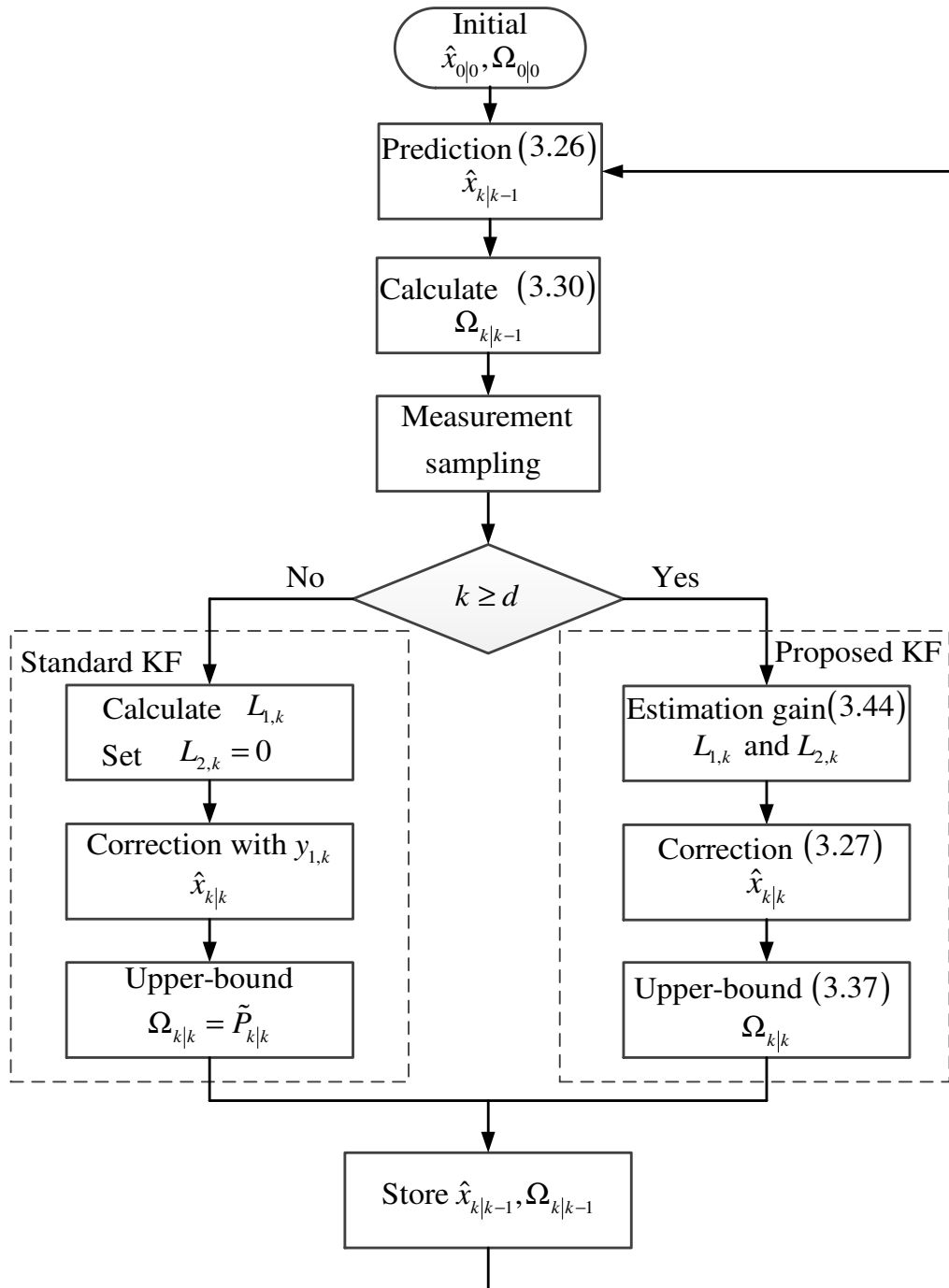   The **problem P.3.2** is solved completely.

Fig. 3.2 Flow chart of the Kalman filter for system with delayed and non-delayed measurements.

3.3.3 Algorithm and discussion

The flow chart of the estimation algorithm is shown in Fig. 3.2. When k is still smaller than d, the state is estimated by only the non-delayed measurements. Since k is equal to d, the state is estimated through both the delayed and the non-delayed measurements.

In (3.44), if d is zero or the measurement is non-delayed, (3.44) becomes the formulation of the standard Kalman filter:

$$\begin{bmatrix} L_{1,k} & L_{2,k} \end{bmatrix} = \tilde{P}_{k|k-1} \begin{bmatrix} C_1 \\ C_2 \end{bmatrix}^T \left(\begin{bmatrix} C_1 \\ C_2 \end{bmatrix} \tilde{P}_{k|k-1} \begin{bmatrix} C_1 \\ C_2 \end{bmatrix}^T + \begin{bmatrix} R_{v1,k} & 0 \\ 0 & R_{v,2k} \end{bmatrix} \right)^{-1} \tag{3.45}$$

In (3.32), if we neglect the covariance (3.43) to approximately calculate the estimation error covariance, the estimation gain can be calculated in the following simple form:

$$\begin{bmatrix} L_{1,k} & L_{2,k} \end{bmatrix} = \begin{bmatrix} \tilde{P}_{k|k-1} C_1^T & S_k \tilde{P}_{k-d|k-d-1} C_2^T \end{bmatrix} \times \begin{bmatrix} C_1 \tilde{P}_{k|k-1} C_1^T + R_{v1,k} & C_1 S_k \tilde{P}_{k-d|k-d-1} C_2^T \\ C_2 \tilde{P}_{k-d|k-d-1}^T S_k^T C_1^T & C_2 \tilde{P}_{k-d|k-d-1} C_2^T + R_{v2,k} \end{bmatrix}^{-1} \tag{3.46}$$

3.4 Simulation verification

3.4.1 A case of study

In this chapter, we will examine a case of study as follows: A linear stochastic discrete-time system includes two states x_1 and x_2 is established with the fundamental sampling time $T_c = 1$ms. Only the state x_2 is measurable. However, the measurement of x_2 is delayed, the time-delay is $T_d = 30T_c$. This means that the time-delay is relatively large in comparison with the fundamental sampling time. Moreover, the nominal model for estimation design is not perfectly precise. The problem is to estimate both x_1 and x_2 as accurate as possible.

The real model:

$$\begin{cases} x_k = Ax_{k-1} + Bu_{k-1} + w_k \\ \quad y_k = Cx_{k-d} + v_k \end{cases} \tag{3.47}$$

where

$$x_k = \begin{bmatrix} x_{1,k} & x_{2,k} \end{bmatrix}^T, \quad u_k = \begin{bmatrix} \delta_k \end{bmatrix} \tag{3.48}$$

$$A = \begin{bmatrix} 0.9870 & -0.0014 \\ -0.1440 & 0.9585 \end{bmatrix}, \quad B = \begin{bmatrix} 0.0065 \\ 0.2880 \end{bmatrix}, \quad C = \begin{bmatrix} 0 & 1 \end{bmatrix} \tag{3.49}$$

The number of the delayed samples is $d = 30$. w_k and v_k are Gaussian noises with zero means. The initial state is $x_0 = \begin{bmatrix} 0 & 0 \end{bmatrix}^T$. The input δ is a sinusoidal signal with the frequency of 0.25 Hz and the amplitude of $5\pi/180$. To simulate the uncertainty, the nominal model for the designing the estimator is selected as:

$$A_n = \begin{bmatrix} 0.9882 & -0.0013 \\ -0.1312 & 0.9622 \end{bmatrix}, \quad B_n = \begin{bmatrix} 0.0059 \\ 0.2624 \end{bmatrix} \tag{3.50}$$

3.4.2 Simulation results

Four estimation methods are designed and performed for comparison. As the number of the delayed samples is large ($d = 30$), the "state augmentation" method is not applicable.

1) The standard Kalman filter (Standard KF): the time-delay is not handled.

2) The cascade estimation (Cascade KF): It is a standard Kalman filter plus a d-step predictor.

3) The measurement extrapolation Kalman filter (MeaExtra KF): As shown in Chapter 1 and the formulation (1.19), a non-delayed measurement is extrapolated from the delayed-measurement. However, the authors of this method neglect the covariance $E\left[\tilde{x}_{k-2d+i|k-2d-1+i} \tilde{x}_{k-d|k-d-1}^T \right]$ to simply obtain the estimation error covariance as:

$$\tilde{P}_{k|k} \approx \tilde{P}_{k|k-1} + L_k C \tilde{P}_{k-d|k-d-1} C^T L_k^T + L_k R_{v,k} L_k^T - \left(\prod_{j=1}^{d} A_{k-j} \right) \tilde{P}_{k-d|k-d-1} C^T L_k^T - L_k C \tilde{P}_{k-d|k-d-1}^T \left(\prod_{j=1}^{d} A_{k-j} \right)^T \tag{3.51}$$

Therefore, this method might fails to predict the estimation error covariance, and the estimation gain is not optimal.

4) The proposed estimation (Upper-bound KF): Because it is hard to derive the covariance $E\left[\tilde{x}_{k-2d+i|k-2d-1+i} \tilde{x}_{k-d|k-d-1}^T \right]$, we calculate the upper-bound of the estimation error covariance for designing the estimation gain. In this simulation, the gain $\mu_{k,i}$ is selected to be 0.8.

The estimation results of the Standard KF, the MeaExtra KF, and the Upper-bound KF are shown in Fig. 3.3. For the convenience of comparison, Fig. 3.4 shows a segment of these data for clearly comparison. Certainly, the Standard KF cannot compensate the time-delay and the estimated states are inaccurate. Especially, the estimation of the state x_1 by the Standard KF is considerably bad. In contrast, both the MeaExtra KF and the Upper-bound KF can handle the delayed measurement. However, as shown in Fig. 3.4, the Upper-bound KF attains the better estimation performance while the variation occurs in case of the MeaExtra KF. This phenomenal can be explained due to the fact that the MeaExtra KF fails to compute the estimation error covariance in every estimation period.

The estimation results of the Standard KF, the Cascade KF, and the Upper-bound KF are compared in Fig. 3.5 and Fig. 3.6 for a segment of the data. The Cascade KF shows the better results than the Standard KF, but the estimation error of this method is still bigger than that of the Upper-bound KF. This means that the d-step predictor is influenced by the model error.

From the simulation results, we can conclude that the Upper-bound KF is better than other three methods considering the large-time-delay and model uncertainties. The MeaExtra KF is not stable in long term, while the Cascade KF suffers from large estimation error.
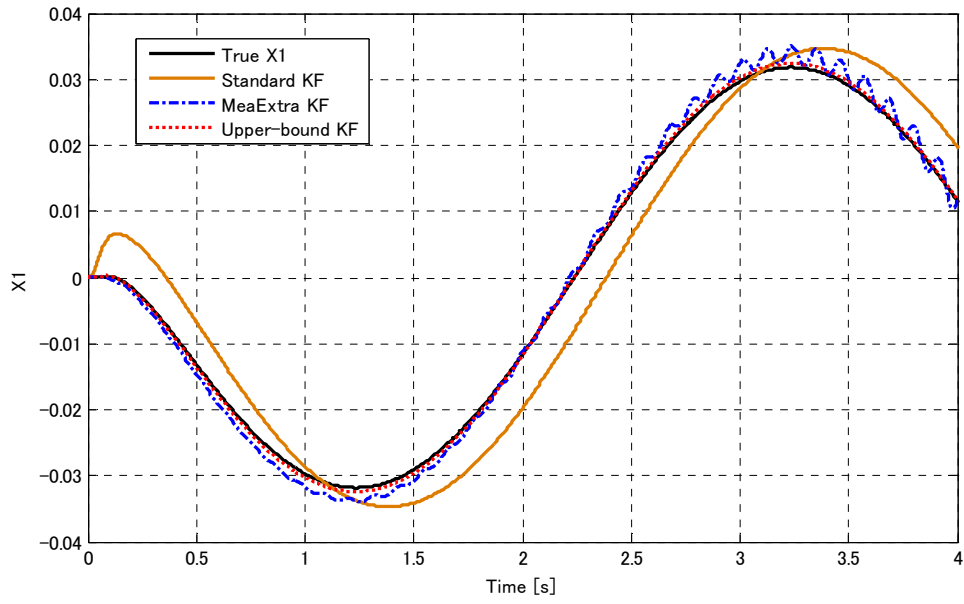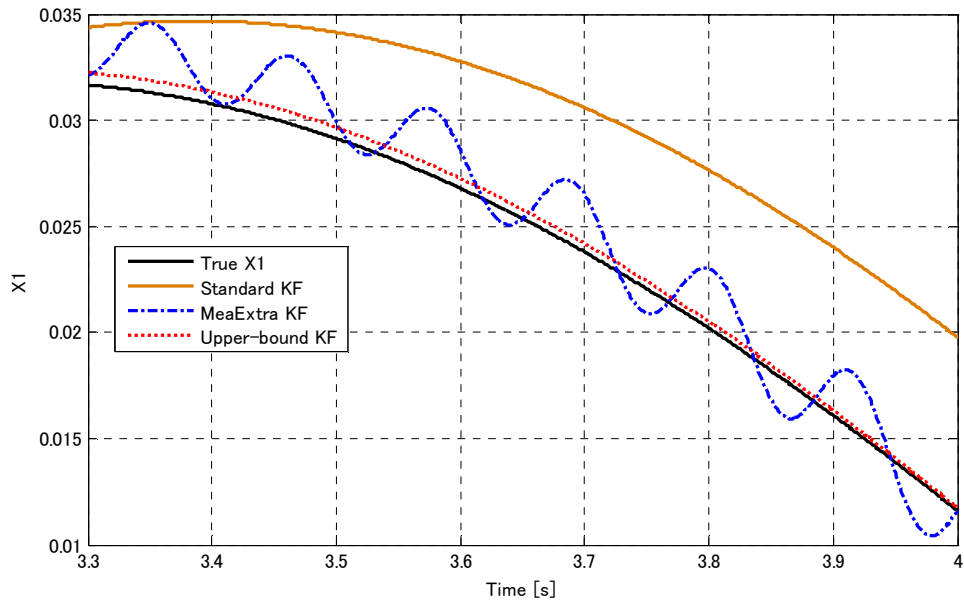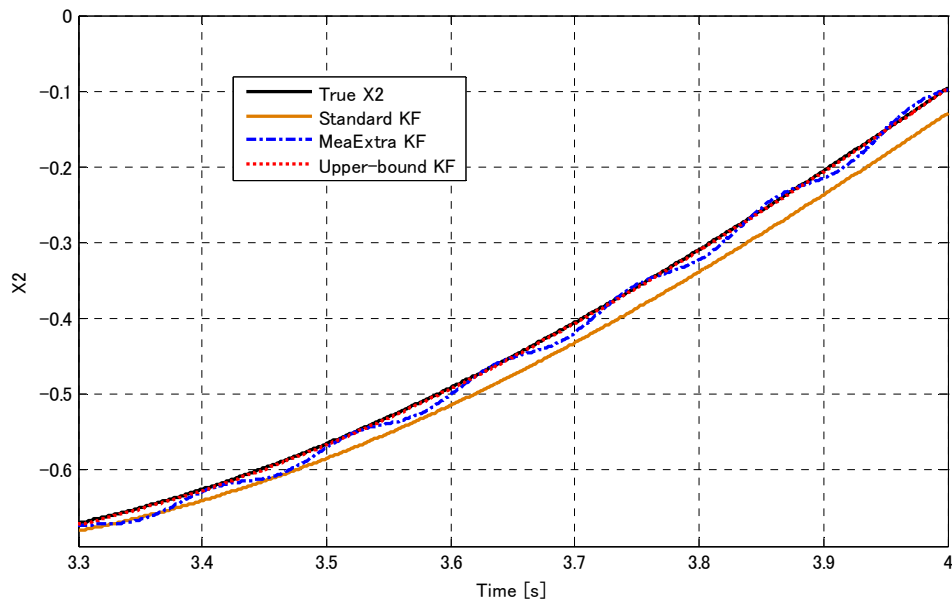
(a)
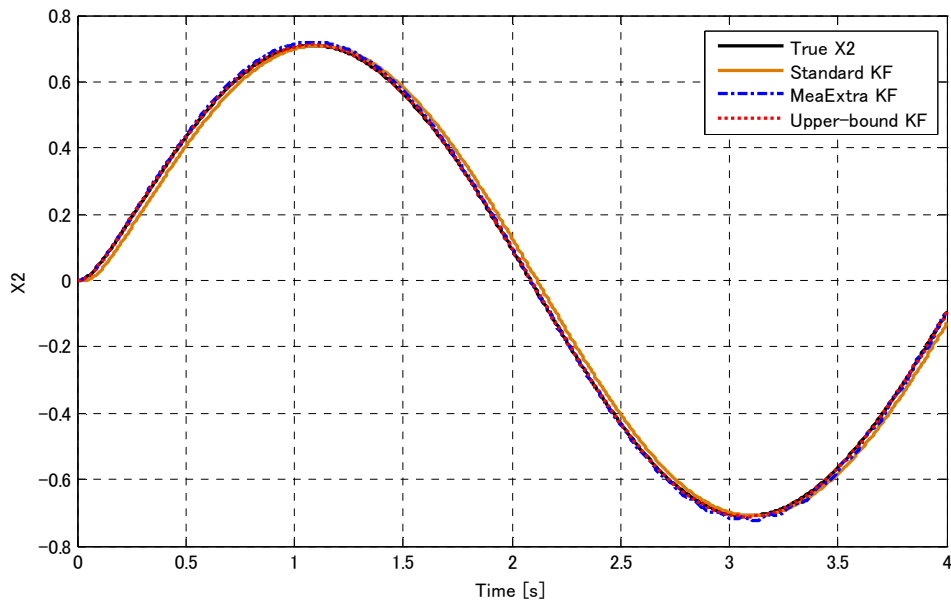
(b)

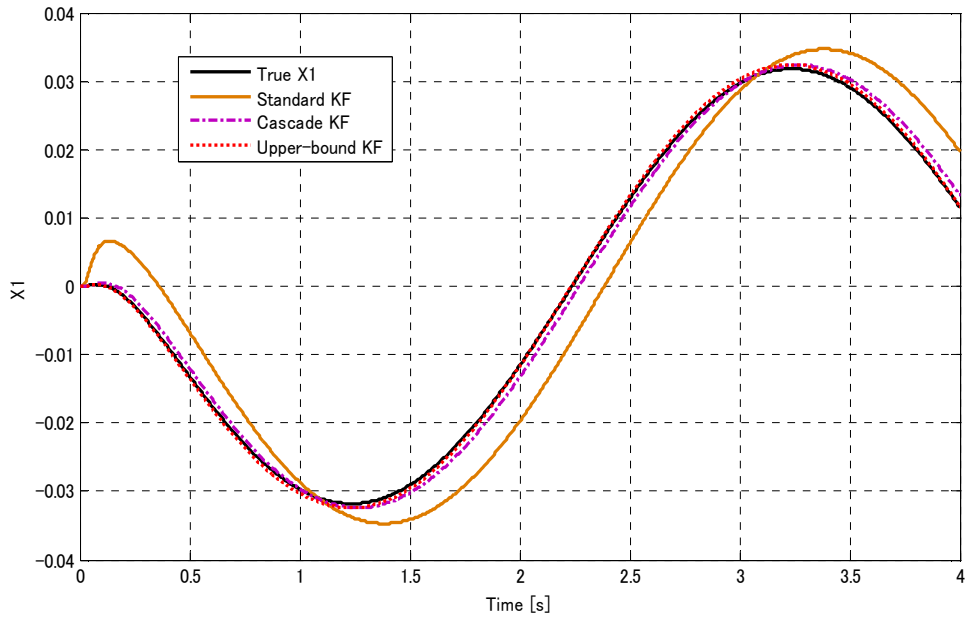Fig. 3.3 Simulation results: Standard KF, MeaExtra KF, and Upper-bound KF.
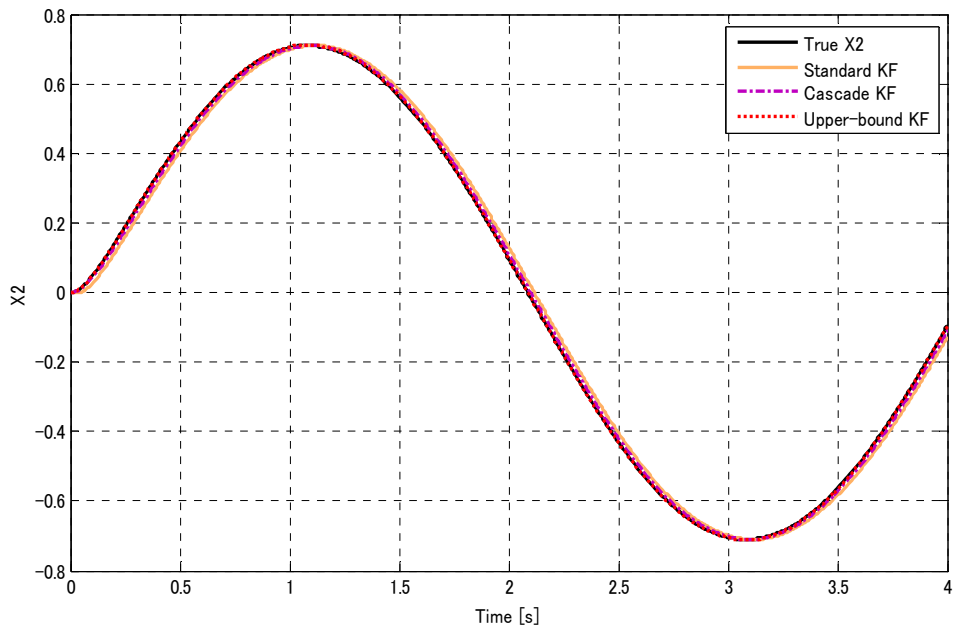
(a)

(b)

Fig. 3.4 Simulation results: Standard KF, MeaExtra KF, and Upper-bound KF (a part of the full data).
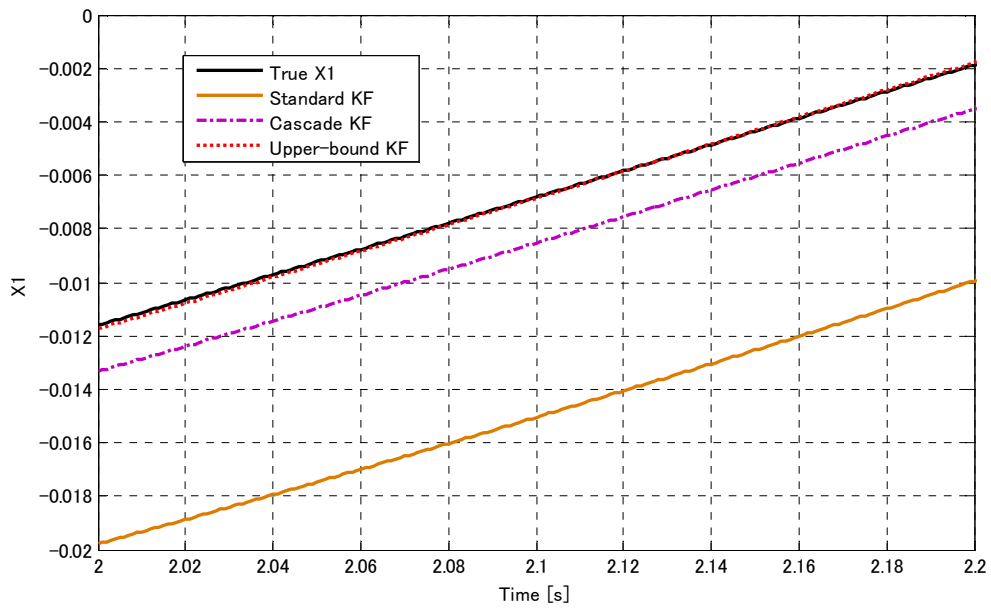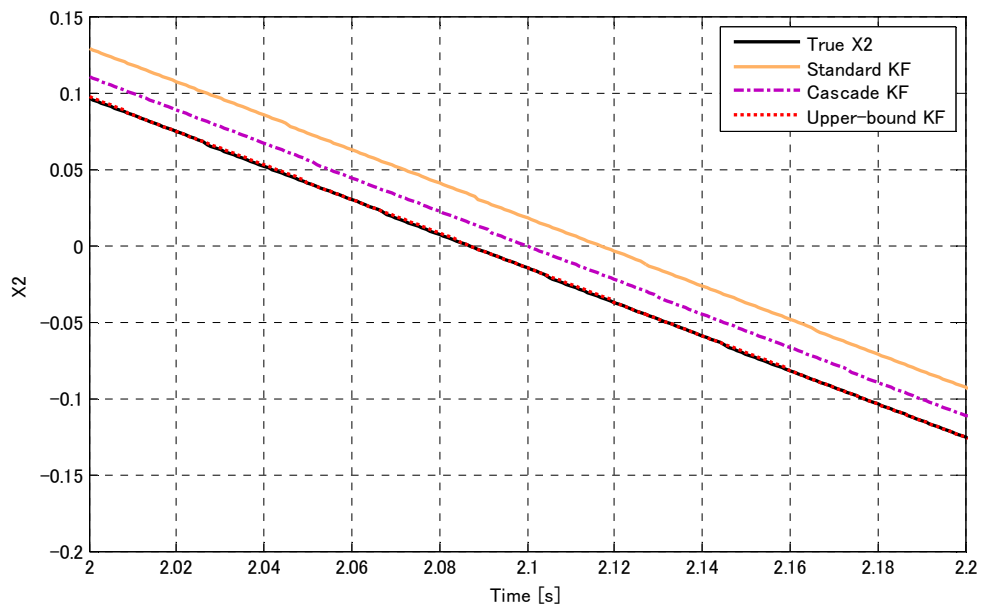
(a)

(b)

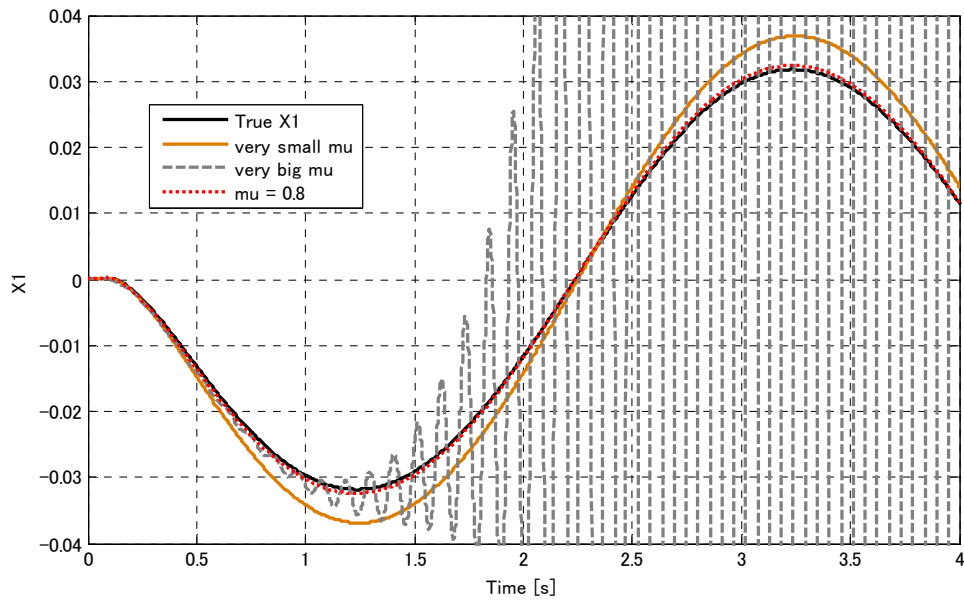Fig. 3.5 Simulation results: Standard KF, Cascade KF, and Upper-bound KF.
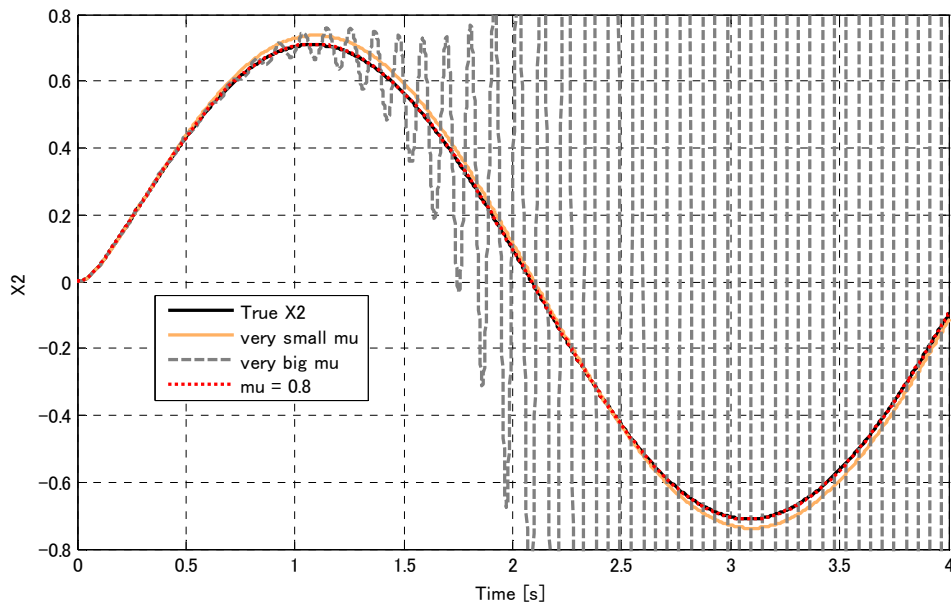
(a)

(b)

Fig. 3.6 Simulation results: Standard KF, Cascade KF, and Upper-bound KF (a part of the full data).

(a)

(b)

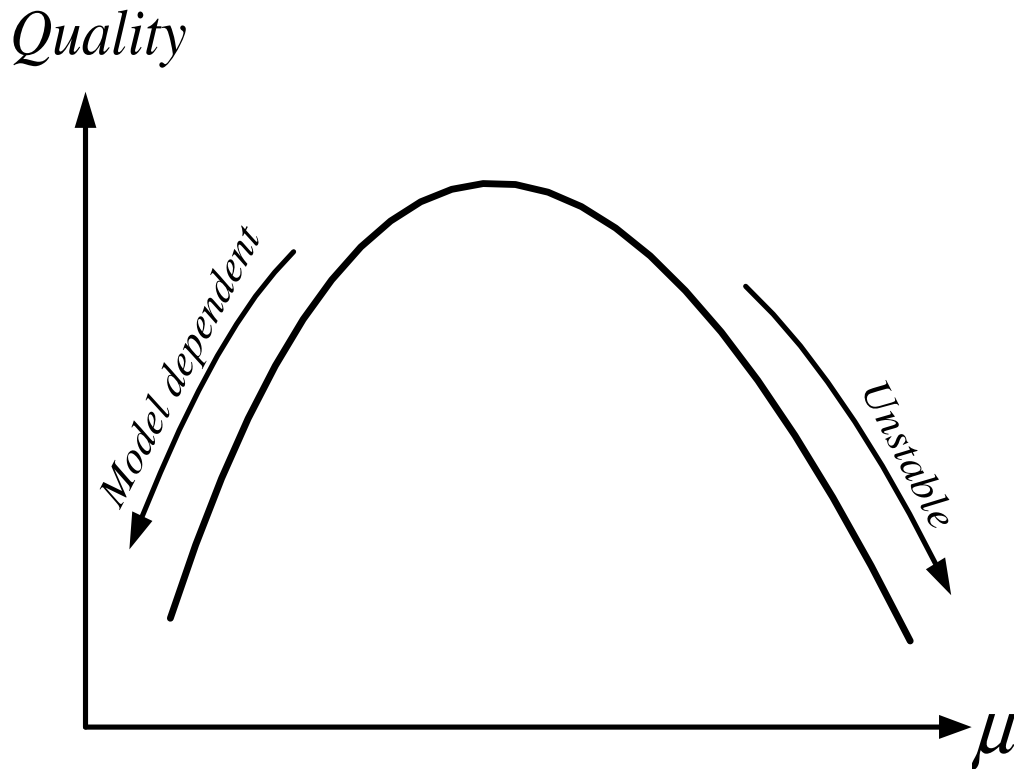Fig. 3.7 Simulation results of the Upper-bound KF at different μ-gains.

Quality

Fig. 3.8 Relationship between the μ-gain and the Upper-bound KF.

3.4.3 Estimation quality and μ-gain

It is desirable to known how the gain $\mu_{k,i}$ is design. We perform the simulations using different number of the gain $\mu_{k,i}$.

1) Case 1: $\mu_{k,i}$ is selected as a very small value, for instance $\mu_{k,i} \approx 0$.

2) Case 2: $\mu_{k,i}$ is selected as a relatively big value in comparison with case 1, such as $\mu_{k,i} = 10$.

3) Case 3: $\mu_{k,i}$ is selected as in the previous simulation: $\mu_{k,i} = 0.8$.

The simulation results are summarized in Fig. 3.7. If the gain $\mu_{k,i}$ (μ-gain) is close to zero, from (3.20), the estimation gain become close to zero as well. Consequently, the estimated state almost relies on the dynamics model. Because of the model uncertainty, the estimation result in Case 1 is inaccurate. On the other hand, if the gain $\mu_{k,i}$ is relatively big, the estimation gain also attains the big value. This results in the unstable estimation performance of Case 2. Case 3 shows the suitable selection of the gain $\mu_{k,i}$. Fig. 3.8 shows the relationship between the gain $\mu_{k,i}$ and the quality of the Upper-bound KF. The quality of the upper-bound KF is decreased when the μ-gain becomes too small or too big. There is the optimal value of the μ-gain that we have to design. In this study, the μ-gain is only obtained through trial-and-error test. In future works, the systematic method to obtain the optimal μ-gain and the online-tuning of the μ-gain will be considered.

3.5 Random-time-delay

In this section, we will study how the upper-bound Kalman filter is developed to the random-time-delay system. There are two possible cases: First, the time-delay is measurable; Second: the time-delay is uncertain.

3.5.1 Measurable time-delay

The system in which the time-delay varies can be expressed as:

$$\begin{cases} x_{k+1} = A_k x_k + B_k u_k + w_k \\ y_k = C x_{k-d(k)} + v_k \end{cases} \tag{3.52}$$

Assume that at period k, the number of delayed samples $d(k)$ is measurable. We can also assume that $d(k)$ has a certain upper and lower bound:

$$d_{\min} \leq d(k) \leq d_{\max} \tag{3.53}$$

The estimation algorithm is almost the same as the algorithm in Fig. 3.1. The difference is the size of the store is increased to capture the arrays of past time predicted state and past time upper-bound.

$$\begin{cases} \text{Array state:} = \left\{ \hat{x}_{k-i|k-i-1} \middle| i \in [d_{\min}, d_{\max}] \right\} \\ \text{Array covariance:} = \left\{ \Omega_{k-i|k-i-1} \middle| i \in [d_{\min}, d_{\max}] \right\} \end{cases} \tag{3.54}$$

At the period k, when the time-delay is known, the associated values in the arrays are used. For instance, the estimated state, the upper-bound of the estimation error covariance, and the estimation gain are calculated as:

$$\hat{x}_{k|k} = \hat{x}_{k|k-1} + L_k \left(y_k - C\hat{x}_{k-d(k)|k-d(k)-1} \right) \tag{3.55}$$

$$\begin{aligned} \Omega_{k|k} = {} & \Omega_{k|k-1} + \left(1 + \sum_{i=0}^{d(k)-1} \frac{1}{\mu_{k,i}} \right) L_k C \Omega_{k-d(k)|k-d(k)-1} C^T L_k^T + L_k R_{v,k} L_k^T \\ & - \left(\prod_{j=1}^{d(k)} A_{k-j} \right) \Omega_{k-d(k)|k-d(k)-1} C^T L_k^T - L_k C \Omega_{k-d(k)|k-d(k)-1}^T \left(\prod_{j=1}^{d(k)} A_{k-j} \right)^T \\ & + \sum_{i=0}^{d(k)-1} \left[\mu_{k,i} \left(\prod_{j=1}^{d(k)-i} A_{k-j} \right) L_{k-d(k)+i} C \Omega_{k-2d(k)+i|k-2d(k)-1+i} C^T L_{k-d(k)+i}^T \left(\prod_{j=1}^{d(k)-i} A_{k-j} \right)^T \right] \end{aligned} \tag{3.56}$$

$$L_k = \left(\prod_{j=1}^{d(k)} A_{k-j} \right) \Omega_{k-d(k)|k-d(k)-1} C^T \left[\left(1 + \sum_{i=0}^{d(k)-1} \frac{1}{\mu_{k,i}} \right) C \Omega_{k-d(k)|k-d(k)-1} C^T + R_{v,k} \right]^{-1} \tag{3.57}$$

3.5.2 Uncertain time-delay

In this case, the number of the delayed samples $d(k)$ is not known exactly. As suggest in [55], we assume that we can derive the time-delay's probability density function $f(t)$, for instance through experiments. From the probability density function, the probability ρ_i that $d(k)$ takes the number $d_i \in$

$[d_{min}, d_{max}]$ is obtained as:

$$\rho_i = \Pr\left(T_s d_i - \frac{T_s}{2} \leq T_{delay} \leq T_s d_i + \frac{T_s}{2}\right) = \int_{T_s d_i - \frac{T_s}{2}}^{T_s d_i + \frac{T_s}{2}} f(t)\,dt \tag{3.58}$$

where T_s is the sampling time of the delayed measurement.

Define $\hat{x}_{k|k}(i)$ is the estimated state when the measurement is d_i-sample-delay measurement. The estimated state $\hat{x}_{k|k}(i)$ is obtained using the upper-bound Kalman filter by setting the number of the delayed sample as d_i. The optimal estimated state is:

$$\hat{x}_{k|k} = \sum_{i=d_{min}}^{d_{max}} \rho_i \hat{x}_{k|k}(i) \tag{3.59}$$

In other words, the estimation algorithm includes $(d_{max} - d_{min} + 1)$ upper-bound Kalman filters. Certainly, more computational cost must be paid to deal with the uncertain time-delay problem.

If the probability density function of the time-delay is unknown, the problem is more difficulty. This problem is still open and would be dedicated to the future works of this study.

3.6 Discussion

In this chapter, a new Kalman filter considering the large-time-delay in the measurement is proposed. The key idea of the method is to introduce a μ-gain to obtain the upper-bound of the estimation error covariance for designing the estimation gain. The effectiveness of the proposed method in comparisons with other previous works is discussed through simulation study. The proposed method is shown to be more robust and stable than the "cascade estimation" or the "measurement extrapolation estimation". However, the μ-gain is just selected by trial-and-error and it is kept as a constant. Therefore, it is interesting to examine the online tuning of the μ-gain in the future study. Finally, a little discussion on the random-time-delay issue is given.

The proposed upper-bound Kalman filter will be applied to the visual servo system for chip mounting machine in the Chapter 6. In this system, the information from the image processing unit is delayed. Therefore, the upper-bound Kalman filter is used to handle the delay and estimate the target position accurately.

Chapter 4:

Simultaneous Estimation of Parameter and State

"You can, for example, never foretell what any one man will do, but you can say
with precision what an average number will be up to. Individuals vary,
but percentages remain constant. So says the statistician."

Sherlock Holmes (The Sign of Four)

4.1 Introduction

In this chapter, we will introduce the Unscented Kalman Filter (UKF) for nonlinear estimation. Beside this, the possibility of UKF in adaptive estimation is presented. It can be a new application of UKF if we can use this algorithm to estimate both the state and the parameter simultaneously instead of using a Kalman filter and a Recursive Least Square (RLS) identification of the parameter.

4.1.1 Optimal estimation-Bayesian point of view

From the probability theory, given the measurement *Y*, the hidden *X* can be estimated by one of the following methods: maximum likelihood estimation, maximum a posterior estimation, and minimum variance estimation [101].

The conditional probability of the hidden sequence X_k given the measurement Y_k can be obtained by Bayes' theorem [101]:

$$\Pr\left(X_k|Y_k\right) = \Pr\left(Y_k|X_k\right) \times \frac{\Pr\left(X_k\right)}{\Pr\left(Y_k\right)} \tag{4.1}$$

where $\Pr\left(X_k|Y_k\right)$ is the posterior, $\Pr\left(X_k\right)$ is the prior, $\Pr\left(Y_k|X_k\right)$ is the likelihood, and $\Pr\left(Y_k\right)$ is the evidence.

If the process dynamics is Markov, the sequential (recursive) the Bayesian estimator is established as follows with two stages in each computational cycle, the prediction and the correction.

Prediction:

This stage is to obtain the prior:

$$\Pr\left(x_k|Y_{k-1}\right) = \int \Pr\left(x_k|x_{k-1}\right) \times \Pr\left(x_{k-1}|Y_{k-1}\right) dx_{k-1} \tag{4.2}$$

Correction:

This stage is to obtain the posterior:

$$\Pr\left(x_k | Y_k\right) = \frac{\Pr\left(y_k | x_k\right)}{\Pr\left(y_k | Y_{k-1}\right)} \times \Pr\left(x_k | Y_{k-1}\right) \tag{4.3}$$

where $\Pr\left(y_k | x_k\right)$ is the likelihood, $\Pr\left(y_k | Y_{k-1}\right)$ is the evidence, and $Y_k = \{y_1, y_2, y_3, ..., y_k\}$.

The above algorithm is the general algorithm of the optimal state estimations. Some of them are presented in cases of study in the previous chapters.

4.1.2 Bayesian estimation of linear system

The linear stochastic system is express as follows:

$$\begin{cases} x_{k+1} = A_k x_k + B_k u_k + w_k \\ y_k = C_k x_k + v_k \end{cases} \tag{4.4}$$

where w_k and v_k are Gaussian noises, their covariance matrices are $R_{w,k}$ and $R_{v,k}$, respectively.

Using the above model, we can easily obtain the posterior in (4.3) using the following Gaussian distributions:

$$\Pr\left(y_k | x_k\right) \sim \left(C_k x_k, R_{v,k}\right) \tag{4.5}$$

$$\Pr\left(x_k | Y_{k-1}\right) \sim \left(\hat{x}_{k|k-1}, \tilde{P}_{k|k-1}\right) = \left(A_{k-1}\hat{x}_{k-1|k-1} + B_{k-1}u_{k-1}, A_{k-1}\tilde{P}_{k-1|k-1}A_{k-1}^T + R_{w,k-1}\right) \tag{4.6}$$

$$\Pr\left(y_k | Y_{k-1}\right) \sim \left(\hat{y}_{k|k-1}, R_{\varepsilon k}\right) = \left(C_k \hat{x}_{k|k-1}, C_k \tilde{P}_{k|k-1} C_k^T + R_{v,k}\right) \tag{4.7}$$

where $\hat{x}_{k|k-1}$ is the predicted state, $\hat{x}_{k|k}$ is the corrected state, $\tilde{P}_{k|k-1}$ is the prediction error covariance,

and $\tilde{P}_{k|k}$ is the correction error covariance.

Then, by maximizing the posterior, the update equations of the estimation gain and the correction state, and the correction error covariance are obtained as follows. They are the same as the update equations of the standard Kalman filter which is designed based on the minimum estimation error covariance. This is an interesting point of the Bayesian estimation theory.

$$L_k = \tilde{P}_{k|k-1} C_k^T \left(C_k \tilde{P}_{k|k-1} C_k^T + R_{v,k}\right)^{-1} \tag{4.8}$$

$$\hat{x}_{k|k} = \hat{x}_{k|k-1} + L_k \left(y_k - C_k \hat{x}_{k|k-1}\right) \tag{4.9}$$

$$\tilde{P}_{k|k} = \left(I - L_k C_k\right)\tilde{P}_{k|k-1} \tag{4.10}$$

4.1.3 Bayesian estimation of nonlinear system

How to obtain the posterior (new) distribution through the nonlinear transformation is a non-trivial question. The conventional solution is to approximate the nonlinear function of

First-order Taylor series Linearization

$$\bar{y} = g(\bar{x})$$
$$P_y = \nabla_g P_x (\nabla_g)^T$$

$$P_y = \nabla_g P_x (\nabla_g)^T$$

true covariance

true mean

$$\bar{y} = g(\bar{x})$$

Sigma-point transform

$$\mathcal{Y}_i = g(\mathcal{X}_i)$$
weighted sample mean
and covariance
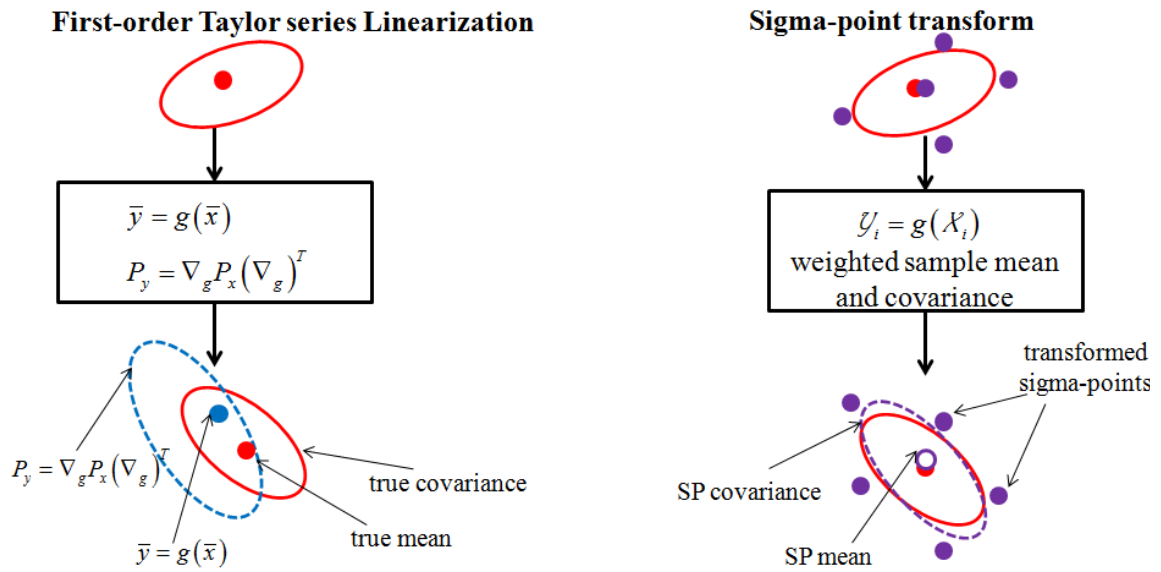
transformed
sigma-points

SP covariance

SP mean

Fig. 4.1 Comparison of two methods for nonlinear transformation.

transformation using Taylor series approximation. For instance, extended Kalman filter (EKF) is the algorithm that utilizes the first-order-approximation of the Taylor series [102]. This method requires the Jacobians calculation which suffers from the computational cost. Moreover, this algorithm might be unstable if the local linearity is violated. The estimation accuracy is degraded if the first order term does not dominate the higher order terms in the Taylor series.

In the last years of the 20th century, a new method named "sigma-points" is proposed by Julier, Uhlmann, and Durrant-Whyte [103] to deal with the nonlinear transformation. The key idea of this method seems to be heuristic: "*it is easier to approximate a probability distribution, than to approximate an arbitrary nonlinear function of transformation.*" The method can be described as follows: Firstly, a set of points with associated weights are generated such that they capture the original distribution. Then, these points are transferred directly using the nonlinear function without any Jacobians calculation. Finally, the transferred points with weights are used to calculate the mean and the covariance of the posterior distribution. One typical example of sigma-point family is the unscented Kalman filter (UKF) [104]. This method can capture not only the first-order-term but also higher-order-terms in the Taylor series. Thus, UKF can achieve the better estimation performance than the EKF. In this study, we will used the UKF as the tool to deal with the nonlinear estimation.

The comparison of the sigma-point transform with the first-order Taylor series linearization is shown in Fig. 4.1 (redrawn from the figure in [101]). In the following section, we will introduce the sigma-point transformation

4.2 Unscented Kalman filter

4.2.1 Sigma-point approach

To deal with the nonlinear transformation, the following idea is introduced by Julier *et al*: Select a set of sigma-point that they capture the specific properties of the underlying distribution. The problem can be expressed as:

GIVEN the sigma-points with associated weights $\Sigma = \{X_i, W_i, i=0,...,N_\sigma\}$ and the nonlinear transformation $a[X_i]$, FIND the statistics of the transformed samples $\mu_y = E\{y\}$, $R_{yy} = Cov\{y\}$.

The sigma-point method:

Step 1: Determine the number, weights, and locations of the sigma-points based on the unique of the characteristics of the prior distribution.

Step 2: Nonlinear transform each point to obtain the set of posterior sigma-point.

$$Y_i = a[X_i] \tag{4.11}$$

Step 3: Estimate the posterior mean and covariance:

$$\mu_y = \sum_{i=1}^{N_x} W_i Y_i, \qquad R_{yy} = \sum_{i=1}^{N_x} W_i (Y_i - \mu_y)(Y_i - \mu_y)^T \tag{4.12}$$

4.2.2 Sigma-point transformation for Gaussian distribution

In case of Gaussian distribution, the sigma-points are selected such that they capture the mean, the covariance, and the symmetric characteristics. Considering a N_x-dimensional random vector $\Sigma = \{X_i, W_i, i=0,...,N_\sigma\}$, the set of sigma-points can be chosen as follows:

$$X_0 = \mu, \qquad W_0 = \frac{\kappa}{N_x + \kappa} \tag{4.13}$$

$$X_i = \mu_x + \left(\sqrt{(N_x + \kappa) R_{xx}}\right)_i, \qquad W_i = \frac{1}{2(N_x + \kappa)} \tag{4.14}$$

$$X_{i+N_x} = \mu_x - \left(\sqrt{(N_x + \kappa) R_{xx}}\right)_i, \qquad W_{i+N_x} = \frac{1}{2(N_x + \kappa)} \tag{4.15}$$

where κ is the tuning parameter to minimize the mismatch between the 4-th order moments of sigma-points and the true distribution. $\left(\sqrt{(N_x + \kappa) R_{xx}}\right)_i$ is the *i*-th column of the matrix-square-root of $(N_x + \kappa) R_{xx}$. The matrix-square-root can be obtained by the *Cholesky decomposition* algorithm [105].

4.2.3 Unscented Kalman filter algorithm

Consider the following nonlinear stochastic system with additive noises:

$$\begin{cases} x_{k+1} = a[x_k] + b[u_k] + w_k \\ y_k = c[x_k] + v_k \end{cases} \tag{4.16}$$

where w_k and v_k are Gaussian noises, their covariance matrices are $R_{w,k}$ and $R_{v,k}$, respectively. a[ ], b[ ], and c[ ] are the nonlinear transfer functions.

The UKF algorithm is presented as follows:

<u>Initial conditions</u>

$$\hat{x}_{0|0}, \qquad \tilde{P}_{0|0} \tag{4.17}$$

<u>State: sigma-points and weights</u>

$$X_{0,k-1|k-1} = \hat{x}_{k-1|k-1}, \qquad W_0 = \frac{\kappa}{N_x + \kappa} \tag{4.18}$$

$$X_{i,k-1|k-1} = \hat{x}_{k-1|k-1} + \left(\sqrt{(N_x + \kappa)\tilde{P}_{k-1|k-1}}\right)_i, \qquad W_i = \frac{1}{2(N_x + \kappa)} \tag{4.19}$$

$$X_{i+N_x,k-1|k-1} = \hat{x}_{k-1|k-1} - \left(\sqrt{(N_x + \kappa)\tilde{P}_{k-1|k-1}}\right)_i, \qquad W_{i+N_x} = \frac{1}{2(N_x + \kappa)} \tag{4.20}$$

<u>State prediction</u>

$$X_{i,k|k-1} = a\left[X_{i,k-1|k-1}\right] + b\left[u_{k-1}\right] \tag{4.21}$$

$$\hat{x}_{k|k-1} = \sum_{i=0}^{2N_x} W_i X_{i,k|k-1} \tag{4.22}$$

<u>State error prediction</u>

$$\tilde{X}_{i,k|k-1} = X_{i,k|k-1} - \hat{x}_{k|k-1} \tag{4.23}$$

$$\tilde{P}_{k|k-1} = \sum_{i=0}^{2N_x} W_i \tilde{X}_{i,k|k-1} \tilde{X}_{i,k|k-1}^T + R_{w,k-1} \tag{4.24}$$

<u>Measurement: sigma-points and weights</u>

$$\hat{X}_{i,k|k-1} = \left\{X_{i,k|k-1}, X_{i,k|k-1} + \kappa\sqrt{R_{w,k-1}}, X_{i,k|k-1} - \kappa\sqrt{R_{w,k-1}}\right\} \tag{4.25}$$

<u>Measurement prediction</u>

$$Y_{i,k|k-1} = c\left[\hat{X}_{i,k|k-1}\right] \tag{4.26}$$

$$\hat{y}_{k|k-1} = \sum_{i=0}^{2N_x} W_i Y_{i,k|k-1} \tag{4.27}$$

<u>Residual prediction</u>

$$\varepsilon_{i,k|k-1} = Y_{i,k|k-1} - \hat{y}_{k|k-1} \tag{4.28}$$

$$R_{\varepsilon\varepsilon,k|k-1} = \sum_{i=0}^{2N_x} W_i \varepsilon_{i,k|k-1} \varepsilon_{i,k|k-1}^T + R_{v,k} \tag{4.29}$$

<u>Estimation gain</u>

$$R_{\tilde{X}\varepsilon,k|k-1} = \sum_{i=0}^{2N_x} W_i \tilde{X}_{i,k|k-1} \varepsilon_{i,k|k-1}^T \tag{4.30}$$

$$L_k = R_{\tilde{X}\varepsilon,k|k-1}\left(R_{\varepsilon\varepsilon,k|k-1}\right)^{-1} \qquad (4.31)$$

State correction

$$e_k = y_k - \hat{y}_{k|k-1} \qquad (4.32)$$

$$\hat{x}_{k|k} = \hat{x}_{k|k-1} + L_k e_k \qquad (4.33)$$

$$\tilde{P}_{k|k} = \tilde{P}_{k|k-1} - L_k R_{\varepsilon\varepsilon,k|k-1} L_k^T \qquad (4.34)$$

4.3 UKF for simultaneous estimation of parameter and state

As discussed in Chapter 1, the adaptive estimation can be designed using the estimator (such as Kalman filter) along with the parameter identification (such as the RLS identification). As shown in Fig. 4.2 (a), the estimated state vector $\hat{x}$ is fed to the Identification and the parameter vector $\hat{c}$ is fed to the Estimator. This estimation configuration is complex to design. Moreover, it is questionable for the convergence to the true values of this estimation configuration. For instance, if the uncertainty is large and the initial values of the parameter vector is considerably inaccurate. In this case, the estimated state is inaccurate, and again, it gives negative influence to the Identification.

Considering the following stochastic system:

$$\begin{cases} x_{k+1} = g\left[x_k, u_k, c_k\right] + w_k \\ y_k = h\left[x_k, u_k, c_k\right] + v_k \end{cases} \qquad (4.35)$$

where x_k is the state vector, u_k is the input vector, and c_k is the parameter vector, w_k and v_k are Gaussian noises.

We may introduce the dynamics of the parameter vector, for instance, as a random walk process:

$$c_{k+1} = c_k + w_{c,k} \qquad (4.36)$$

By this way, the following augmented system can be obtained:

$$\begin{cases} X_{k+1} = G\left[X_k, U_k\right] + W_k \\ Y_k = H\left[X_k, U_k\right] + V_k \end{cases} \qquad (4.37)$$

where

$$X_k = \begin{bmatrix} x_k \\ c_k \end{bmatrix}, \ U_k = u_k, \ Y_k = y_k, \ W_k = \begin{bmatrix} w_k \\ v_k \end{bmatrix}, \ V_k = v_k \qquad (4.38)$$

The system (4.35) can be a linear or nonlinear system. However, the augmented system (4.37) is generally a nonlinear system. Therefore, it is possible to estimate both the state and the parameter simultaneously using the simpler configuration in Fig. 4.2 (b).
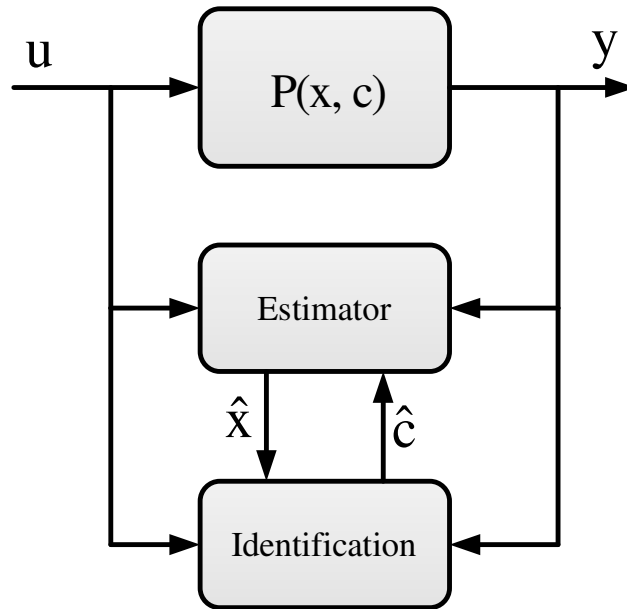
(a) State estimator + parameter identification.
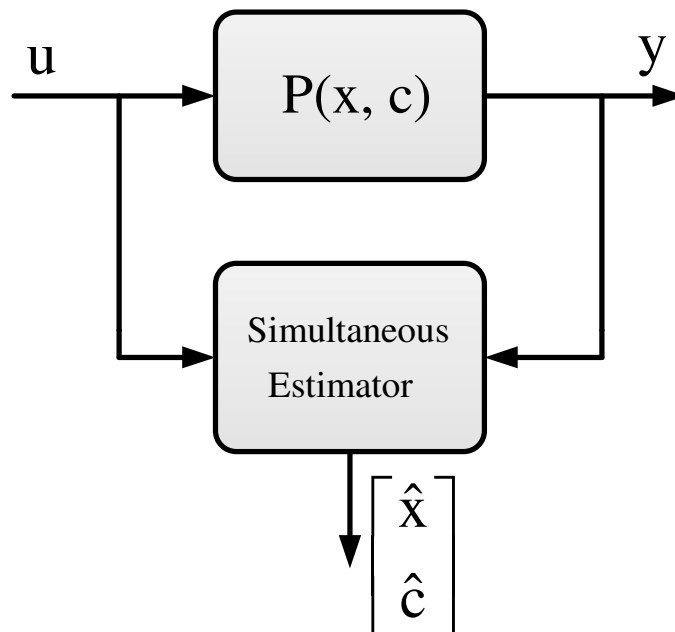
(b) Estimation of augmented system using UKF.

Fig. 4.2 Two configurations for state and parameter estimation.

4.4 Discussion

In this chapter, we introduce the sigma-point-transformation and the unscented Kalman filter which is an effective tool for estimation design of the nonlinear system. However, our goal is not studying the nonlinear estimation. We aim to utilize the nonlinear estimation tool to develop a new configuration of adaptive estimation. Together with the state, the parameter can be considered as the extension state and an augmented state space model can be established. Because the augmented model is usually nonlinear, the unscented Kalman filter can be applied to estimate both the state and the parameter simultaneously. This is an alternative configuration besides the adaptive estimator including the filter/observer and the RLS identification.

In Chapter 7, the effectiveness of the new configuration will be verified through a case of study: simultaneous estimation of vehicle's sideslip angle and cornering stiffness using tire lateral force sensors. Through this case of study, the two configurations in Fig. 4.2 will be compared with each other.

Part B

Motion Control Application

Chapter 5:

Motion Control of Electric Vehicle Using GPS

"The EV is the most exciting object to apply advanced motion control technique."

Prof. Yoichi Hori

5.1 Why electric vehicle?

Electric vehicles (EVs) have been interested by both the industry and the academic circles because of their advantages for environmental protection and energy conservation. Various types of EVs have been produced by automotive companies all over the world, such as the Nissan Leaf, the Fiat 500e, the Honda Fit EV, etc. Thanks to the development of wireless power transfer, super-capacitor and energy management, EVs will soon become popular to replace the internal combustion engine vehicles (ICEVs). Equipped with the electric motors, from the view point of motion control, EVs has number of remarkable advances in comparison with the ICEVs [57]:

1. The torque response of EVs is very quick, 10-100 times faster than that of ICEVs. Thus, it is possible use the motor torque as the control input to design the two degree of freedom control of EVs. For instance, high performance adhesion control of EVs was realized, such as the anti skid control [57].

2. The motor torque can be obtained easily from the motor current. Consequently, road condition estimation and driving force observer can be attained [58].

3. The electric motors are compact and inexpensive. Therefore, they can be installed at each wheel. This means that each wheel's torque can be controlled independently to generate yaw-moment – a control input of the vehicle stability control system [59].

In conclusion, EVs is a novel motion control system. In near future, EVs should be the means of transportation of human society. Needless to say, research on motion control of EVs play the non-trivial role in both industrial circle and academic circle.

5.2 Why GPS for EV motion control?

Considering the control purpose and the desired state feedback, motion controls of electric vehicle are summarized in Table 5. 1. This summarization shows that many motion variables are desirable to be estimated, such as sideslip angle, roll angle, pitch angle, yaw angle, longitudinal velocity. These variables can be estimated using inertial sensors and encoders. For instance, in [60], the gyroscopes and accelerometers are used to estimate the roll angle and the pitch angle. As mentioned in Chapter 1, the inertial sensors suffer from the strong noises, bias, scale error… Therefore,
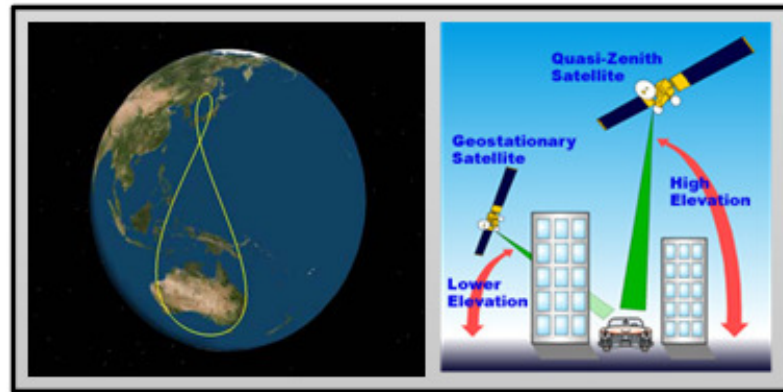
(a) QZSS (Source: JAXA)
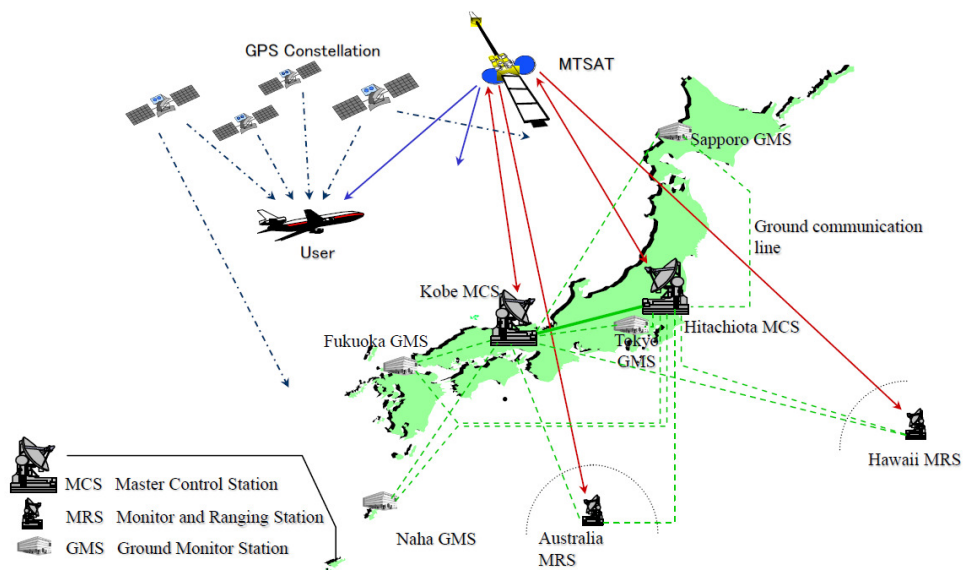
(b) MTSAT (Source: Ministry of Land, Infrastructure and Transportation, Japan).

Fig. 5.1 Japan's own GPS system.

sensor fusion in which the inertia sensors are fused with other nonconventional sensors has been researched for years. The nonconventional sensors can be a vision system [61], magnetometer [45], GPS [22], tyre force sensor [62], etc. Among them, GPS became a strong candidate due to the following reasons:

1) GPS provides not only the position but also the velocity and the course angle. In contrast, another sensor like the magnetometer or the vision system can only provide the yaw angle (heading angle) of the vehicle. The measurements from GPS can be utilized for many motion control purposes, such as lateral stability control, traction control, velocity control, autonomous control.

2) GPS provides the long-term-stable and accurate measurements. Thanks to the development of GPS technology, our GPS receiver can receive not only the signal from the system produced by United States but also other correction signals. Nowadays, many space based augmented systems

have been launched, such as European geostationary overlay system (EGNOS), India' GPS aided GEO augmented navigation system (GAGAN), and Chinese's satellite navigation augmentation system (SNAS). In Japan, national projects have been conducted in order to establish Japan's own GPS. The Quasi-zenith satellite system (QZSS) has been designed by Japan Space Association (JAXA) to provide high elevation satellites over Japan to overcome problems with navigation in urban area with tall buildings, as shown in Fig 5.1(a). The MTSAT satellite-based augmentation system (MSAS) has been developed by Japan Civil Aviation Bureau (JCAB). The MSAS is described in Fig. 5.1(b) with two master control stations (MCS) located in Kobe and Hitachiota. As the Japan's Strategic Headquarters for Space Policy, their QZSS can improve the positioning accuracy considerably, to a sub-meter or several-centimeter level [63]. If real-time-kinematic (RTK) technique is applied in which the correction signal comes from local station, the GPS positioning can attain the centimeter level of accuracy.

From the above discussions, we have been interested in using GPS to design the state estimation for electric vehicle motion control.

Table 5.1 Controlled states in EV motion controls

Control purpose	Methods to obtain state feedback	
	Measurement	*Estimation*
Traction control [64]	Wheel rotational speed	Vehicle longitudinal velocity
Lateral stability [65]	Yaw-rate	Sideslip angle
Roll stability [66]		Roll angle
Pitch stability [67]		Pitch angle
Driving force control [68]		Wheel's driving force
Range extension control [69]	Wheel rotational speed & Yaw-rate	Vehicle longitudinal velocity & Sideslip angle
Yaw angle control [70]		Yaw angle

5.3 Vehicle dynamics

Dynamics of vehicle includes many issues. In this thesis, we just present the basics of lateral dynamics which is the background of the contribution of this thesis.

5.3.1 Characteristics of the tire lateral force

The tire is the main component of the vehicle that interacts with the surface of the road. Therefore, it is essential to study the tire lateral force characteristics for lateral motion control of the vehicle. In this section, the relation between the tire lateral force and the tire slip angle is examined. As shown in Fig. 5.2, the lateral force will exert on the tire as the tire slip angle appears. As a result, the tire will be deformed. When the tire slip angle is small, the lateral force is proportional to the tire slip angle. The cornering stiffness can be defined to express this linear relationship:

$$F_y = C\alpha \tag{5.1}$$

where F_y is the tire lateral force, α is the tire slip angle, and C is the tire cornering stiffness.

The tire lateral force increases when the tire slip angle becomes larger. At a certain large tire slip angle, the tire lateral force is saturated because of the friction limit [71]. As shown in Fig. 5.3, the vector addition of the lateral and longitudinal tire force is upper-bounded by the vertical tire force multiplied by the road friction coefficient. The characteristics of the lateral tire force can be generally explained in Fig. 5.4. If the tire slip angle is small, the tire force is placed in the linear region with a certain cornering stiffness. On the other hand, if the tire slip angle is large, the tire force will be placed in the non-linear region. The maximum value of the tire lateral force decreases when the friction coefficient of the road becomes smaller.

A number of works have been conducted to formulate the tire lateral force characteristics. For instance, in [71], an empirical model is proposed as follows:

$$F_y = \begin{cases} C\alpha - \dfrac{(C\alpha)^2}{4\mu F_z} & when \ \alpha < \dfrac{F_z}{C} \\ \mu F_z & when \ \alpha \geq \dfrac{F_z}{C} \end{cases} \tag{5.2}$$

Where F_z is the vertical force of the tire, and μ is the road friction coefficient. In this thesis, the empirical model expressed in (5.2) is utilized in order to construct the simulation model using MATLAB/SIMULINK.

In [72], another model is constructed for modeling the tire force characteristics using the "magic formula":

$$F_y = D \sin\left[C \arctan\left\{ B\alpha - E\left(B\alpha - \arctan(B\alpha) \right) \right\} \right] \tag{5.3}$$

where B is the stiffness factor, C is the shape factor, D is the peak factor, and E is the curvature factor. By adjusting the stiffness factors, the expression of the tire lateral force can be modified flexibly to match with the experimental results.

5.3.2 Vehicle handling models

In this study, the electric vehicle with the active front steering is used for studying. Therefore, a front steer vehicle model is constructed as shown in Fig. 5.5. In Fig. 5.5 and the following equations, β is the sideslip angle; γ is the yaw rate; a_x and a_y are the longitudinal and lateral acceleration; v_x is the longitudinal velocity; v_y is the lateral velocity; V is the velocity vector; δ_f is the front steering angle; l_f, l_r, d_f, and d_r are the dimensions of the vehicle; m is the mass of vehicle; I_z is the yaw moment of inertia; and N_z is the yaw moment which is the result of the different driving torques at the left and the right sides in-wheel motors.
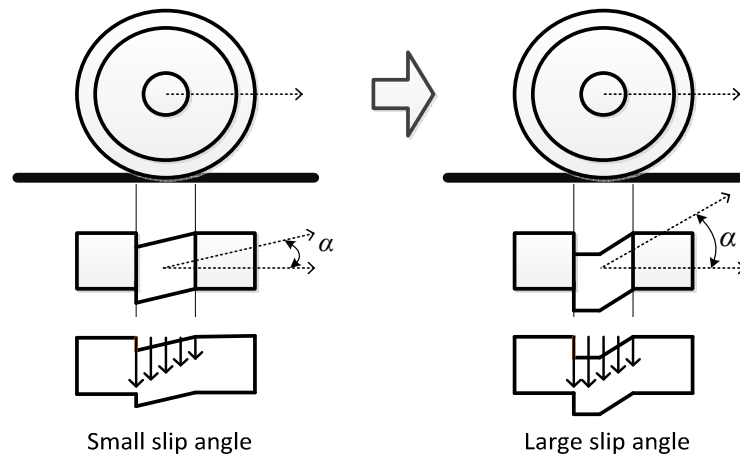
Fig. 5.2 The deformation of the tire at different slip angles.
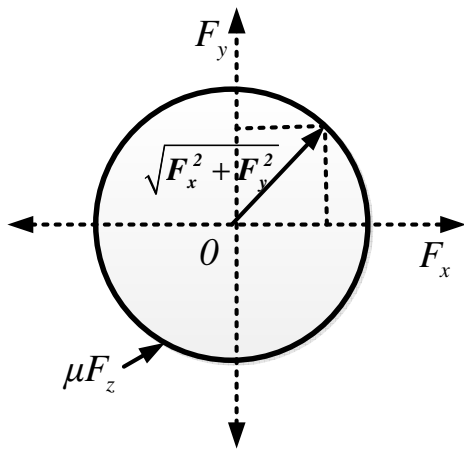

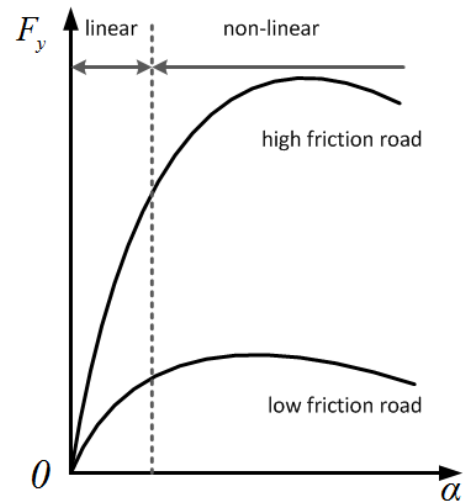Fig. 5.3 Friction limit circle.

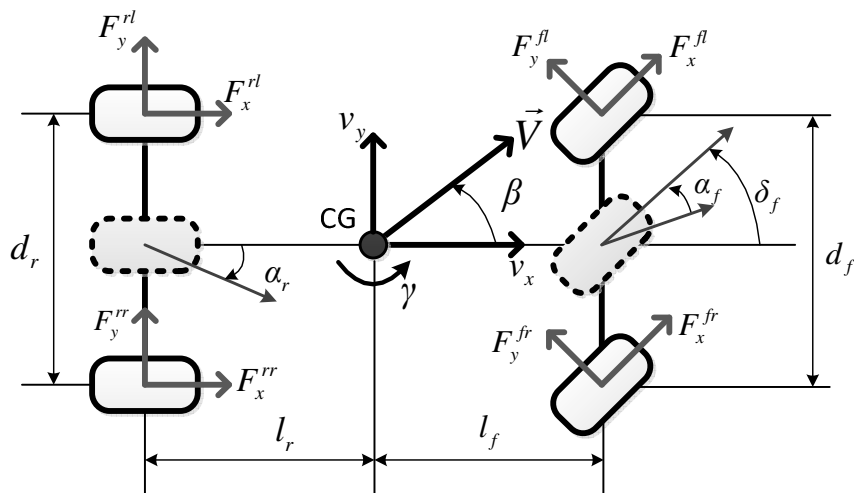Fig. 5.4 Characteristics of the tire lateral force.

Fig. 5.5 Planar model of the vehicle with front steering.

Using the vehicle model in Fig. 5.5 and assume that the tire force is in linear region, the calculation of the tire lateral forces can be expressed as:

$$F_y^{fl} = -C_f \left(\frac{v_x\beta + l_f\gamma}{v_x - \frac{d_f}{2}\gamma} - \delta_f \right) \tag{5.4}$$

$$F_y^{fr} = -C_f \left(\frac{v_x\beta + l_f\gamma}{v_x + \frac{d_f}{2}\gamma} - \delta_f \right) \tag{5.5}$$

$$F_y^{rl} = -C_r \left(\frac{v_x\beta - l_r\gamma}{v_x - \frac{d_r}{2}\gamma} \right) \tag{5.6}$$

$$F_y^{rr} = -C_r \left(\frac{v_x\beta - l_r\gamma}{v_x + \frac{d_r}{2}\gamma} \right) \tag{5.7}$$

5.3.3 Linear model of vehicle

For the sake of simplicity, the linear bicycle model in Fig. 5.6 is widely used in motion control of the vehicle. This model is constructed under the following assumptions: 1) The tire slip angle is small such that the tire force is in the linear region. 2) The vehicle is symmetric about the fore-and-aft center line. 3) The load transfer is neglected. 4) The vehicle velocity is almost constant.

Using the linear bicycle model in Fig. 5.6, the front and rear tire lateral forces can be expressed as follows:

$$F_{yf} = -2C_f\alpha_f \tag{5.8}$$
$$F_{yr} = -2C_r\alpha_r \tag{5.9}$$

The front and rear tire slip angle can be expressed as:

$$\alpha_f = \beta + \frac{l_f}{v_x}\gamma - \delta_f \tag{5.10}$$

$$\alpha_r = \beta - \frac{l_r}{v_x}\gamma \tag{5.11}$$

The lateral force equation and the yaw moment equation can be rewritten as:

$$F_{yf} + F_{yr} = mv_x\left(\dot\beta + \gamma\right) \tag{5.12}$$

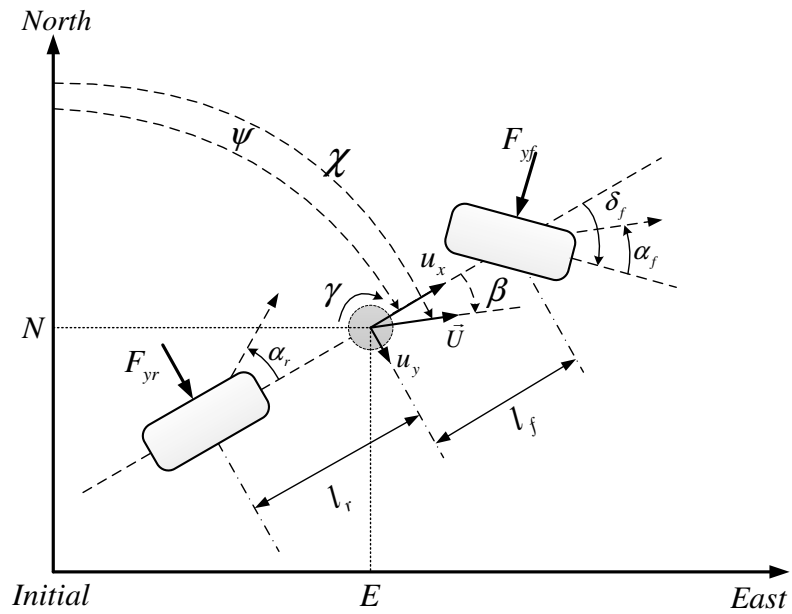$$F_{yf}l_f - F_{yr}l_r + N_z = I_z\dot\gamma \tag{5.13}$$

Fig. 5.6 Bicycle model of the vehicle on the North-East coordinates.

From (5.8) ~ (5.13), the state space model of the lateral dynamics of the vehicle is established as follows:

$$\dot{x} = Ax + Bu \tag{5.14}$$

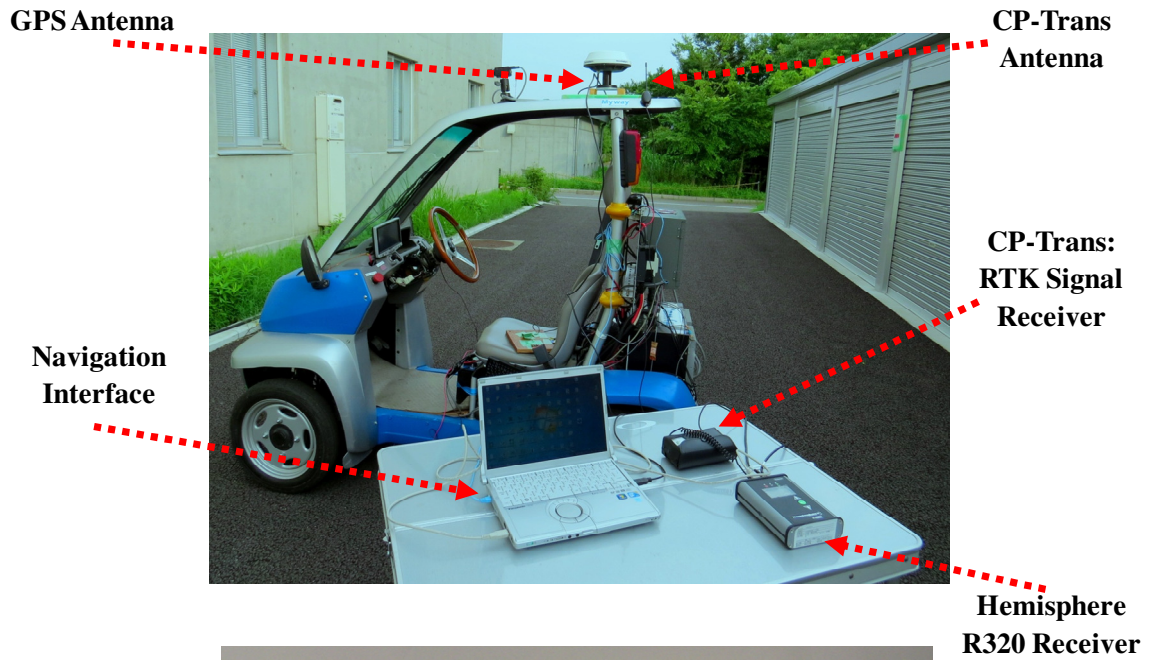$$x = \begin{bmatrix} \beta & \gamma \end{bmatrix}^T \tag{5.15}$$

$$u = \begin{bmatrix} \delta_f & N_z \end{bmatrix}^T \tag{5.16}$$

$$A = \begin{bmatrix} a_{11} & b_{11} \\ a_{22} & b_{22} \end{bmatrix} = \begin{bmatrix} \dfrac{-2(C_f + C_r)}{mv_x} & -1 - \dfrac{2(C_f l_f - C_r l_r)}{mv_x^2} \\ \dfrac{-2(C_f l_f - C_r l_r)}{I_z} & \dfrac{-2(C_f l_f^2 + C_r l_r^2)}{I_z v_x} \end{bmatrix} \tag{5.17}$$

$$B = \begin{bmatrix} b_{11} & b_{12} \\ b_{21} & b_{22} \end{bmatrix} = \begin{bmatrix} \dfrac{2C_f}{mv_x} & 0 \\ \dfrac{2C_f l_f}{I_z} & \dfrac{1}{I_z} \end{bmatrix} \tag{5.18}$$

Fig. 5.6 also shows the vehicle on the North-East coordinates. The course angle χ is the angle between the vehicle's velocity vector and the North. By using a single antenna GPS receiver, the course angle of the vehicle is measured. It equals to the yaw angle ψ plus the sideslip angle β.

$$\chi = \psi + \beta \tag{5.19}$$

GPS Antenna

CP-Trans Antenna

CP-Trans: RTK Signal Receiver

Navigation Interface

Hemisphere R320 Receiver

RTK GPS Receiver and Antenna

Optical sensor for sideslip angle measurement

Fig. 5.7 Experimental system.

Fig. 5.8 GPS interface software and experimental data.

Table 5.2 Specification of the experimental EV

Total mass	400 kg
Wheel base	1.2 m
Track-width of rear wheel	0.82 m
Height of CG	0.4 m
Wheel radius	0.26 m
Wheel spin inertia	1.26 kgm^2
Yaw moment of inertia	136 kgm^2
Energy store (super-capacitor)	210V, 29F, 173 Wh
Main controller	PC104, Linux OS
In-wheel motor type	PMSM
Max. motor power	2 kW
Max. motor torque	100 Nm
Max. vehicle velocity	50 km/h

5.4 Experimental electric vehicle

The micro in-wheel motored EV named "Super-capacitor COMS" developed by our research group is used in this study (Fig. 5.7). Its specifications are shown in Table 5.2. Two in-wheel motors are placed in the rear-left and rear-right wheels. Thus, the driving torque of each wheel can be controlled independently. The active-front-steering is installed so both manual driving and autonomous driving are available. The EV is equipped with gyroscopes and accelerometers to measure the yaw-rate, the longitudinal acceleration and the lateral acceleration. Encoders are used to obtain the steering angle or wheel rotation speed. In addition, a non-contact optical sensor produced by Corrsys-Datron is used for accurate acquisition of the sideslip angle, longitudinal velocity, and lateral velocity. In this paper, it is used to evaluate the proposed estimation algorithm. Although it is placed in the front of the EV, the sideslip angle at the center of gravity can be derived thanks to an understanding of the vehicle geometry. The RTK-GPS receiver produced by Hemisphere is used in this study. It can provide not only the vehicle position but also its velocity and course angle. In the RTK operation mode, the positioning of one-centimeter-accuracy level is achieved. The GPS interface software is developed to manage, decode, and displace data from the GPS receiver in real time, as shown in Fig. 5. 8. The RT-Linux operating system computer is used to process the algorithm in real-time and to collect the experimental data.
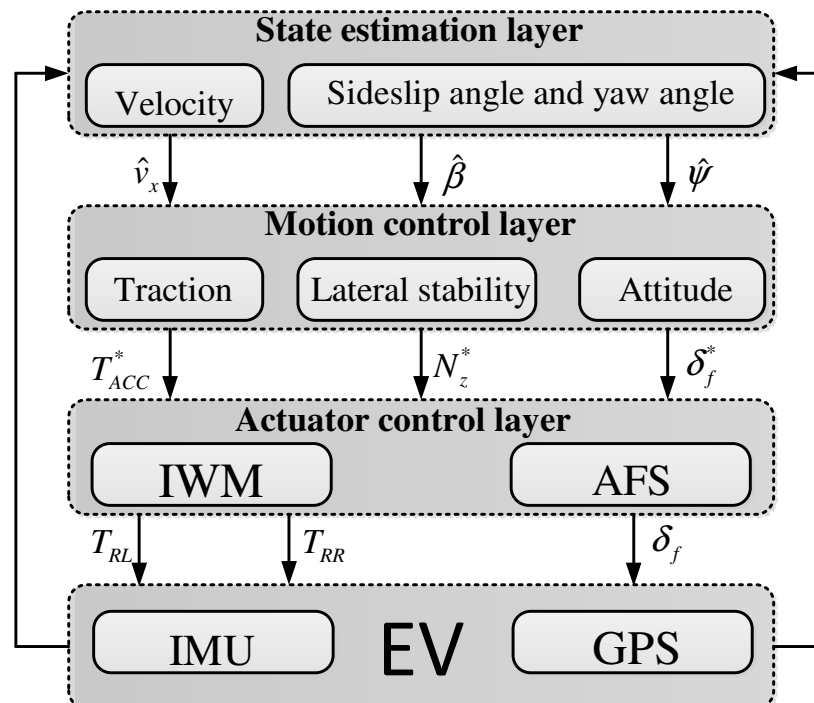

Fig. 5.9 Electric vehicle motion control system using GPS.

5.5 Introduction to the electric vehicle control system using GPS

The electric vehicle motion control system is shown in Fig. 5.9 including three layers. Using the measurements from GPS and IMU, the state estimation layer outputs the estimated values of longitudinal velocity, sideslip angle, and yaw angle to the motion control layer. In the motion control layer, the traction control is established based on the wheel-slip-ratio calculated through estimated velocity. Lateral stability control is designed thanks to the estimated sideslip angle. Attitude control is constructed using the estimated yaw angle. The motion control layer outputs the acceleration command, the yaw moment command, and the front steering command to the actuator control layer. The actuator control layer distributes the torque to the rear left and rear right in-wheel motors and controls the front active steering motor.

5.6 Robust estimation of sideslip angle using GPS
5.6.1 Literature review

Using an accelerometer and a gyroscope, sideslip angle estimation methods can be divided into three groups: kinematic model based estimation [18], [73], nonlinear dynamic model based estimation [74], [75], and linear dynamic model based estimation [19], [76]. The kinematic model based estimation is very simple to be implemented. Moreover, it does not rely on tire force characteristics of the vehicle. However, it uses accelerometers and gyroscopes which are always interfered by strong noise, offset, and scale errors. Therefore, this method does not satisfy stable and accurate estimation in the long-term. Although non-linear estimation has been developed theoretically, it is too complicated to be implemented in real-time. Therefore, linear model based estimation seems to be a suitable choice when considering both the robustness issue and the computation issue. However, due to the variation of road conditions, the linear model of the vehicle contains uncertain parameters such as the tire cornering stiffness. A linear estimator with constant tire cornering stiffness is certainly not robust enough. In [29], adaptive estimation of sideslip angle, which is the combination of a linear observer and online cornering stiffness identification, is introduced. This method increases the computational burden of the control system because it requires a tire force estimator in addition to the parameter identification. If the road conditions suddenly change (for instance, from high friction to low friction), accurate sideslip angle estimation is not achieved until the convergence of identified cornering stiffness.

Recently, sideslip angle estimation using nonconventional sensors has been studied. An on-board vision system using a camera and image processing can obtain the heading angle of the vehicle for sideslip angle estimation [77]. However, visibility is not always available, due to bad weather or when road markers are covered with leaves, snow, dirt, or water. The huge computation time of image processing results in measurement delay which is a serious problem in estimation design. On the other hand, based on the differences between the left and right tire lateral force measurements, the sideslip angle can be identified without cornering stiffness [78]. This method seems to be mathematically

beautiful from its formulation. However, the possibility of this method for practical application is still questionable. First, the cost of tire force sensors are high and it is not easy to install this sensor into the rim of the wheel. Second, this sensor would suffer from strong noise and signal delay. Third, the influence of load transfer is not considered in this method. Last but not least, the authors use a linear identification algorithm which is only suitable for slow time-varying parameter estimation. In fact, the sideslip angle varies quickly and frequently, especially during sharp cornering or slalom driving.

Since the middle of the last decade, global positioning system (GPS) became a candidate for sideslip angle estimation. Thanks to the development of GPS technology, satellite systems, and GPS signal correction services, GPS can provide accurate measurement of vehicle motion in the long term [79]. By using a double-antenna GPS receiver, sideslip angle can be calculated directly considering the phase shift of carrier waves arriving at two different antennae at known locations on the vehicle [80]. However, this method is too expensive to be used in production vehicles. Moreover, the estimation period of this method is limited by the poor update rate of GPS receivers. In [81], estimation is design based on a kinematic model using the fusion of the inertial measurement unit, GPS, and magnetometer. This method is influenced by the variation of Earth's magnetic field and other aforementioned problems of the kinematic method. In [82], Bevly utilized a single-antenna GPS along with a yaw-rate sensor. This method relies on the integration of yaw-rate measurement to calculate the yaw angle. Then, the sideslip angle is calculated by subtracting GPS's course angle with the yaw angle. This method is very simple but not effectively robust due to many problems, such as the noises and scale error of yaw-rate sensor and the out-of-plan vehicle motion. In [24], Anderson *et al* made an advance of the method in [82] by using the linear bicycle model for estimation design. However, Anderson used the conventional Kalman filter without any consideration of the model uncertainties or unknown disturbances. Between two consecutive updates of the GPS measurement, it only relies on the yaw-rate measurement to estimate the sideslip angle. As a result, the estimation is not robust enough and could be degraded easily during these intervals.

From the aforementioned discussion, considering both the cost and robustness issues, the dynamic model based estimation using a single antenna GPS and a yaw-rate sensor could be a good selection if we can design a robust estimation algorithm. The clear advantage of this sensor fusion is that the measurement equation does not contain cornering stiffness as any method using lateral accelerometer does. Moreover, we can combine the advantages of each sensor: accuracy and stability in long-term GPS and high-update-rate of yaw-rate sensor.

5.6.2 Some previous methods

A. Estimation using yaw-rate sensor and accelerometer

In [76], by using the linear bicycle model, Aoki *et al* introduce the following observer in the continuous-time domain:

$$\dot{\hat{x}} = A\hat{x} + Bu + K\left(y - C\hat{x} - Du\right) \tag{5.20}$$

$$K = \begin{bmatrix} k_{11} & k_{12} \\ k_{21} & k_{22} \end{bmatrix} = \begin{bmatrix} \dfrac{\lambda_1 \lambda_2}{C_f} \dfrac{\left(l_f - l_r\right)I_z}{2\left(l_f^2 + l_r^2\right) + 4l_f l_r} - 1 & \dfrac{1}{u_x} \\ -\lambda_1 - \lambda_2 & \dfrac{m\left(l_f^2 + l_r^2\right)}{\left(l_f - l_r\right)I_z} \end{bmatrix} \tag{5.21}$$

Aoki *et al* claim that the observer gain K in (5.21) is the best for robust conditions. However, their proposed observer gain does not satisfy any popular criterion of robust estimation, such as:

Design K that $E\left[\left(x_k - \hat{x}_k\right)\left(x_k - \hat{x}_k\right)^T\right] \to \min$ \hfill (5.22)

For detailed explanation, k_{12} is obtained by considering the estimation error of sideslip angle:

$$\dot{\hat{\beta}} - \dot{\beta} = \left(\hat{\beta} - \beta\right)\left(a_{11} - k_{12}v_x\right) - \left(1 - k_{12}v_x\right)\left(a_{11}' - a_{11}\right)\beta + \left(\hat{\gamma} - \gamma\right)\left[a_{12} - k_{12}v_x\left(a_{12} + 1\right) - k_{11}\right]$$
$$- \left(1 - k_{12}v_x\right)\left(a_{12}' - a_{12}\right)\gamma + \left(1 - k_{12}v_x\right)\left(b_{11} - b_{11}'\right)\delta_f \tag{5.23}$$

where a_{11}', a_{12}', and b_{11}' are the real values of the vehicle dynamics model; a_{11}, a_{12}, and b_{11} are the nominal values of the estimation model.

According to Aoki *et al*, under the assumption that $\hat{\gamma} \approx \gamma$ the "best" condition for robust estimation is that $1 - k_{12}v_x = 0$, in other words $k_{12} = \dfrac{1}{u_x}$.

B. Estimation using yaw-rate sensor and GPS

Following the idea in [24] and [82], the course angle from GPS can be a measurement and the yaw angle can be another state along with the sideslip angle. The following model is established:

$$\dot{x} = Ax + Bu \tag{5.24}$$

$$x = \begin{bmatrix} \beta & \gamma & \psi \end{bmatrix}^T, \quad u = \begin{bmatrix} \delta_f & N_z \end{bmatrix}^T \tag{5.25}$$

$$A = \begin{bmatrix} a_{11} & a_{12} & 0 \\ a_{21} & a_{22} & 0 \\ 0 & 1 & 0 \end{bmatrix}, \quad B = \begin{bmatrix} b_{11} & b_{12} \\ b_{21} & b_{22} \\ 0 & 0 \end{bmatrix} \tag{5.26}$$

The above continuous time model can be transformed into the discrete time model with fundamental sampling time T_c using the following transformation:

$$A_k = e^{AT_c}, \quad B_k = \int_0^{T_c} e^{A\tau} d\tau B \tag{5.27}$$

To provide the state feedback control, T_c is set to be the same as the period of the control input u. (for instance, $T_c = 1$ millisecond). In our system, the sampling time of GPS course angle is rT_c where r is the dual-rate ratio which is an integer number. For the sake of simplicity, we assume that the sampling time of the yaw-rate sensor is also T_c. A stochastic discrete-time system can be established as follows:

$$x_{k+1} = A_k x_k + B_k u_k + w_k \tag{5.28}$$

$$y_k = C_k x_k + \delta_k v_k \tag{5.29}$$

$$C_k = \begin{cases} \begin{bmatrix} 0 & 1 & 0 \\ 1 & 0 & 1 \end{bmatrix} & \text{if } k = jr \\ \begin{bmatrix} 0 & 1 & 0 \\ 0 & 0 & 0 \end{bmatrix} & \text{if } k \neq jr \end{cases} , \quad \delta_k = \begin{cases} \begin{bmatrix} 1 & 0 \\ 0 & 1 \end{bmatrix} & \text{if } k = jr \\ \begin{bmatrix} 1 & 0 \\ 0 & 0 \end{bmatrix} & \text{if } k \neq jr \end{cases} \tag{5.30}$$

where w_k and v_k are Gaussian noises with zero means, the measurement vector is $y_k = \begin{bmatrix} \gamma_k & \chi_k \end{bmatrix}^T$. The second row of the measurement matrix is set to zero during the periods that GPS measurement is unavailable.

Then, a conventional estimation method, such as the standard Kalman filter [12] can be applied to design the estimation:

$$\hat{x}_{k+1} = A_k \hat{x}_k + B_k u_k + L_k \left(y_k - C_k \hat{x}_k \right) \tag{5.31}$$

C. Estimation using yaw-rate sensor and GPS based on innovation holding scheme

According to the above method, during the period that GPS measurement is unavailable, the sideslip angle is corrected only by the innovation from yaw-rate measurement. Notice that the yaw-rate measurement suffers from the scale error, noises, sensor bias. Moreover, the modeling may have uncertainty, the cornering stiffness is a time-varying parameter, and the external disturbance like wind force is unknown. Therefore, during the GPS-unavailable-periods, the estimation accuracy is degraded. To improve the estimation accuracy, it is possible to utilize the innovation holding method which is introduced in Chapter 1. This method is originally proposed by Hara *et al* [37].

Define $y_{1,k}$ as the yaw-rate measurement and $y_{2,k}$ as the course angle measurement. The measurement equations (without noises) can be expressed as:

$$y_{1,k} = C_{1,k} x_k \tag{5.32}$$

$$C_{1,k} = \begin{bmatrix} 0 & 1 & 0 \end{bmatrix} \tag{5.33}$$

$$y_{2,k} = C_{2,k} x_k \tag{5.34}$$

$$C_{2,k} = \begin{cases} \begin{bmatrix} 1 & 0 & 1 \end{bmatrix} & \text{if } k = jr \\ \begin{bmatrix} 0 & 0 & 0 \end{bmatrix} & \text{if } k = jr \end{cases} \quad C_{2,k} = \begin{cases} \begin{bmatrix} 1 & 0 & 1 \end{bmatrix} & \text{if } k = jr \\ \begin{bmatrix} 0 & 0 & 0 \end{bmatrix} & \text{if } k = jr \end{cases} \tag{5.35}$$

Assume that $t = jr$, the GPS measurement is updated. The estimation algorithm can be expressed as follows:

$$\hat{x}_{t+i+1} = \begin{cases} A_t \hat{x}_t + B_t u_t + L_{1,t} \left(y_{1,t} - C_{1,t} \hat{x}_t \right) + L_{2,t} \left(y_{2,t} - C_{2,t} \hat{x}_t \right) & \text{for } i = 0 \\ A_{t+i} \hat{x}_{k+i} + B_{t+i} u_{t+i} + L_{1,t+i} \left(y_{1,t+i} - C_{1,t+i} \hat{x}_{t+i} \right) + L_{2,t+i} \left(y_{2,t} - C_{2,t} \hat{x}_t \right) & \text{for } i \in [1, \ r-1] \end{cases} \tag{5.36}$$

The innovation of the GPS measurement $\left(y_{2,t} - C_{2,t} \hat{x}_t \right)$ is stored for contributing the correction during the GPS-unavailable-periods. The observer gains $L_{1,t+i}$ and $L_{2,t+i}$ can be obtained through pole-placement.

5.6.3 Estimation using yaw-rate sensor and GPS based on disturbance accommodation

A. Disturbance accommodation

All three above sideslip angle estimation methods fail to deal with model uncertainties and external disturbances. In this sub-section, we will propose a more robust estimation algorithm. Firstly, let's go back to the decade of 1970s when Johnson introduced the concept of "disturbance accommodation" [83]. His idea is that we might introduce to the linear system a disturbance term along with the disturbance's dynamics to establish an extended state linear system. By this way, the robust of the linear regulator can be improved by the estimation of both the state and the disturbance term. The disturbance accommodation control is applied to motion control of a helicopter in [84].

Utilizing this idea, we introduce the disturbance term into the stochastic dynamics in (5.28):

$$x_{k+1} = A_k x_k + B_k u_k + \Gamma_k x_{d,k} + w_k \tag{5.37}$$

where

$$x_{d,k} = \begin{bmatrix} x_{d1,k} & x_{d2,k} \end{bmatrix}^T \tag{5.38}$$

$$\Gamma_k = \begin{bmatrix} 1 & 0 \\ 0 & 1 \\ 0 & 0 \end{bmatrix} \tag{5.39}$$

Assume that the disturbance term is a random-walk process:

$$x_{d,k+1} = x_{d,k} + w_{d,k} \tag{5.40}$$

where $w_{d,k}$ is the Gaussian noise associated with the random-walk.

The extended system is established as:

$$\bar{X}_{k+1} = \bar{A}_k \bar{X}_k + \bar{B}_k \bar{U}_k + \bar{W}_k \tag{5.41}$$

$$\bar{Y}_k = \bar{C}_k \bar{X}_k + \bar{\delta}_k \bar{V}_k \tag{5.42}$$

$$\bar{X}_k = \begin{bmatrix} x_k \\ x_{d,k} \end{bmatrix}, \ \bar{U}_k = u_k, \ \bar{Y}_k = y_k \tag{5.43}$$

$$\bar{A}_k = \begin{bmatrix} A_k & \Gamma_k \\ [0]_{2\times3} & [I]_{2\times2} \end{bmatrix}, \ \bar{B}_k = \begin{bmatrix} B_k \\ [0]_{2\times2} \end{bmatrix}, \ \bar{C}_k = \begin{bmatrix} C_k & [0]_{2\times2} \end{bmatrix}, \ \bar{\delta}_k = \delta_k \tag{5.44}$$

$$\bar{W}_k = \begin{bmatrix} w_k \\ w_{d,k} \end{bmatrix}, \ \bar{V}_k = v_k \tag{5.45}$$

The covariance matrices of the noises are:

$$\bar{R}_{w,k} = \begin{bmatrix} R_{w,k} & [0]_{3\times2} \\ [0]_{2\times3} & R_{wd,k} \end{bmatrix}, \ \bar{R}_{v,k} = R_{v,k} \tag{5.46}$$

where $R_{w,k}$ and $R_{wd,k}$ are covariance matrices of the process noises; $R_{v,k}$ is the covariance matrix of the measurement noises. We can assume that they are diagonal matrices:

$$R_{w,k} = diag(\alpha_1, \alpha_2, \alpha_3), \ R_{wd,k} = diag(\alpha_4, \alpha_5), \ R_{v,k} = diag(\sigma_{gyro}, \sigma_{GPS}) \tag{5.47}$$

where σ_{gyro} and σ_{GPS} are the covariance of the yaw-rate measurement and course angle measurement from GPS. The set $\left(\alpha_1, \alpha_2, \alpha_3, \alpha_4, \alpha_5, \sigma_{gyro}, \sigma_{GPS} \right)$ are tuning parameters of the estimation. In this study, trial-and-error was conducted to select the suitable values of the tuning parameters.

B. Estimation algorithm

The estimation algorithm is based on the Kalman filter in which the estimation gain is designed to minimize the estimation error covariance. The algorithm is expressed as follows, including two stages, the prediction and the correction.

Initial condition:

$$\hat{\bar{X}}_{0|0} = \begin{bmatrix} \beta_0 & \gamma_0 & \psi_0 & x_{d1,0} & x_{d2,0} \end{bmatrix}^T, \ \bar{P}_{0|0} = diag \left(P_{11}, P_{22}, P_{33}, P_{44}, P_{55} \right) \tag{5.48}$$

Prediction stage:

- Predicted state:

$$\hat{\bar{X}}_{k|k-1} = \bar{A}_{k-1} \hat{\bar{X}}_{k-1|k-1} + \bar{B}_{k-1} \bar{U}_{k-1} \tag{5.49}$$

- Prediction error covariance:

$$\bar{P}_{k|k-1} = \bar{A}_{k-1} \bar{P}_{k-1|k-1} \bar{A}_{k-1}^T + \bar{R}_{w,k} \tag{5.50}$$

Correction stage:

- Estimation gain:

$$\bar{L}_k = \bar{P}_{k|k-1} \bar{C}_k^T \left(\bar{C}_k \bar{P}_{k|k-1} \bar{C}_k^T + \bar{\delta}_k \bar{R}_{v,k} \bar{\delta}_k^T \right)^{-1} \tag{5.51}$$

- Corrected state:

$$\hat{\bar{X}}_{k|k} = \hat{\bar{X}}_{k|k-1} + \bar{L}_k \left(\bar{Y}_k - \bar{C}_k \hat{\bar{X}}_{k|k-1} \right) \tag{5.52}$$

- Correction error covariance:

$$\bar{P}_{k|k} = \left(I - \bar{L}_k \bar{C}_k \right) \bar{P}_{k|k-1} \tag{5.53}$$

5.6.4 Simulation and experimental results

Four methods of sideslip angle estimation are performed for comparison. They are summarized in Table 5.3. Except *Method 2*, other three methods are dual-rate estimation with dual-rate ratio $r = 100$.

A. Simulation results

Simulations are performed using Matlab/Simulink with the conditions as bellow:

- Model uncertainties: The tire cornering stiffness of vehicle model are $C_{fv} = C_{rv} = 7000$ (N/rad). However, the estimation model is established with $C_{fn} = C_{rn} = 10,000$ (N/rad). In other words, the uncertainties of $\Delta C_f = \Delta C_r = -3000$ (N/rad) are introduced.

- Disturbances: Lateral wind force is simulated as unknown disturbance. The general disturbance

terms including model uncertainties are simulated as follows:

$$d_1 = \frac{-2(\Delta C_f + \Delta C_r)}{mu_x}\beta + \frac{-2(\Delta C_f l_f - \Delta C_r l_r)}{mu_x^2}\gamma + \frac{2\Delta C_f}{mu_x}\delta_f + \frac{1}{mu_x}F_d \tag{5.54}$$

$$d_2 = \frac{-2(\Delta C_f l_f - \Delta C_r l_r)}{I_z}\beta + \frac{-2(\Delta C_f l_f^2 + \Delta C_r l_r^2)}{I_z u_x}\gamma + \frac{2\Delta C_f l_f}{I_z}\delta_f + \frac{1}{I_z}N_d \tag{5.55}$$

where F_d and N_d are the unknown disturbance force and the unknown disturbance yaw moment.

- Vehicle runs in a slalom test at the velocity of 25 kph.

- A scale error of 0.9 is introduced to the yaw rate measurement. This is to simulate the incorrect of yaw rate measurement in real time operation.

The simulation results are shown in Fig. 5.10, including the course angle measurement, the yaw rate estimation, and the sideslip angle estimation. Due to the use of yaw rate with scale error and model uncertainty, the estimation results of *Method 2* are considerably inaccurate. Thanks to the utilizing of GPS course angle, *Method 3* provides much better estimation in comparison with *Method 2*. However, the estimation results from method 3 are non-smooth, especially the sideslip angle. As shown in Fig. 5.10 (d), the estimation error of *Method 3* is reduced when a course angle is updated. However, during the GPS-unavailable-periods, *Method 3* is strongly influenced by model uncertainties and disturbances. *Method 4* holds the course angle innovation during the GPS-unavailable-periods to attain the smoother estimation in comparison with *Method 3*. Thanks to the disturbance accommodation, the proposed method (*Method 1*) achieves the best estimation performance. The smooth estimation performance of *Method 1* can be explained by two reasons: First, the course angle is accurate without scale error. Second, the disturbance is estimated to compensate the model uncertainties and the external disturbances (see Fig. 5.10 (e) and Fig. 5.10 (f)).

Notice: Data of the estimation results of the disturbance terms in case of cornering test are shown in the Appendix 2.

B. *Experimental results*

Experiments are performed under the same conditions as simulations. Four sideslip angle estimation methods are implemented using C-programming. RTK-GPS receiver is set to output the data every 100 millisecond. Experiments are conducted under clear sky for good GPS signal. Trial-and-error is used to tune the noise covariance matrices. The optical sensor produced by Corrsys-Datron is used to obtain the sideslip angle measurement. The results of experiment are demonstrated in Fig. 5.11, including measured course angle, estimated yaw rate and sideslip angle. As the simulation, *Method 2* which uses IMUs is poorest. By using GPS, *Method 3* and *Method 4* are shown to be superior, but they are still sensitive to model error and disturbances. Especially, *Method 3* is non-smooth and might result in uncomfortable driving feeling if this method is used in vehicle motion control system. The proposed method (*Method 1*), on other hand, is robust enough to the uncertainties.

The idea of *Method 4* is to hold the GPS measurement's innovation to fulfill the correction stages.

The proposed method (*Method 1*) also fulfills the correction stages, but with the estimation of the disturbance term. From the simulation results and experimental results, the proposed method, even heuristic to some extent, is shown to be robust to model uncertainty and external disturbance. Therefore, it can be utilized for vehicle motion control system.

For quantitative comparison, root-mean-square deviation (RMSD) of each method is calculated using the following formulation:

$$RMSD = \sqrt{\frac{1}{N} \sum_{j=1}^{N} \left(\hat{X}_j - X_{m,j} \right)^2} \tag{5.56}$$

where N is the number of samples, $\hat{X}_j$ and $X_{m,j}$ represent the estimated and measured value at jth sample.

The RMSD results are summarized in Table 5.4 where the proposed method (*Method 1*) attains the smallest RMSD values.

Table 5.3 Description of four sideslip angle estimation methods

Number	Description	Outputs	Inputs
Method 1	The proposed estimation using yaw-rate sensor and GPS based on disturbance accommodation in dual-rate Kalman filter.	+ Yaw-rate sensor	+ Front steer angle
		+ GPS course angle	+ Yaw moment
Method 2	Estimation using yaw-rate sensor and lateral accelerometer with robust observer gain proposed by Aoki *et al*.	+ Yaw-rate sensor	+ Front steer angle
		+ Accelerometer	+ Yaw moment
Method 3	Estimation using yaw-rate sensor and GPS based on conventional dual-rate Kalman filter.	+ Yaw-rate sensor	+ Front steer angle
		+ GPS course angle	+ Yaw moment
Method 4	Estimation using yaw-rate sensor and GPS based on innovation holding linear observer.	+ Yaw-rate sensor	+ Front steer angle
		+ GPS course angle	+ Yaw moment
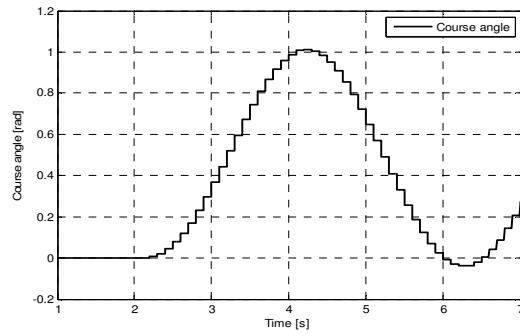
(a)   Course angle from GPS receiver
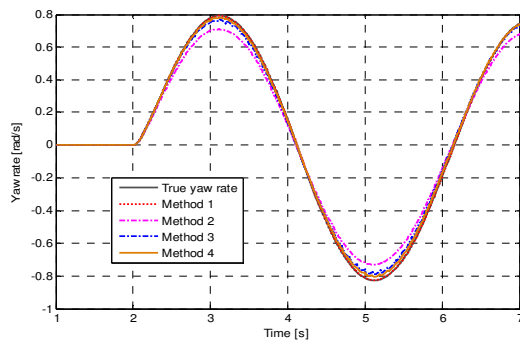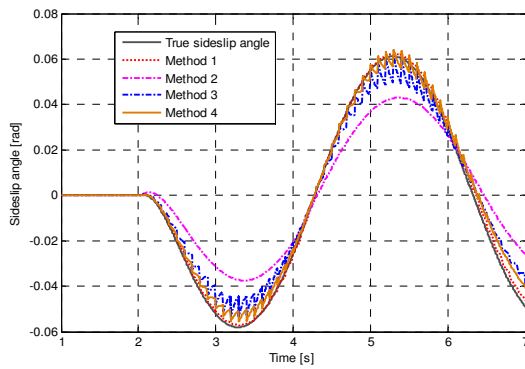
(b)   Yaw rate estimation

(c)   Sideslip angle estimation
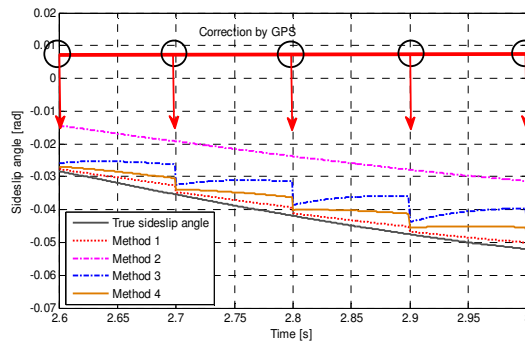
(d)   Sideslip angle estimation for several samples of GPS data

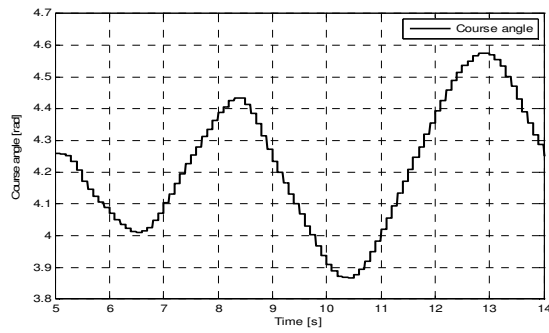Fig. 5.10 Simulation results of sideslip angle estimation.
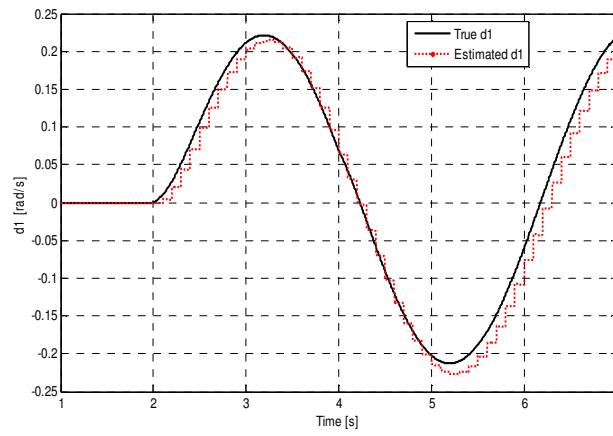
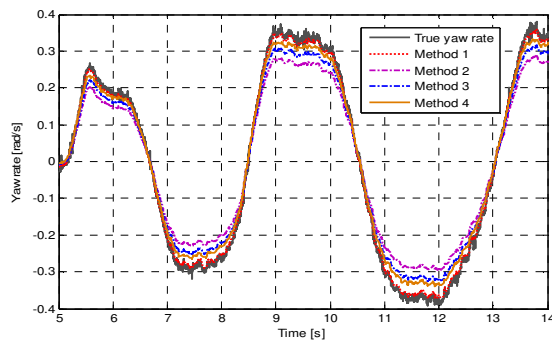(e) Estimation of the disturbance term x_{d1}
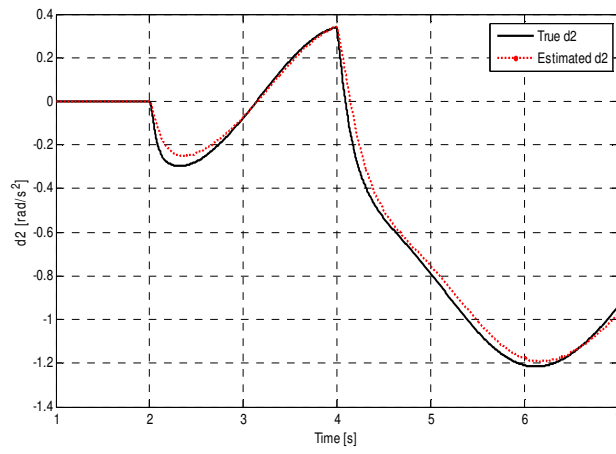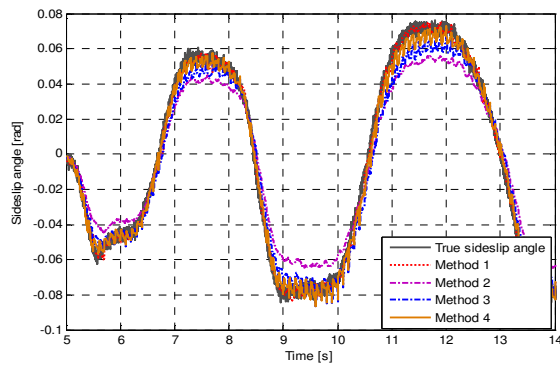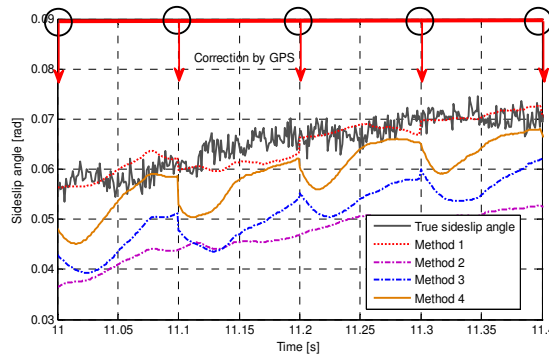

(f) Estimation of the disturbance term x_{d2}

Fig. 5.10 Simulation results of sideslip angle estimation (Continue from the previous page).

(a) Course angle from GPS receiver

(b) Yaw rate estimation

(c) Sideslip angle estimation

(d) Sideslip angle estimation for several samples of GPS data

Fig. 5.11 Experimental results of sideslip angle estimation.

Table 5.4 RMSD of four estimation methods

Estimation method	RMSD of experiment		RMSD of simulation	
	Sideslip angle [rad]	Yaw rate [rad/s]	Sideslip angle [rad]	Yaw rate [rad/s]
Method 1	0.36×10^{-2}	0.86×10^{-2}	0.16×10^{-2}	0.23×10^{-2}
Method 2	1.31×10^{-2}	5.61×10^{-2}	1.30×10^{-2}	5.60×10^{-2}
Method 3	0.88×10^{-2}	3.56×10^{-2}	0.61×10^{-2}	2.41×10^{-2}
Method 4	0.56×10^{-2}	2.52×10^{-2}	0.36×10^{-2}	1.44×10^{-2}

5.7 Lateral stability control using GPS

5.7.1 Control system design

In daily driving, there are many situations that the drivers want to perform the lane change or cornering. In these situations, it is very important to control both the yaw-rate and the sideslip angle of the vehicle. Otherwise, the yaw-rate and sideslip angle might increase considerably that the vehicle's behavior cannot follow the driver's will. For example, spin motion of the vehicle may results in serious accidents. Therefore, every vehicle must be installed the lateral stability control system to manage the yaw-rate and the sideslip angle. On commercial car, this system can be named Electronic Stability Program (ESP) in Volkswagen or Lamborghini, Vehicle Stability Assist (VSA) in Honda, Dynamic Stability Control (DSC) in Mazda, etc.

The block diagram of the lateral stability control system proposed in this thesis is shown in Fig. 5.12. The disturbance accommodation Kalman filter (DACKF) proposed in the previous section is used to provide the estimated state. The upper-layer based on 2DOF controller and disturbance rejection is used to control the yaw-rate and the sideslip angle. It outputs the front steering command and yaw moment command. These commands are fed to the lower-layer to control the active front steering systems and distribute the torque to the rear-left and rear-right in-wheel motors.
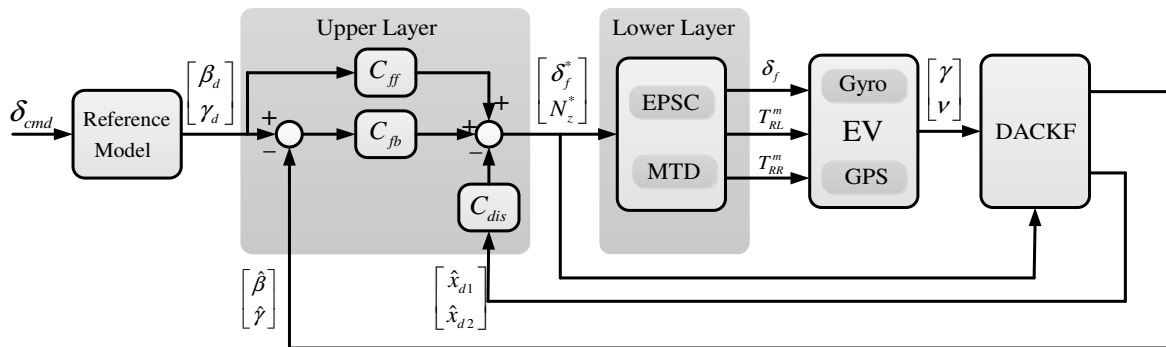

Fig. 5.12 Lateral stability control system based on DAKF using GPS and yaw-rate sensor.

A.   Reference model

The reference model is obtained based on the steady state response of sideslip angle and yaw-rate from the front steering command δ_{cmd} and the nominal values of the tire-cornering stiffness. Using the linear bicycle model, the reference values are calculated as:

$$\beta_d = \frac{1 - \dfrac{m}{2(l_f + l_r)} \dfrac{l_f}{C_{rn} l_r} u_x^2}{1 + G u_x^2} \frac{l_r}{(l_f + l_r)} \delta_{cmd} \tag{5.57}$$

$$\gamma_d = \frac{1}{1 + G u_x^2} \frac{u_x}{(l_f + l_r)} \delta_{cmd} \tag{5.58}$$

where

$$G = \frac{m}{2(l_f + l_r)^2} \cdot \frac{C_{rn} l_r - C_{fn} l_f}{C_{fn} C_{rn}} \tag{5.59}$$

B.   Upper-layer

The upper-layer includes the feed forward controller, the feedback controller, and the disturbance rejection. The nominal transfer function from the input $\begin{bmatrix} \delta_f & N_z \end{bmatrix}^T$ to the controlled state $\begin{bmatrix} \beta & \gamma \end{bmatrix}^T$ is derived as:

$$P_n = \left(s[I]_{2\times 2} - \begin{bmatrix} a_{n11} & a_{n12} \\ a_{n21} & a_{n22} \end{bmatrix} \right)^{-1} \begin{bmatrix} b_{n11} & b_{n12} \\ b_{n21} & b_{n22} \end{bmatrix} \tag{5.60}$$

where a_{n11}, …, a_{n22}, b_{n11}, …, b_{n22} are computed from the nominal parameters of the bicycle model.

$$P_n = \begin{bmatrix} \dfrac{b_{n11}s + b_{n21}a_{n12} - b_{n11}a_{n22}}{(s - a_{n11})(s - a_{n22}) - a_{n12}a_{n21}} & \dfrac{b_{n22}a_{n12}}{(s - a_{n11})(s - a_{n22}) - a_{n12}a_{n21}} \\ \dfrac{b_{n21}s + b_{n11}a_{n21} - b_{n21}a_{n11}}{(s - a_{n11})(s - a_{n22}) - a_{n12}a_{n21}} & \dfrac{b_{n22}s - b_{n22}a_{n11}}{(s - a_{n11})(s - a_{n22}) - a_{n12}a_{n21}} \end{bmatrix} \tag{5.61}$$

The feed forward controller is designed as the inverse of the matrix P_n:

$$C_{ff} = P_n^{-1} = \begin{bmatrix} C_{ff11} & C_{ff12} \\ C_{ff21} & C_{ff22} \end{bmatrix} \tag{5.62}$$

The desired closed loop system including the feedback controller and the plant (EV bicycle model) is expressed as:

$$P_{desired} = \begin{bmatrix} \dfrac{K_\beta}{s + K_\beta} & 0 \\ 0 & \dfrac{K_\gamma}{s + K_\gamma} \end{bmatrix} \tag{5.63}$$

Fig. 5.13 Front EPS motor.

In (5.63), the cut-off frequency K_β and K_γ can be determined by trial-and-error experiments. If the cut-off frequencies are too low, the response of the sideslip angle and the yaw-rate are too slow to track the vehicle motion with the desired motion. On the other hand, it is impossible to set the cut-off frequencies too high due to the limitation of the actuators' capability. The feedback controller is obtained by solving the following matrix equation:

$$\left([I]_{2\times 2} + P_n C_{fb} \right)^{-1} P_n C_{fb} = P_{desired} \tag{5.64}$$

The formulation of the feedback controller is:

$$C_{fb} = P_n^{-1} P_{desired} \left([I]_{2\times 2} - P_{desired} \right)^{-1} = \begin{bmatrix} C_{fb11} & C_{fb12} \\ C_{fb21} & C_{fb22} \end{bmatrix} \tag{5.65}$$

Finally, the disturbance rejection matrix is calculated as:

$$C_{dis} = \begin{bmatrix} b_{n11} & b_{n12} \\ b_{n21} & b_{n22} \end{bmatrix}^{-1} \tag{5.66}$$

The command from the upper-layer is obtained as:

$$\begin{bmatrix} \delta_f^* \\ N_z^* \end{bmatrix} = C_{fb} \begin{bmatrix} \beta_d - \hat{\beta} \\ \gamma_d - \hat{\gamma} \end{bmatrix} + C_{ff} \begin{bmatrix} \beta_d \\ \gamma_d \end{bmatrix} - C_{dis} \begin{bmatrix} \hat{x}_{d1} \\ \hat{x}_{d2} \end{bmatrix} \tag{5.67}$$

C. Lower-layer

The yaw moment is generated by distributing the different torques to the rear-left and the rear-right in-wheel motors. The torque of each in-wheel motors are obtained by solving the following equations in real time:

(a) Sideslip angle.

(b) Yaw-rate.

(c) Yaw moment

(d) Front steering angle
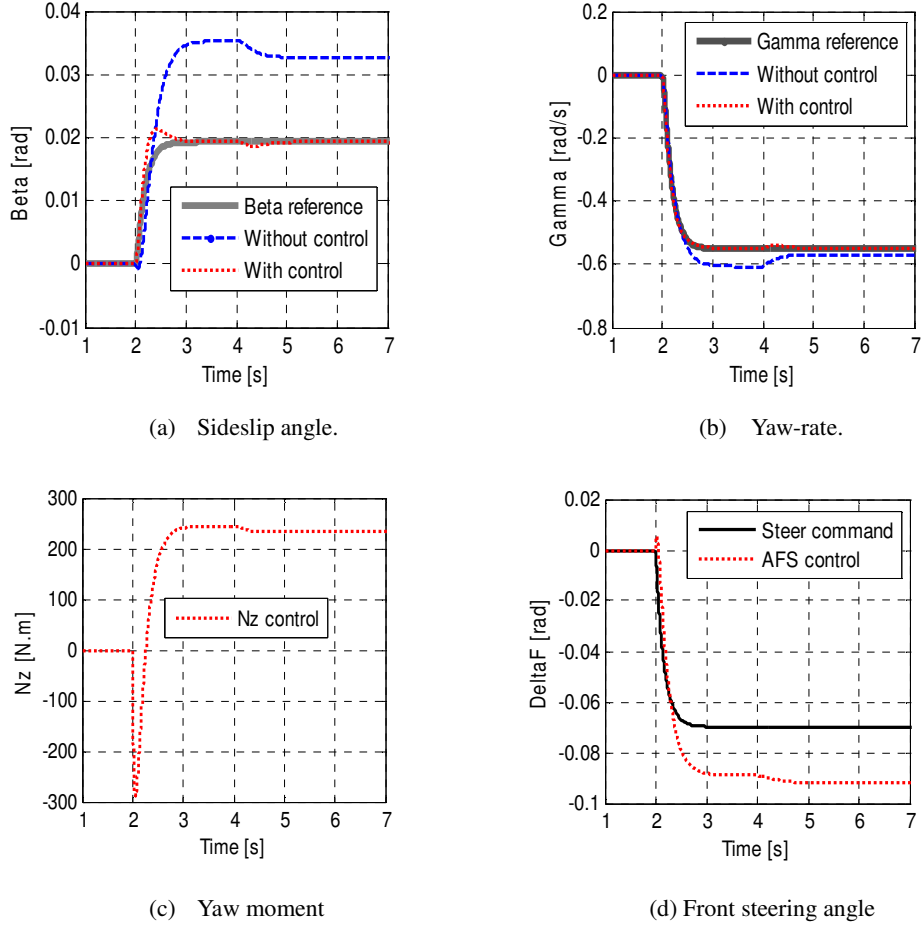
Fig. 5.14 Simulation results of lateral stability control.

$$\begin{cases} \dfrac{d_r}{2}\left(\dfrac{T_{RR}^m}{r} - \dfrac{T_{RL}^m}{r} \right) = N_z^* \\ \\ T_{RR}^m + T_{RL}^m = T_{acc} \end{cases} \tag{5.68}$$

where r is the wheel radius, T_{acc} is the acceleration command given by the driver, and d_r is the track-width between two rear wheels. T_{RL}^m and T_{RR}^m are the rear-left and rear-right in-wheel motor's torque, respectively.

An EPS motor is utilized for generating the front steering angle (Fig. 5.13). Thanks to the EPS, our system enables the steer-by-wire mode in which the steering command is generated by program without the driver's handling.

5.7.2 Simulation and experimental results

A. Simulation results

The simulation of lateral stability control is performed using Matlab/Simulink. The following conditions are set:

- Model uncertainties: The tire cornering stiffness of vehicle model are $C_{fv} = C_{rv} = 7000$ (N/rad). However, the estimation model is established with $C_{fn} = C_{rn} = 10,000$ (N/rad).

(a)   Sideslip angle (without control).

(b)   Yaw-rate (without control).

(c)   Sideslip angle (with control).

(d)   Yaw-rate (with control).
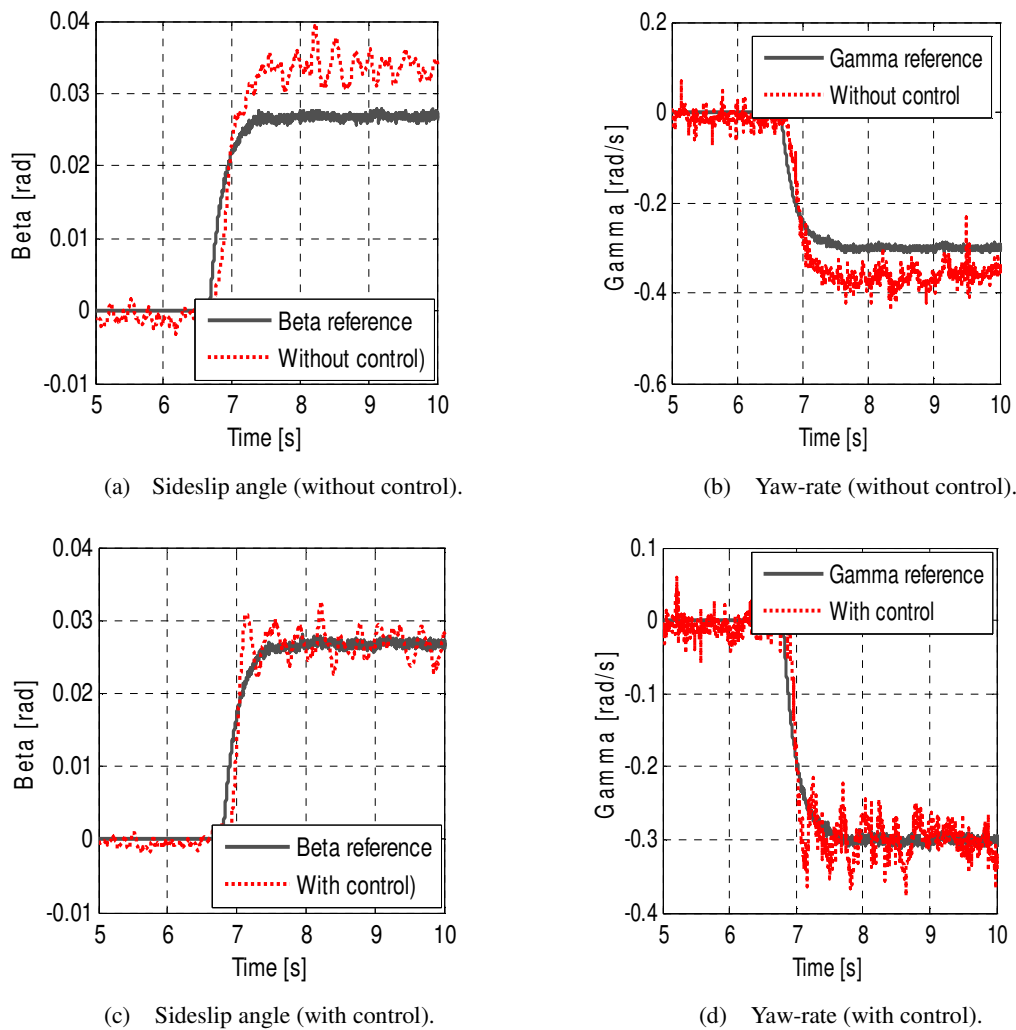
Fig. 5.15 Experimental results of lateral stability control.

- Disturbances: Lateral wind force is simulated as unknown disturbance. The wind force starts from 4 second.

- Vehicle runs in a cornering test at the velocity of 25 kph.

The simulation results are summarized in Fig. 5.14. In case of without control, the front steering angle is the same as the steering command and the yaw moment is zero. In this case, both the yaw-rate and the sideslip angle increases in comparison with the desired values. Moreover, the disturbance considerably influences the vehicle motion, as can be seen in the response of the yaw-rate and sideslip angle after 4 second. In contrast, while the proposed stability control system is applied, active front steering angle and yaw moment are generated to track the sideslip angle and the yaw-rate with their desired value. From 4 second, the disturbance only has little influence to the vehicle motion.

B. Experimental results

The cornering tests are conducted and the results are summarized in Fig. 5.15. The conditions are

set the same as the simulation. The steering command and the front steering angle are generated by the program without the driver's handling. In case of without control, both the sideslip angle and the yaw-rate increase over their references. In contrast, when the proposed lateral stability control is utilized, the response of the sideslip angle and the yaw-rate can follow the references. This means that the stability of the EV is improved.

5.8 Attitude control using GPS
5.8.1 Introduction

In recent year, autonomous vehicle technology has been developed drastically to improve the safety and the comfort of the transportation. Besides the famous Google car, a number of works on autonomous driving can be found from literature review [85], [86], [87], [88], [89]. However, almost the previous works focus on the navigation and the guidance algorithm, such as position estimation or path planning. Less effort is paid to autonomous driving from the view point of motion control. In the autonomous vehicle system, the guidance layer outputs the attitude command, often represented by yaw angle, and velocity command. Therefore, yaw angle control should play an essential task in autonomous driving. Its function is to change the attitude of the vehicle to track with a desired path generated by the path planning layer.

In low cost autonomous vehicle, course angle measured by single antenna GPS receiver can be used as the feedback of the vehicle attitude [90], [91]. However, course angle is not actually yaw angle, but the yaw angle plus the sideslip angle. Moreover, the update rate of GPS data is from 1 Hz to 50 Hz which is very slower in comparison with the control period of the actuator-the electric motor servo control. Therefore, yaw angle feedback cannot be updated at every control period. Thus, using only single-antenna GPS would limit the performance of the yaw angle control. On the other hand, Bevly *et al* propose that the yaw angle can be calculated directly by using double-antenna GPS receiver [22]. However, the cost of the double-antenna GPS system is very expensive. Moreover, this method cannot improve the update rate of yaw angle measurement. Thus, it requires the fusion of double-antenna GPS with IMU. As proposed in chapter, besides the sideslip angle, yaw angle can be estimated (at high rate) through the fusion of a single-antenna GPS with yaw-rate sensor. Transparently, this is a cost affordable method for yaw angle control system.

In this thesis, the yaw angle control system is introduced based on the disturbance accommodation Kalman filter. Some previous works just realize yaw angle control by simple feedback controller like PD or PID [92], [93]. To improve the robustness of yaw angle control, this thesis proposes the 2-degree-of-freedom control with disturbance observer. The front EPS is selected as the actuator of the yaw angle control system.

5.8.2 Modeling
A. Dynamic model

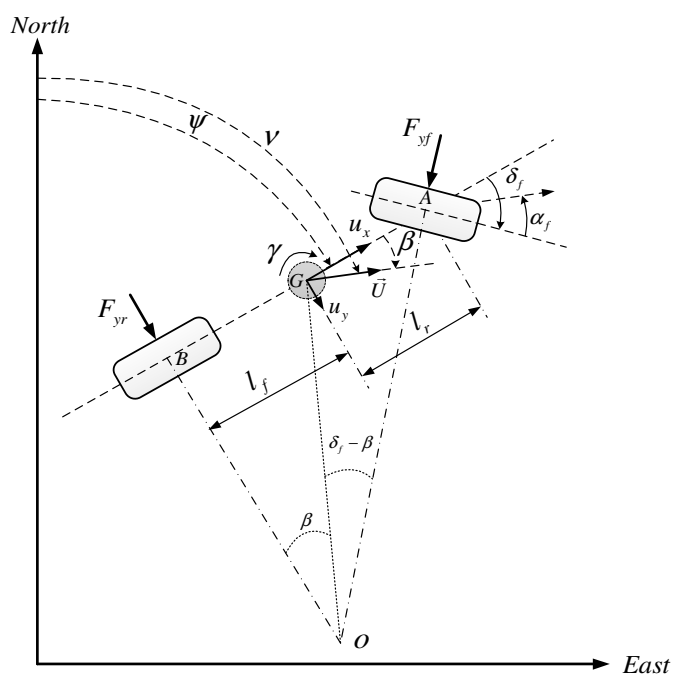Using the linear bicycle model, the transfer function from the front steering angle to the yaw

Fig. 5.16 Vehicle motion on the North-East coordinates.

angle is derived as:

$$P(s) = \frac{\psi(s)}{\delta_f(s)} = \frac{b_{21}s + (a_{21}b_{11} - a_{11}b_{21})}{s^3 + (-a_{11} - a_{22})s^2 + (a_{11}a_{22} - a_{12}a_{21})s} \tag{5.69}$$

B. A simple model

Fig. 5.16 shows the vehicle motion on the planar coordinates. Point O is the instantaneous rolling center of the vehicle. It is the intersection of lines AO and BO which are perpendicular to the orientation of the front and rear rolling wheels. OG is the instantaneous radius of the vehicle path. Apply the sine rule to the triangles OGA and OGB, the following geometric relationships are derived:

$$\tan(\delta_f)\cos(\beta) - \sin(\beta) = \frac{l_f}{OG} \tag{5.70}$$

$$\sin(\beta) = \frac{l_r}{OG} \tag{5.71}$$

Adding the above two equations together:

$$\tan(\delta_f)\cos(\beta) = \frac{l_f + l_r}{OG} \tag{5.72}$$

Assume that the vehicle velocity is almost constant and the radius of the vehicle path does not change quickly, the rate of change of orientation of the vehicle would be equal to the angular velocity of the vehicle. In other words:
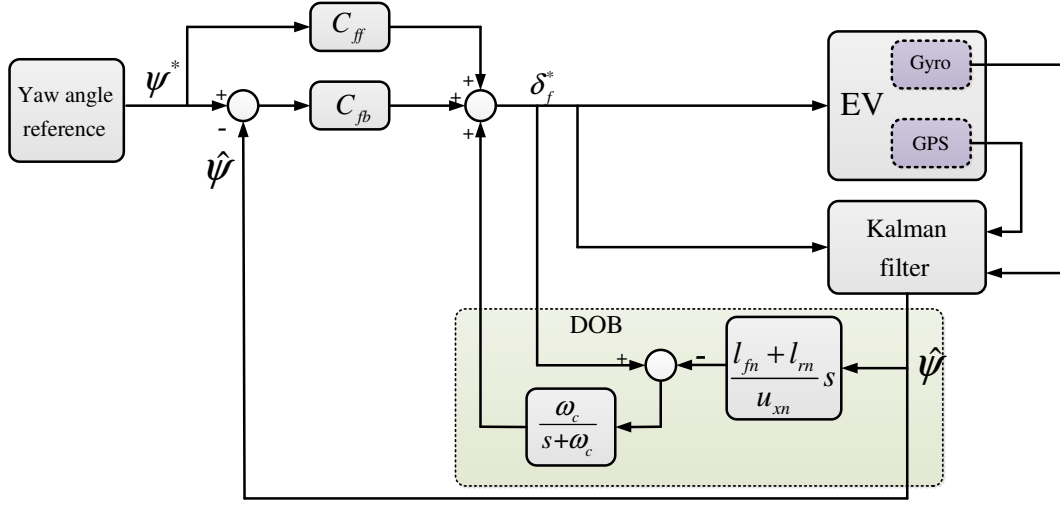
Fig. 5.17 Yaw angle control system.

$$\dot{\psi} \approx \frac{u}{OG} = \frac{u\cos(\beta)}{l_f + l_r}\tan(\delta_f) \tag{5.73}$$

Assume that the steering angle and the sideslip angle are small, we can obtain the simple model of yaw angle:

$$\dot{\psi} \approx \frac{u_x}{l_f + l_r}\delta_f \tag{5.74}$$

5.8.3 Control system design

The yaw angle control system is shown in Fig. 5.17. The disturbance accommodation Kalman filter is used to estimate the yaw angle along with the sideslip angle. Front EPS angle is used as the control signal.

A. Yaw angle reference

Autonomous navigation can be classified into three strategies: point-to-point, path following, and trajectory tracking [94]. Using the point-to-point navigation, the desired yaw angle to navigate the vehicle from point $A_1(x_1, y_1)$ to point $A_2(x_2, y_2)$ is calculated as:

$$\psi^* = \begin{cases} \tan^{-1}\left(\dfrac{x_2 - x_1}{y_2 - y_1}\right) & (y_2 > y_1) \\ \pi - \tan^{-1}\left(\dfrac{x_2 - x_1}{y_2 - y_1}\right) & (y_2 < y_1, x_2 > x_1) \\ \tan^{-1}\left(\dfrac{x_2 - x_1}{y_2 - y_1}\right) - \pi & (y_2 < y_1, x_2 < x_1) \end{cases} \tag{5.75}$$

A path can be divided into number of segments, for instance A_1A_2, A_2A_3,…, $A_{n-1}A_n$. In each segment, yaw angle reference is kept constant.
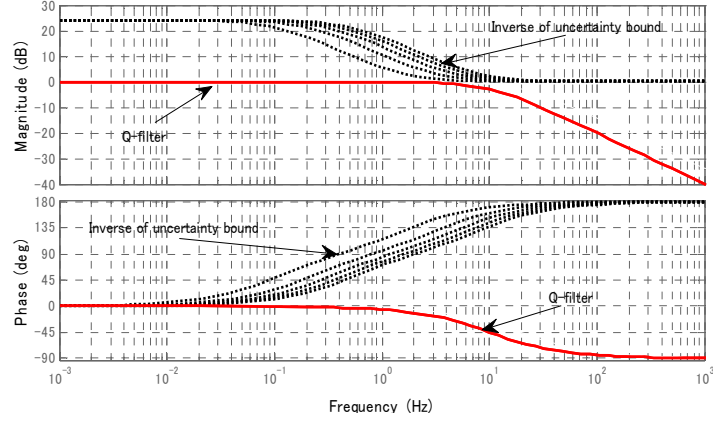
Fig. 5.18 Q-filter design for DOB (plot at the speed of 25 kph).

B. Disturbance observer (DOB)

DOB was firstly introduced by Ohnishi [95] and then further refined by many research groups. According to this method, the feedback loop includes a model of the dynamics of the exogenous reference and disturbance signal, called nominal internal model. By carefully designing the nominal model and a Q-filter, the perfect asymptotic tracking and disturbance compensation are achieved. Until now, DOB has been widely applied as a robust motion control method.

As shown in (5.69), the model of yaw angle dynamics contains cornering stiffness which is the time-varying parameter. A controller which is designed using constant cornering stiffness would be not as robust enough as requirement. Moreover, the yaw motion may be interfered by disturbance like the wind force. Therefore, to improve the robustness of yaw angle control, DOB is applied. It is possible to utilize the simple formulation in (5.74) to obtain the following nominal model:

$$P_n(s) = \frac{u_x}{(l_f + l_r)s} = \frac{k_n}{s} \tag{5.76}$$

The nominal model does not rely on tire cornering stiffness, but just the velocity and vehicle geometric distances. The yaw model can be expressed as nominal model with multiplicative perturbation as model uncertainties:

$$P(s) = P_n(s)\left[1 + \Delta(s)\right] \tag{5.77}$$

where $\Delta(s)$ is a proper boundary and stable transfer function representing the model uncertainties.

The model uncertainty transfer function is calculated as:

$$\Delta(s) = \frac{P(s) - P_n(s)}{P_n(s)} \tag{5.78}$$

Generally, both disturbances and model uncertainties are regarded as equivalent disturbance in DOB. The DOB is designed to compensate the equivalent disturbance, and the inner-loop is forced to be approximately nominal model. Robust stability of inner-loop is assured if Q-filter satisfies the

following condition for all frequencies:

$$|Q(j\omega)| < \frac{1}{|\Delta(j\omega)|} \tag{5.79}$$

Because the nominal model is the first order, Q-filter is selected as a first order low-pass-filter.

$$Q(s) = \frac{\omega_c}{s + \omega_c} \tag{5.80}$$

The cut-off frequency of the Q-filter is selected as 20 Hz in this paper. Fig. 5.18 shows that even the cornering stiffness varies (at the speed of 25 kph), the magnitude of the Q-filter is always bounded by the magnitude of the inverse of the uncertainty transfer function. In other words, the robust stability condition is satisfied.

C.   Feedback and feed-forward controller

The feed-forward controller can be designed as the inverse of the nominal model:

$$C_{ff}(s) = \frac{1}{k_n} s \tag{5.81}$$

Notice that the inner-loop with DOB can be approximately the nominal transfer function. The feedback controller can be designed using PI regulator follows:

$$\begin{cases} C_{fb}(s) = k_p + \dfrac{k_i}{s} \\ k_p = -\dfrac{(s_1 + s_2)}{k_n} \\ k_i = \dfrac{s_1 s_2}{k_n} \end{cases} \tag{5.82}$$

where s_1 and s_2 are two desired poles of the close-loop.

5.8.4 Simulation and experimental results

A.   Simulation results

The simulation is to test the ability of the control system to keep the vehicle motion straightforward to the North (desired yaw angle is zero). Simulation is performed at the speed of 25 kph. Strong lateral wind force starts to exert onto the vehicle after the simulation starts 2 second. Yaw angle control by only feedback controller (PD) is also performed for comparison. The PD controller is designed based on pole-placement using the transfer function of yaw dynamics expressed in (5.69). Uncertainty of cornering stiffness is introduced such that $C_{fv}/C_{fn} = C_{rv}/C_{rn} = 0.7$.

Simulation results are summarized in Fig. 5.19, including the response of the yaw angle, the front steering angle, and the vehicle trajectory. In case of without control, the front steering angle is always zero. As the results, the vehicle cannot follow the straightforward direction to the North under the influence of wind force. If the PD controller is applied, it takes a long time for the vehicle to recover the desired direction, but lateral position off-set occurs. Thanks to the proposed control system with DOB, the disturbance is suppressed and model uncertainty is compensated. Consequently, the vehicle

can quickly recover the reference yaw angle. Moreover, the lateral position error of the proposed control system is considerably reduced in comparison with that of the PD controller.
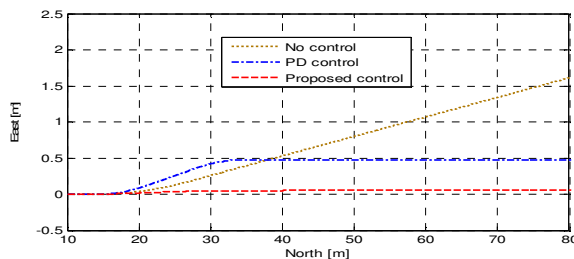
B.   Experimental results

To evaluate the proposed yaw angle control scheme, we conduct the autonomous driving test. In the first experiment, the vehicle trajectory is desired to be parallel with the direction of the test course. Yaw angle reference is pre-calculated by using (5.75). Experimental results including yaw angle response, front steering angle, and vehicle trajectories are shown in Fig. 5.20. In case of without control, the front EPS motor always keeps the front steering angle to be zero. Therefore, the yaw angle and trajectory of vehicle cannot follow the references. In contrast, when applying the proposed control scheme, the front steering angle is generated to compensate the influence of disturbances. As a result, the tracking of yaw angle and trajectory are successfully achieved.
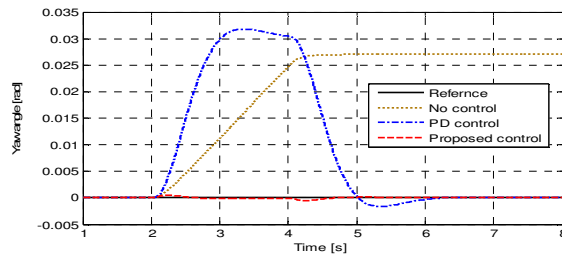
(a)   Yaw angle.
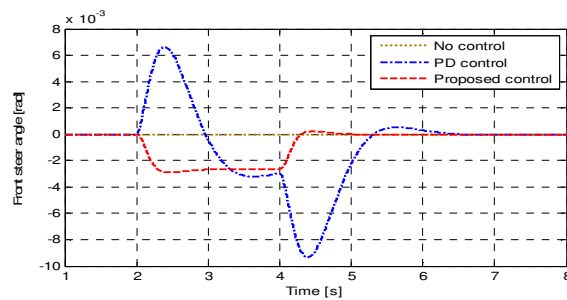
(b)   Front steering angle.

(c)   Vehicle trajectory.

Fig. 5.19 Simulation results of attitude control based on yaw angle control.
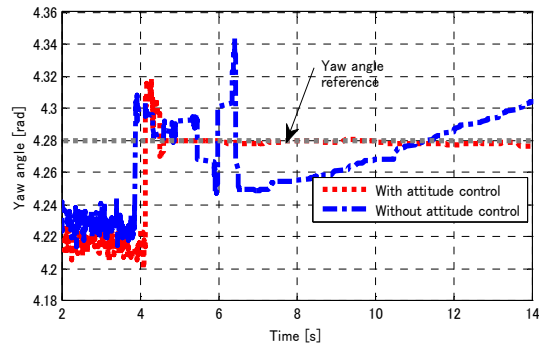
(a)　Yaw angle.
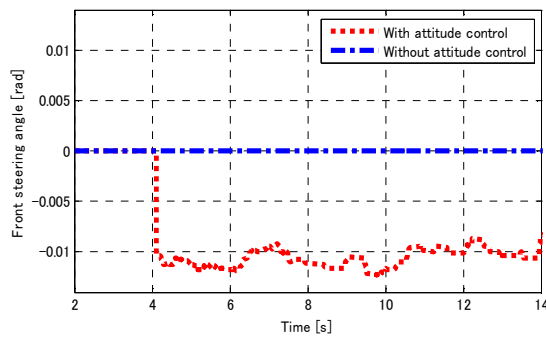
(b)　Front steering angle.

(c)　Vehicle trajectory (without control)

(d)　Vehicle trajectory (with control)

Fig. 5.20 Experimental results of attitude control based on yaw angle control.
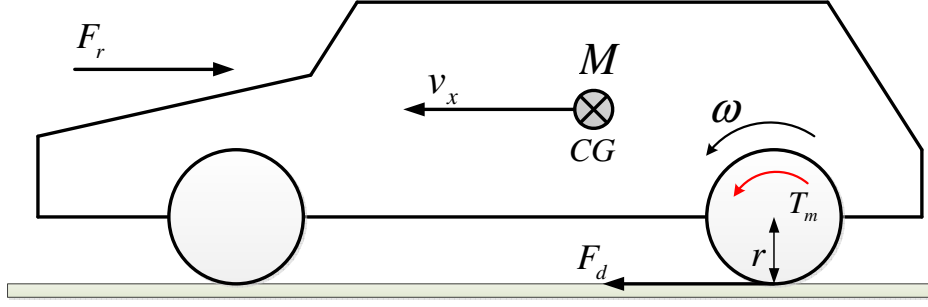
Fig. 5.21 Longitudinal model.

5.9 Traction control using GPS

5.9.1 Longitudinal model

The longitudinal model (one-wheel-driven) of the vehicle is shown in Fig. 5.21. Assume that the vehicle is in acceleration mode, the following equations demonstrate the longitudinal motion:

$$I_\omega \dot{\omega} = T_m - rF_d \tag{5.83}$$

$$m\dot{v}_x = F_d - F_r \tag{5.84}$$

$$\lambda = \frac{r\omega - v_x}{r\omega} \tag{5.85}$$

where F_d is the driving force at tire-road contact path, F_r is the driving resistant force, T_m is the motor torque, r is the wheel radius, m is the vehicle mass, I_ω is the wheel moment of inertia, λ is the wheel slip ratio.

5.9.2 Control system design

To maintain the safety traction on slippery road, the wheel slip ratio control is designed. The control system is shown in Fig. 5.22. Taking the advantage of EVs, the in-wheel motor torque is selected as the control signal. The sliding mode controller is utilized for wheel slip ratio control.

A. Design of longitudinal velocity estimation

Assume that the vehicle is running in the straight direction, the following dual-rate model is established for longitudinal velocity estimation:

$$\begin{cases} x_{k+1} = A_k x_k + B_k u_k + w_k \\ \quad y_k = C_k x_k + \delta_k v_k \end{cases} \tag{5.86}$$

$$x_k = v_x, u_k = a_x, y_k = v_{GPS,k} \tag{5.87}$$

$$A_k = 1, \quad B_k = T_c, \quad \begin{cases} \text{if GPS data update:} \qquad C_k = \delta_k = 1 \\ \text{if GPS data unavailable: } C_k = \delta_k = 0 \end{cases} \tag{5.88}$$

where v_x is the longitudinal velocity, a_x is the longitudinal acceleration obtained by accelerometer, w_k and v_k are Gaussian noises.
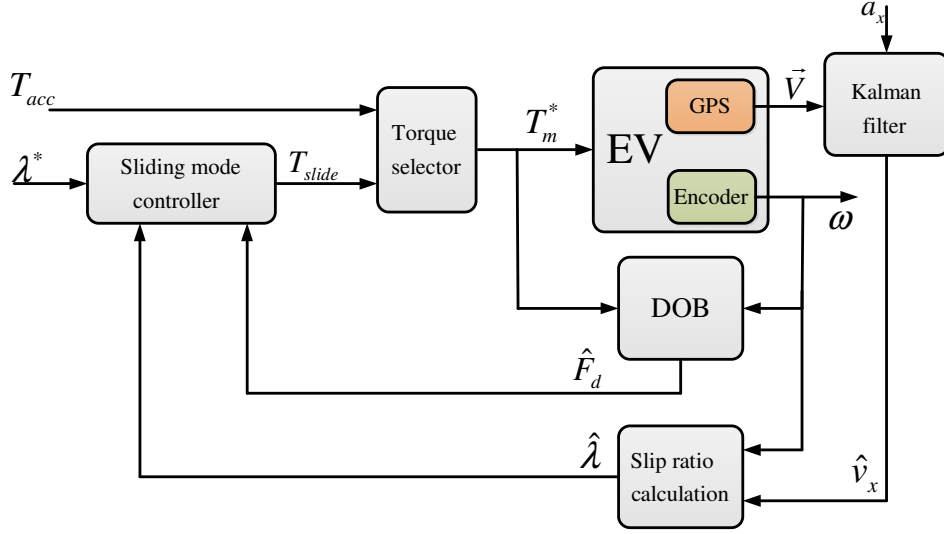
Fig. 5.22 Wheel slip ratio control system.

A dual-rate Kalman filter is used to estimate the longitudinal velocity. Then, using (5.83) the slip ratio is computed.

B. *Design of the sliding mode controller*

From (5.83)~(5.85) the dynamics model for slip ratio control is established as:

$$\dot{\lambda} = -\frac{\dot{v}_x}{v_x}\lambda + \frac{v_x}{I_\omega r \omega^2}T_m - \frac{\dot{v}_x}{v_x} - \frac{v_x}{I_\omega \omega^2}F_d \tag{5.89}$$

The sliding surface, the reaching law, the Lyapunov function *V* and its derivative are expressed as follows:

$$S = \left(\lambda - \lambda^*\right) \tag{5.90}$$

$$\dot{S} = -LS - Qsat(S) \tag{5.91}$$

$$V = \frac{1}{2}S^2 \tag{5.92}$$

$$\dot{V} = S\dot{S} = -LS^2 - QSsat(S) \tag{5.93}$$

In (5.91), *L* and *Q* are selected as positive constants. Thus, the derivative of the Lyapunov function is always negative. In other words, the stability of the control system is confirmed. A sliding mode control law is obtained as follows with the estimated slip ratio and the observation of driving force:

$$T_{slide} = \frac{I_\omega r \omega^2}{\hat{v}_x}\left[\frac{\dot{\hat{v}}_x}{\hat{v}_x}(1-\lambda) + \dot{\lambda}^* + \frac{\hat{v}_x}{I_\omega \omega^2}\hat{F}_d - LS - Qsat(S)\right] \tag{5.94}$$

The driving force observer is an advantage of in-wheel electric vehicles. The design of driving force observer can be found in many papers, such as in [68].
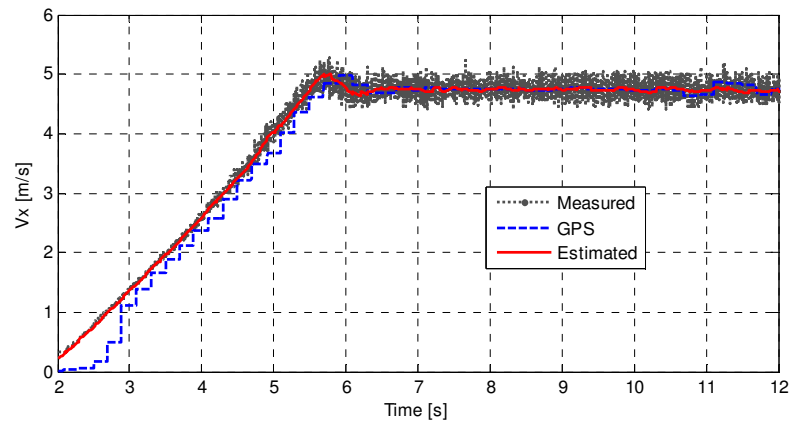
Fig. 5.23 Longitudinal velocity estimation using GPS.

Fig. 5.24 Traction control on slippery road.

5.9.3 Experimental results

The experimental results of longitudinal velocity estimation using GPS is shown in Fig. 5.23. In this test, the GPS update rate is 5 Hz, but the velocity can be estimated at the rate of 1 kHz. Comparing with the longitudinal velocity measured by optical sensor, the estimated velocity is accurate enough for motion control.

The low friction sheets covered with water is placed on the test course to simulate the slippery road (Fig. 5.24). The driver accelerates the vehicle from a starting point near by the low friction sheets. Because the vehicle motion is straight in this test, it is necessary to show the results of only one wheel (the rear left, for instance). In case of without control, the motor torque is kept constant as the driver's command (Fig. 5.25 (a)). As the results, the wheel slip ratio increases considerably (Fig. 5.25 (b)) and the slip occurs. When the proposed slip ratio control based on sliding mode theory is applied, the motor torque is controlled and reduced in the low friction sheets as shown in Fig. 5.26 (a). Wheel slip ratio follows the reference value of 0.1 (Fig. 5.26 (b)) and the safe traction of EV is achieved.
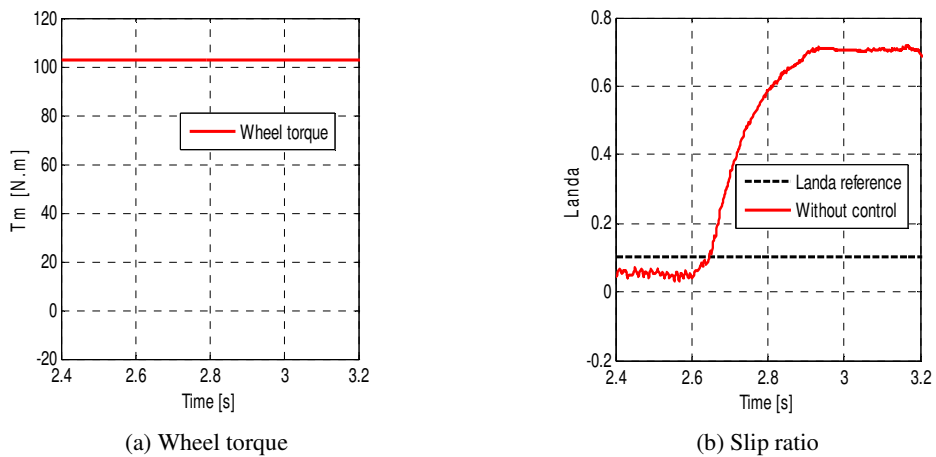
(a) Wheel torque

(b) Slip ratio

Fig. 5.25 Longitudinal motion on slippery road (without control).
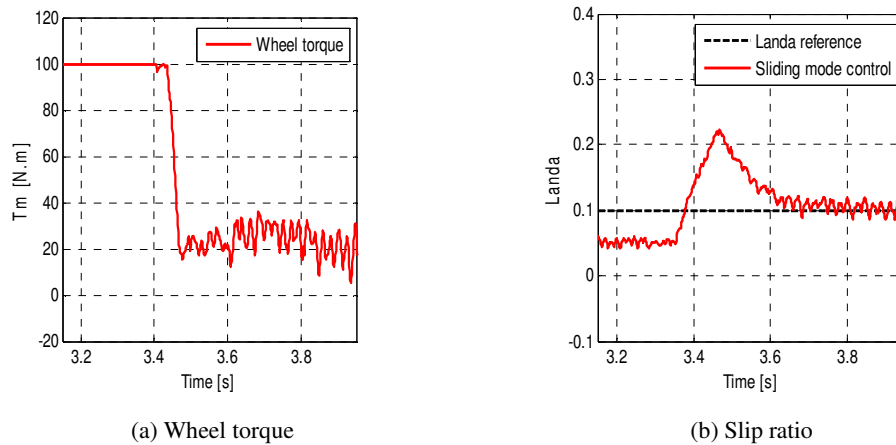

(a) Wheel torque

(b) Slip ratio

Fig. 5.26 Longitudinal motion on slippery road (with control).

5.10 Discussion

In this chapter, we design the electric vehicle motion control system based on the fusion of GPS receiver with inertial sensors. The main contribution of this chapter is to utilize the disturbance accommodation Kalman filter to enhance the robustness of sideslip angle estimation using single antenna GPS and yaw-rate sensor. Simulations and experiments are performed to verify the advances of the proposed estimation in comparison with other estimation methods. Besides the sideslip angle, the yaw angle and the longitudinal velocity are estimated using GPS. Three motion controls of EV are designed and tested: lateral stability control, attitude control, and wheel slip-ratio control.

Chapter 6:

Motion Control of Chip Mounting Machine

"Computers are incredibly fast, accurate, and stupid. Human beings are incredibly slow, inaccurate, and brilliant. Together they are powerful beyond imagination."

Albert Einstein

6.1 Chip mounting machine

Chip mounting machine is a type of industrial machine which uses electrical actuators to place the chips onto a printed circuit board. To satisfy the development of electronic devices manufacturing, chip mounting is desirable to perform high speed and high precision operation. Fig. 6.1 shows the photo of the chip mounting machine model CM602-L produced by Panasonic. With 12 nozzles, it can mount one hundred thousand chips per hour with the accuracy of ±40µ/chip.

There are two main tasks in the operation of a chip mounting machine. The first is to detect the position to place the chip. The second is to move the nozzle (as fast as possible) to the desired position. To perform these tasks, a chip mounting machine can be equipped with a vision system and the motor servo systems. Fig. 6.2 shows the basic component of the chip mounting machine with the nozzle, the camera, the two linear motors as actuator, and the circuit board. The vision system serves as the "eyes" while the motor servo systems are the "hand" of the machine. The design of the controller that manages the "eyes" and the "hand" is our interests in this study.

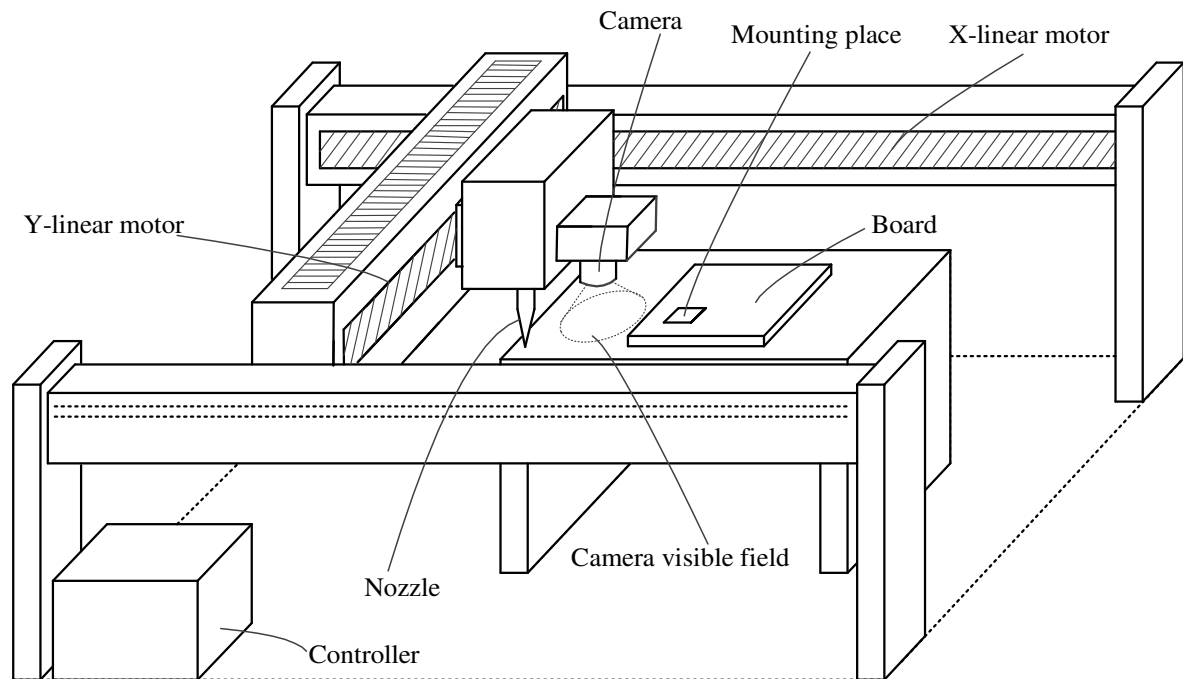Fig. 6.1 Chip mounting machine CM602-L (Panasonic).

Fig. 6.2 Main components of a chip mounting machine.

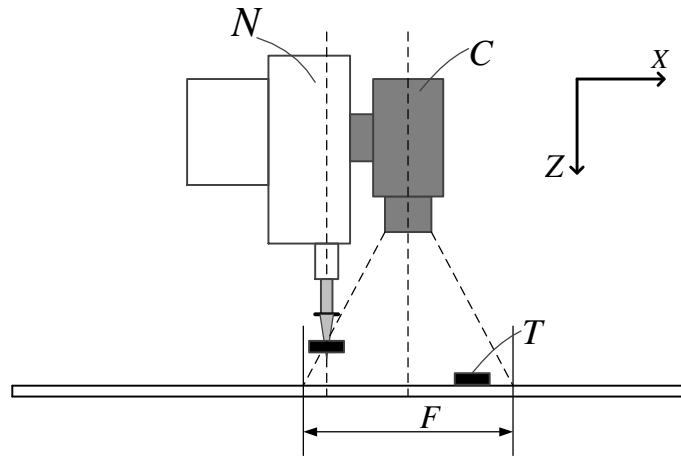## 6.2 Visual servo – the key of chip mounting machine

Since the early works by Shirai and Inoue [96], visual servo has been considerably developed and widely applied in various automated manufacturing systems. Visual servo is a promising solution in assembling machine of electronic products which requires high speed and high accuracy. As the miniature component trend in electronic devices, it is essential to overcome the possible position errors due to the inevitable reasons, such as operating temperature, ageing of machine, vibration induced from environments, and the dispersion among components, etc.

The two main tasks of the chip mounting can be realized using the visual servo. The operation of the visual servo for chip mounting is demonstrated in Fig. 6.3. For the sake of simplicity, one-axis motion is used for explanation.

(a)   The nozzle N is attached with a camera C. From the initial position, the linear motor moves the nozzle (with camera) along the X axis in the non-visual servo mode because the target is not detected. The distance F represents the visible field of the camera.

(b)   The target T is detected when it is insight the field F. Based on the image processing, the relative distance between the target and the vertical axis of the nozzle is calculated. Right after that, the visual servo mode starts. The control system generates the command to the linear motor drives that the nozzle is moved toward the target position.

(c)   The goal of the visual servo is that the vertical axis of the nozzle can finally match with the target position.
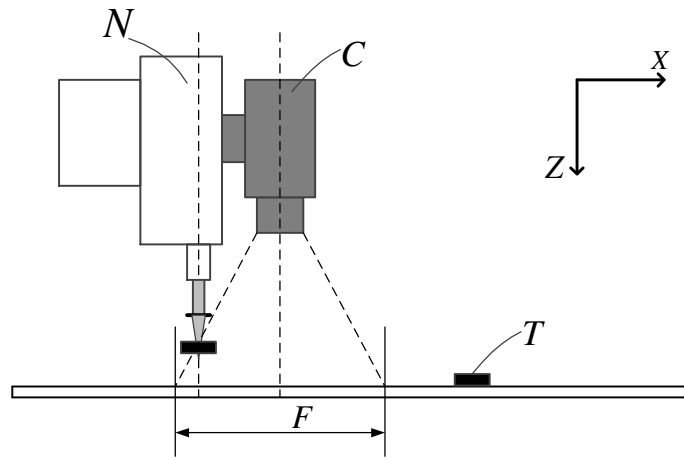
(a) Non-visual servo mode

(b) Target detected, visual servo starts.
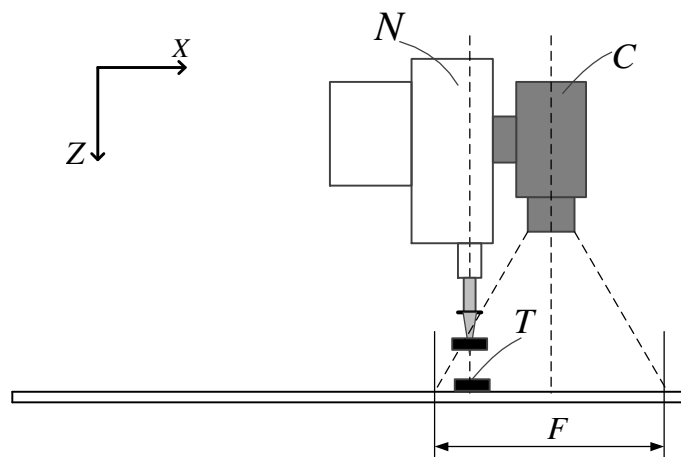
(c) Target tracking

Fig. 6.3 Visual servo operation in chip mounting machine.

6.3 Experimental setup of a visual servo system

In order to develop the key technology for chip mounting machine, we focus on the visual servo control in this study. A one-axis system is established for the sake of simplicity.

6.3.1 Experimental system

A. System specification

The experimental system used in this research is shown in Fig. 6.4. It consists of a one-axis-linear-stage, a high speed CMOS camera, a motor driver, an image processing unit (IPU), and a motion control unit (MCU). The specifications of the system are summarized in Table 6.1. The target is a black line drawn on a plastic plate which is placed in parallel with the linear stage. Visual information from the camera mounted on the stage is transferred to IPU to obtain the relative position between camera and target center. The position of camera on the stage is measured by linear encoder. The MCU generates the current command to drive the linear motor such that the camera axis is moved to track the target center line with the accuracy less than 3µm.

B. Experiment method

The experiment is conducted as follows. At the initial status, the distance between the camera and the target is $L+\Delta L$ as shown in Fig. 6.5 (a). Here L represents the default movement of the linear stage while ΔL is a random number standing for environmental error. ΔL is assumed to be smaller than a half of the camera's visible field which is 2.5 mm in this research. From the initial position, the camera is moved toward the target in non-visual-servo mode over the distance L. When the target is detected by the IPU, visual servo mode starts for target tracking, as shown in Fig. 6.5 (b) .

C. Problems of the system

The sampling time of the relative position measurement is 2 ms which is 20 times longer than the control period of linear motor drive. Moreover, time delay of the IPU is found to be 3 ms which is 30 times longer than the motor control period, as demonstrated in Fig. 1.6.
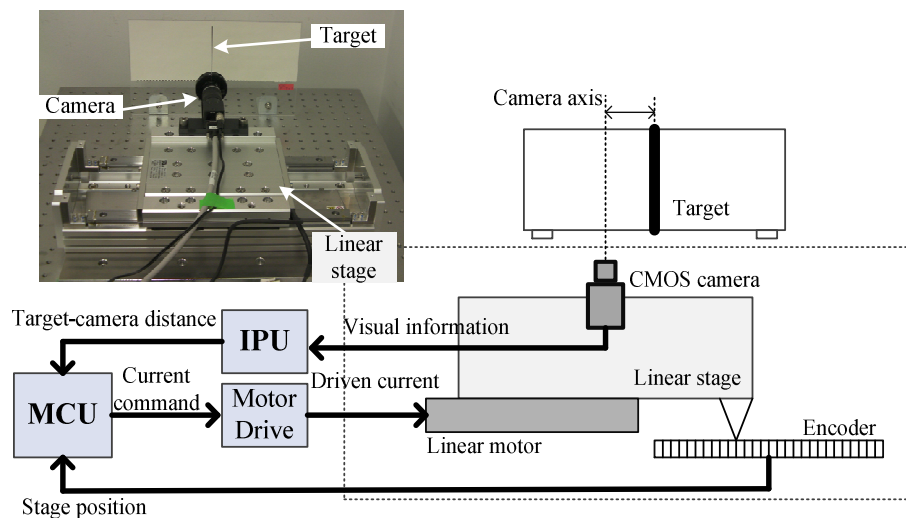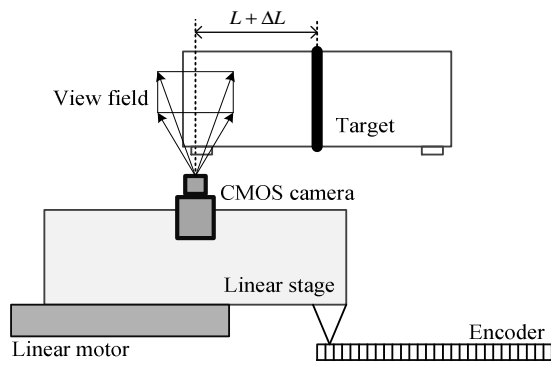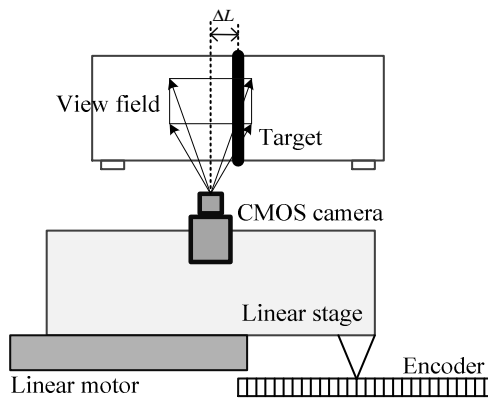

Fig. 6.4 Main components of a chip mounting machine.

(a) Initial status when the distance is $L+\triangle L$.

(b) Visual servo starts as the target is detected.

Fig. 6.5 Operation of the experimental system.

Table 6.1 Specification of the experimental system

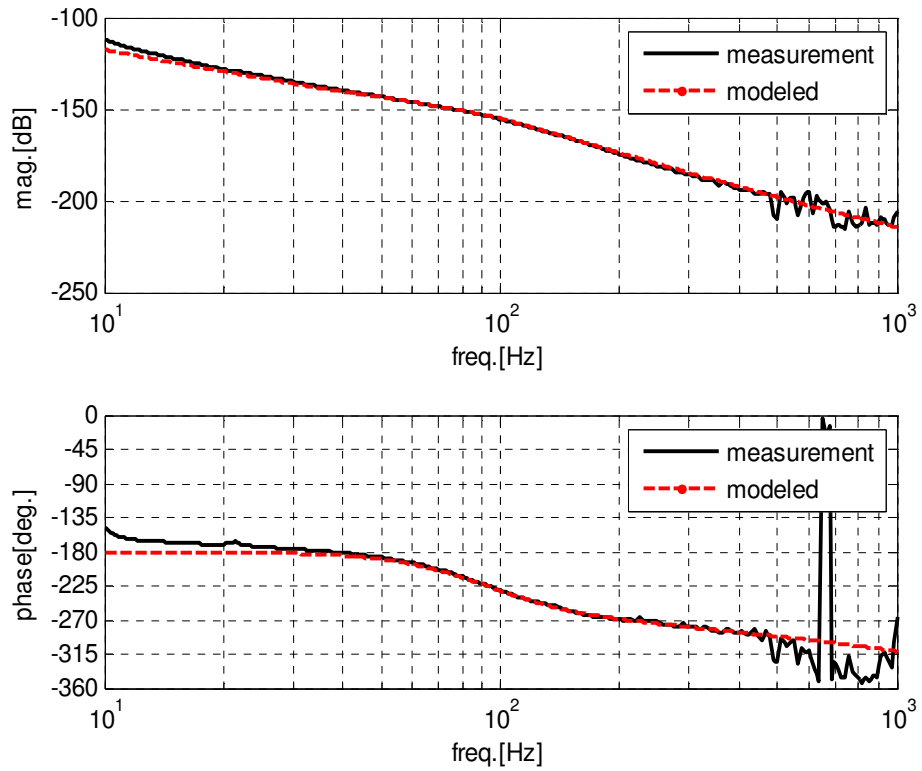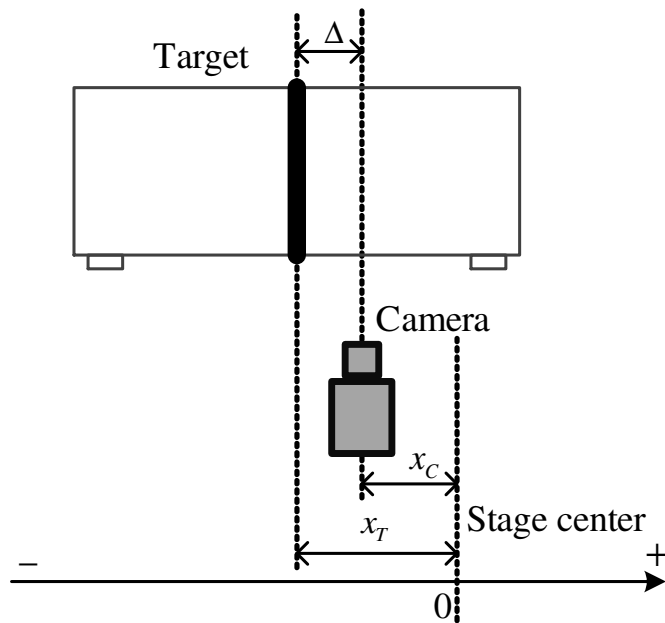| Linear stage	
Acceleration	4 G
Maximum velocity	700 mm/s
Position accuracy of encoder	0.1 μm
COMS camera	
Image size	640x480 pixel
View field width	5 mm
Pixel resolution	7.8 m/pixel
Sampling time	2 ms
Image processing unit (IPU)	
FPGA Board	Spartan 6
Processing period	2 ms
Time delay	3 ms
Position accuracy	1 μm
Motion control unit (MCU)	
Name	SH7760
Operating system	T-Engine
Control period	100 μs
Experimental operation	
Default moving length (L)	1 ~ 70 mm
Environmental position error ($\triangle L$)	< 300 μm

Fig. 6.6 Bode diagram: experiment and modelling.

Fig. 6.7 A coordinates for camera and target.

6.3.2 System modeling

A. Model of the linear stage

The controlled plant includes the servo drive and the linear stage. The control input to this plant is the current command generated by the MCU and the output is the stage position measured by linear encoder. By conducting experiment with sub-analyzer, the Bode diagram of the plant can be obtained as in Fig. 6.6.

The plant transfer function is obtained as follows though parameter fitting:

(6.1) $$P_x(s) = \frac{1}{Ms^2} + \frac{K}{s^2 + 2\xi\omega s + \omega^2}$$ (6.1)

where $M = 200$ [kg.count/N] is the equivalent mass and count is the unit of current command in the counter of MCU. $\xi = 0.55$ is the damping coefficient, $\omega = 2\pi \times 92$ [rad/s] is the resonant frequency, and $K = -5.5 \times 10^{-3}$ is the residue of resonance.

B. A state space model

To establish the model for estimating the distance between the target and the camera, the coordinates in Fig. 6.7 is used. The distance Δ is defined as:

$$\Delta = x_T - x_C$$ (6.2)

In the chip mounting machine, the target is fixed, we can write:

$$\dot{\Delta} = -\dot{x}_C$$ (6.3)

From (6.1) and (6.3), the following state space model is established:

$$\dot{x}(t) = Ax(t) + Bu(t)$$ (6.4)

$$y_1(t) = C_1 x(t)$$ (6.5)

$$y_2(t) = C_2 x(t - t_d)$$ (6.6)

$$x = \begin{bmatrix} z_1 & z_2 & z_3 & z_4 & \Delta \end{bmatrix}^T, \ u = I_q, \ y_1 = x_C, \ y_2 = \Delta$$ (6.7)

$$A = \begin{bmatrix} 0 & 1 & 0 & 0 & 0 \\ 0 & 0 & 1 & 0 & 0 \\ 0 & 0 & 0 & 1 & 0 \\ 0 & 0 & -\omega^2 & -2\xi\omega & 0 \\ 0 & -\frac{\omega^2}{M} & -\frac{2\xi\omega}{M} & -\frac{1+KM}{M} & 0 \end{bmatrix}, \ B = \begin{bmatrix} 0 \\ 0 \\ 0 \\ 1 \\ 0 \end{bmatrix}$$ (6.8)

$$C_1 = \begin{bmatrix} \frac{\omega^2}{M} & \frac{2\xi\omega}{M} & \frac{1+KM}{M} & 0 & 0 \end{bmatrix}, \ C_2 = \begin{bmatrix} 0 & 0 & 0 & 0 & 1 \end{bmatrix}$$ (6.9)

The above system has an input, the current command of the linear motor drives, and two output measurements: y_1 from linear encoder, and y_2 from the image processing unit. While y_1 is sampled at every control period, y_2 is delayed ($t_d = 3$ms) and its sampling time is 20 times longer than that of y_1.

6.4 Sub-pixel image processing

The sub-pixel image processing algorithm is shown in Fig. 6.9 including three steps.

1) Projection of pixel value: The IPU builds a projection histogram. Each component of this histogram is the pixel value in each column of an obtained image.

2) Detection of target edges: A sub-pixel edge of the target is detected by using the histogram (as shown in Fig. 6.8 (b)).

3) Calculation of the center of the target: Cross points between the envelope of the histogram and a certain threshold value are calculated using the following formulation:

$$x = x_1 + (x_2 - x_1)\frac{th - y_1}{y_2 - y_1} \tag{6.10}$$

Two cross points are determined as the edges of the target in sub-pixel resolution, and the middle point of the detected target edges is calculated as the center of the target. By using this algorithm, the target position can be detected with the accuracy less than 1.0 micrometer.
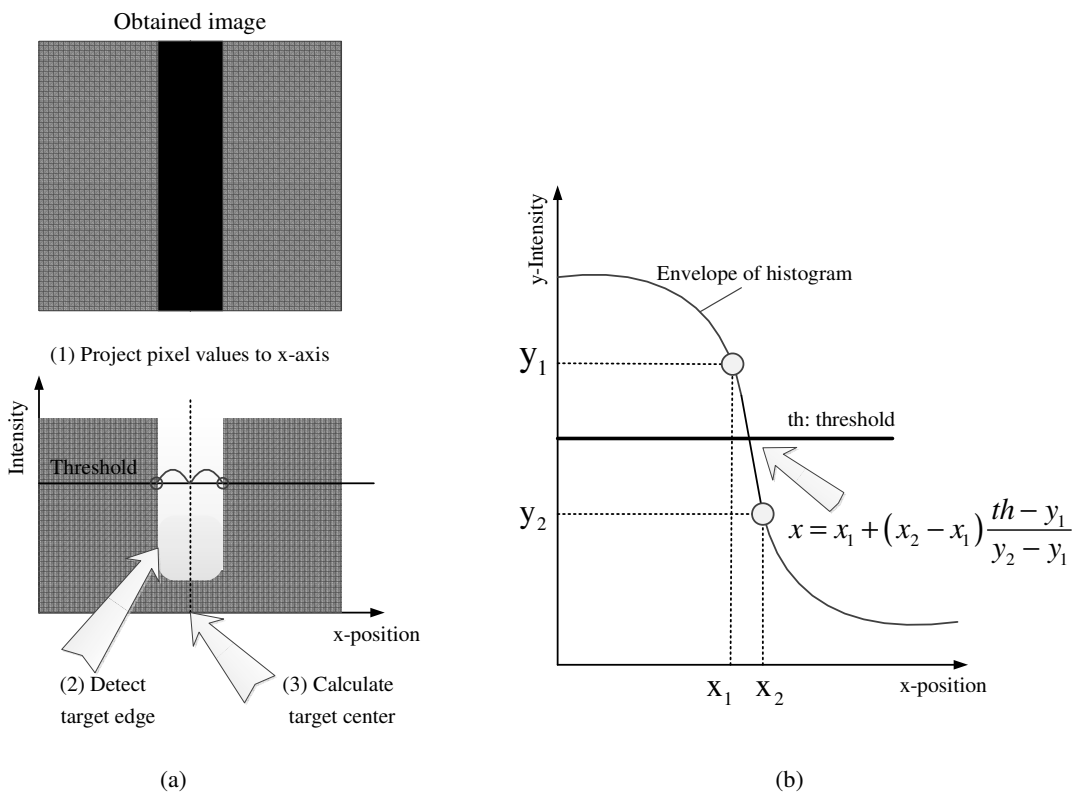

Fig. 6.8 Sub-pixel image processing algorithm.

By using a field-programmable gate array (FPGA) as a processing core of the IPU, the algorithm described above is executed at the same sampling rate as that of the high-speed CMOS camera. A simplified timing chart of the processing is shown in Fig. 6.9. After a certain exposure time to obtain an image, the camera transfers the pixel values to the IPU which builds the projection histogram. After that, the IPU calculates the center position of the target, and sends the results to the MCU. As the time required for exposure, pixel transfer, and image processing, a time delay of 3.0 milliseconds is found. It means that when the vision information is sent to the MCU, it expresses the target position at 3.0 milliseconds before the present (see Fig. 1.6 in the Chapter 1).
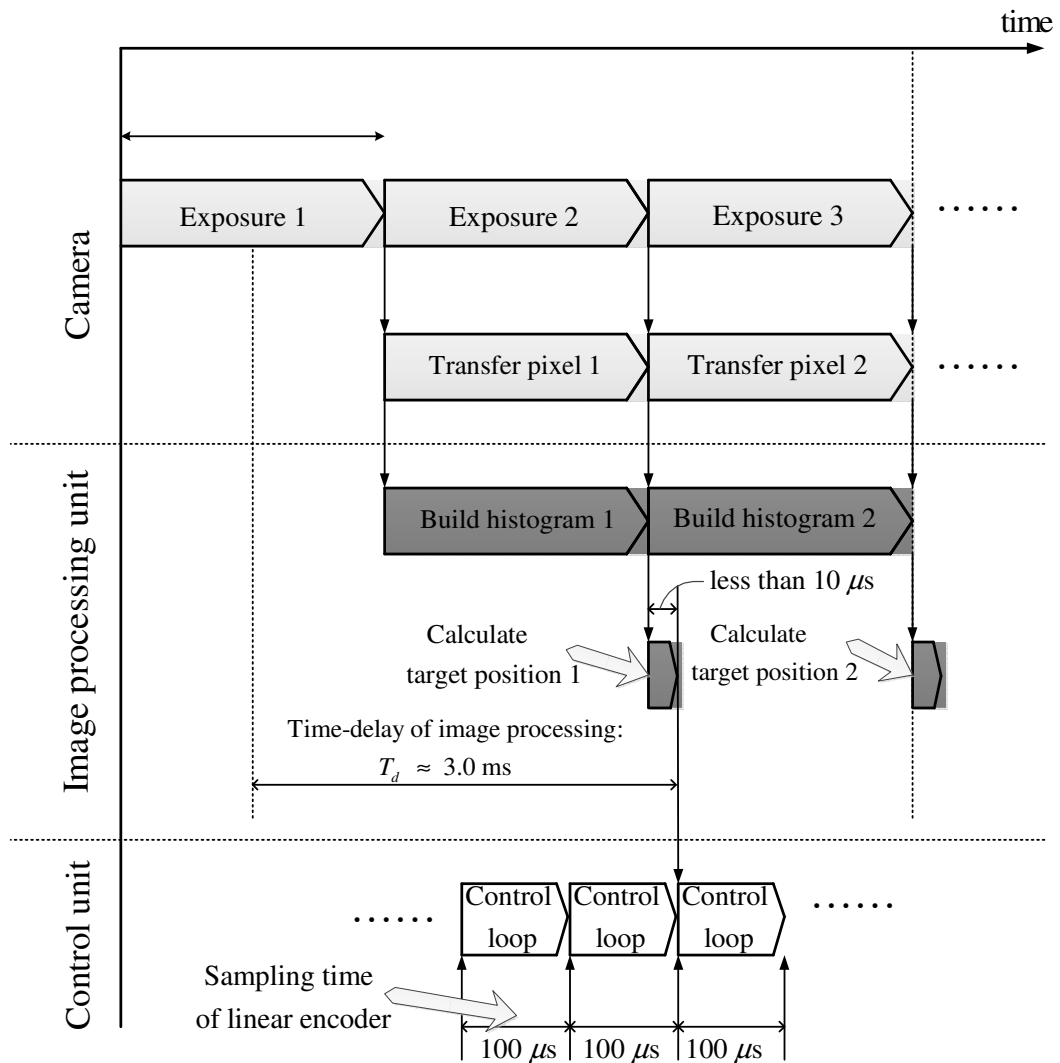
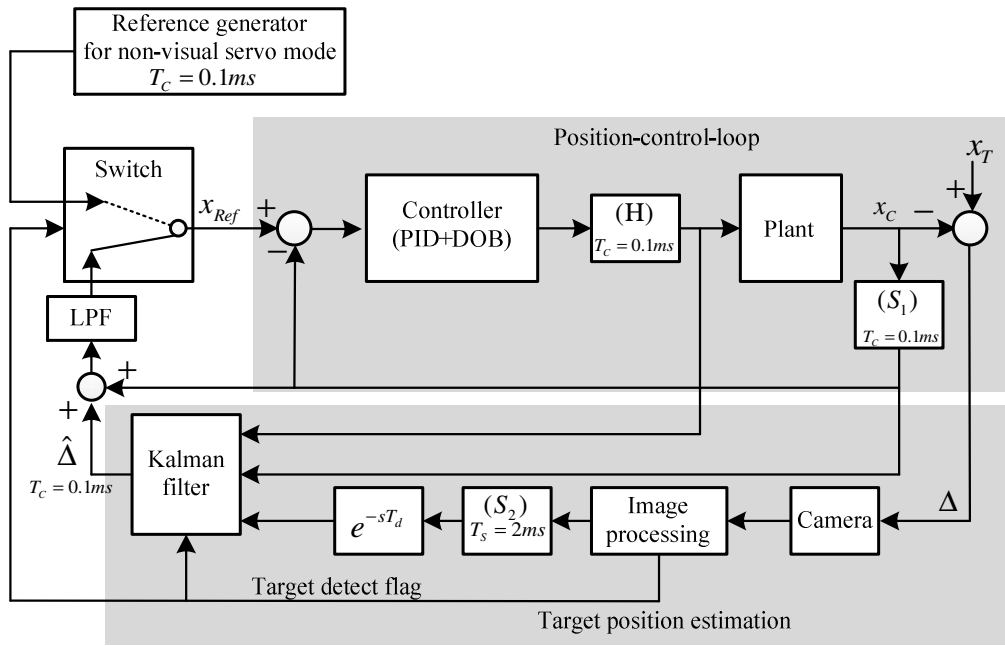Fig. 6.9 Timing chart of image processing.

Fig. 6.10 Visual servo control system.

6.5 Design of the visual servo control system

The visual servo control system is shown in Fig. 6.10. A Kalman filter is designed to estimate the target position at every control period of the linear motor drives and compensate the time delay of the image processing unit. The position control loop is used to control the linear motor stage such that the camera axis can track the target. The reference generator is used to provide the position reference in non-visual servo mode. The reference trajectory is calculated considering the manufacturing requirement, such as the maximum velocity, maximum acceleration, and the maximum jerk. When the image processing unit detects the target, it sets the "target-detect-flag" from zero to one and sends the flag to the Kalman filter and the switch. Right after that, the Kalman filter starts to estimate the target position. Using the estimates from the Kalman filter, the position reference for visual servo mode is calculated as follows:

$$x^* = x_C + \hat{\Delta} \tag{6.11}$$

where x_c is the camera position obtained through linear encoder. A low-pass-filter is utilized to smooth the reference value.

6.5.1 Design of the Kalman filter

Using the continuous time state space model (6.4) ~ (6.9), the following discrete-time stochastic model is established:

$$x_{k+1} = A_k x_k + B_k u_k + w_k \tag{6.12}$$

$$y_{1,k} = C_{1,k} x_k + v_{1,k} \tag{6.13}$$

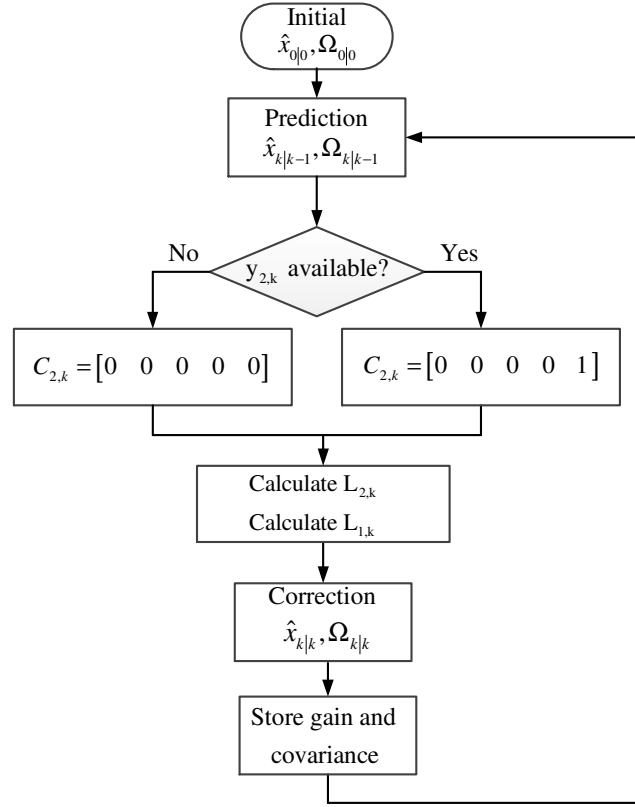$$y_{2,k} = C_{2,k} x_{k-d} + \delta_{2,k} v_{2,k} \tag{6.14}$$

Fig. 6.11 Target position estimation algorithm.

where the state matrix A_k and input matrix B_k are obtained using the following transformation with the fundamental sampling time $T_c = 0.1$ millisecond:

$$A_k = e^{AT_c}, \; B_k = \int_0^{T_c} e^{A\tau} d\tau B \tag{6.15}$$

In the discrete-time model, u_k is the current command and $y_{1,k}$ is the measurement from linear encoder. The input and the linear encoder measurement are updated at every T_c. $y_{2,k}$ is the measurement obtained from the image processing unit. Its sampling time is $T_s = 20T_c = 2$ milliseconds. The dual-rate ratio is $r = T_s/T_c = 20$. The time delay of $y_{2,k}$ is 3 millisecond. Thus, the number of delayed sample is calculated as $d = T_d/T_c = 30$. The measurement matrices are expressed as:

$$C_{1,k} = C_1 = \left[\frac{\omega^2}{M} \quad \frac{2\xi\omega}{M} \quad \frac{1+KM}{M} \quad 0 \quad 0 \right] \tag{6.16}$$

$$C_{2,k} = \begin{cases} C_2 = \begin{bmatrix} 0 & 0 & 0 & 0 & 1 \end{bmatrix} & \text{if } k = jr \\ [0] = \begin{bmatrix} 0 & 0 & 0 & 0 & 0 \end{bmatrix} & \text{if } k \neq jr \end{cases} \tag{6.17}$$

$$\delta_{2,k} = \begin{cases} 1 & \text{if } k = jr \\ 0 & \text{if } k \neq jr \end{cases} \tag{6.18}$$

where j is the integer number.

The covariance matrix of the process noise w_k is assumed to be a diagonal matrix for the sake of simplicity:

$$R_{w,k} = diag\left(\alpha_1, \alpha_2, \alpha_3, \alpha_4, \alpha_5\right) \tag{6.19}$$

The covariance matrices of the measurement noise $v_{1,k}$ and $v_{2,k}$ are expressed as follows considering the standard deviation of the linear encoder and the vision processing system:

$$R_{v1,k} = \sigma_{encoder} \tag{6.20}$$

$$R_{v2,k} = \sigma_{vision} \tag{6.21}$$

We can apply the upper-bound Kalman filter for a system with delayed and a non-delayed measurement which is proposed in Chapter 3. The algorithm is expressed as follows:

Initial condition:

$$\hat{x}_{0|0} = \begin{bmatrix} z_{1,0} & z_{2,0} & z_{3,0} & z_{4,0} & \Delta_0 \end{bmatrix}^T \tag{6.22}$$

$$\Omega_{0|0} = diag\left(\Omega_{11}, \Omega_{22}, \Omega_{33}, \Omega_{44}, \Omega_{55}\right) \tag{6.23}$$

Prediction:
- Predicted state:

$$\hat{x}_{k|k-1} = A_{k-1}\hat{x}_{k-1|k-1} + B_{k-1}u_{k-1} \tag{6.24}$$

- "Upper-bound" of the prediction error covariance:

$$\Omega_{k|k-1} = A_{k-1}\Omega_{k-1|k-1}A_{k-1}^T + R_{w,k-1} \tag{6.25}$$

Correction:
- Corrected state:

$$\hat{x}_{k|k} = \hat{x}_{k|k-1} + L_{1,k}\left(y_{1,k} - C_{1,k}\hat{x}_{k|k-1}\right) + L_{2,k}\left(y_{2,k} - C_{2,k}\hat{x}_{k-d|k-d-1}\right) \tag{6.26}$$

- Estimation gains:

$$\begin{bmatrix} L_{1,k} & L_{2,k} \end{bmatrix} = \bar{N}_k \bar{M}_k^{-1} \tag{6.27}$$

$$\bar{M}_k = \begin{bmatrix} C_{1,k}\left(\Omega_{k|k-1} + \mu_k Q_k\right)C_{1,k}^T + R_{v1,k} & C_{1,k}S_k\Omega_{k-d|k-d-1}C_{2,k}^T \\ C_{2,k}\Omega_{k-d|k-d-1}^T S_k^T C_{1,k}^T & \left(1+\dfrac{d}{\mu_k}\right)C_{2,k}\Omega_{k-d|k-d-1}C_{2,k}^T + \delta_{2,k}R_{v2,k}\delta_{2,k}^T \end{bmatrix} \tag{6.28}$$

$$\bar{N}_k = \begin{bmatrix} \left(\Omega_{k|k-1} + \mu_k Q_k\right)C_{1,k}^T & S_k\Omega_{k-d|k-d-1}C_{2,k}^T \end{bmatrix} \tag{6.29}$$

$$\Psi_{1,k-j} = A_{k-j}\left(I - L_{1,k-j}C_{1,k}\right) \tag{6.30}$$

$$S_k = \prod_{j=1}^{d} \Psi_{1,k-j} \tag{6.31}$$

$$Q_k = \sum_{i=0}^{d-1} \left[\left(\prod_{j=1}^{d-i-1} \Psi_{k-j} \right) A_{k-d+i} L_{2,k-d+i} C_{2,k} \Omega_{k-2d+i|k-2d-1+i} C_{2,k}^T L_{2,k-d+i}^T A_{k-d+i}^T \left(\prod_{j=1}^{d-i-1} \Psi_{k-j} \right)^T \right] \qquad (6.32)$$

- "Upper-bound" of correction error covariance:

$$\Omega_{k|k} = \Omega_{k|k-1} + \bar{L}_k \bar{M}_k \bar{L}_k^T - \bar{L}_k \bar{N}_k^T - \bar{N}_k \bar{L}_k^T + \mu_k Q_k \qquad (6.33)$$

In the above equations, μ_k is the tuning parameter which is assumed to be a constant in this study. Trial-and-error experiments are conducted to find the suitable value of μ_k. Notice that if μ_k is too small, the estimation gain associated with the vision measurement will be almost zero. Therefore, the vision information has little contribution to the estimated state. On the other hand, if μ_k is too big, the estimation will be unstable. The flow chart of the estimation algorithm is shown in Fig. 6.11.

6.5.2 Design of the position control

The position control loop is shown in Fig. 6.12 including a PID controller and the disturbance observer (DOB). The DOB is utilized to improving the robustness of the position control by rejecting the disturbance using the nominal model and the Q-filter. In this thesis, the nominal plant's transfer function is selected as:

$$P_{xn}(s) = \frac{1}{M_n s^2} \qquad (6.34)$$

where M_n is the nominal value of the equivalent mass.

The order of the Q-filter must be equal or higher than the order of the nominal plant. Thus, in this thesis the second order Q-filter is designed to satisfy the robust stability. The transfer function of the Q-filter is expressed as:

$$Q(s) = \frac{1}{1 + \dfrac{s}{q\omega_n} + \left(\dfrac{s}{\omega_n} \right)^2} \qquad (6.35)$$

where q is the quality factor and ω_n is the undamped natural frequency.

The real plant in (6.1) can be represented by the nominal plant and the boundary function $\Delta(s)$ as follows:

$$P_x(s) = P_{xn}(s) \left[1 + \Delta(s) \right] \qquad (6.36)$$

By using the Bode diagram, the quality factor and the undamped natural frequency is designed such that the following stability condition is satisfied for all frequency:

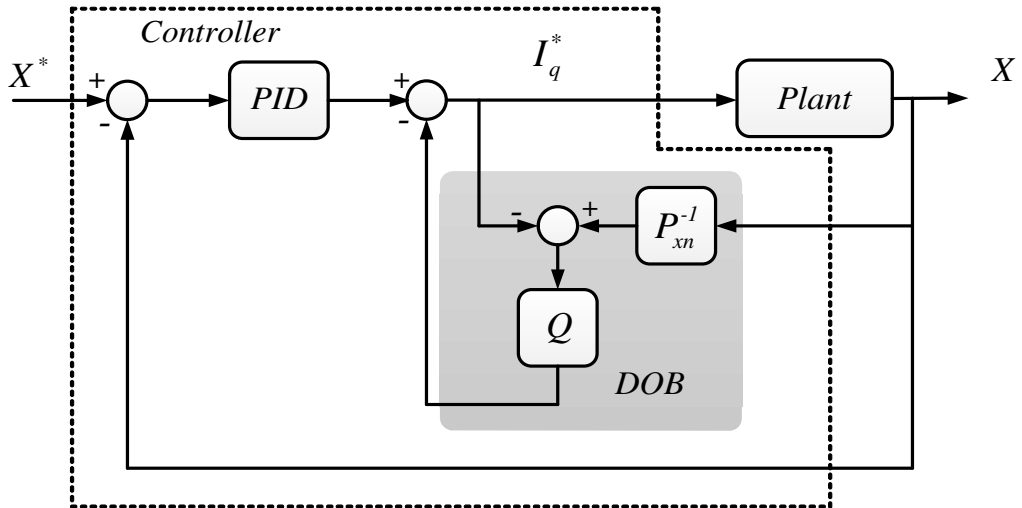$$|Q(j\omega)| < \frac{1}{|\Delta(j\omega)|} \qquad (6.37)$$

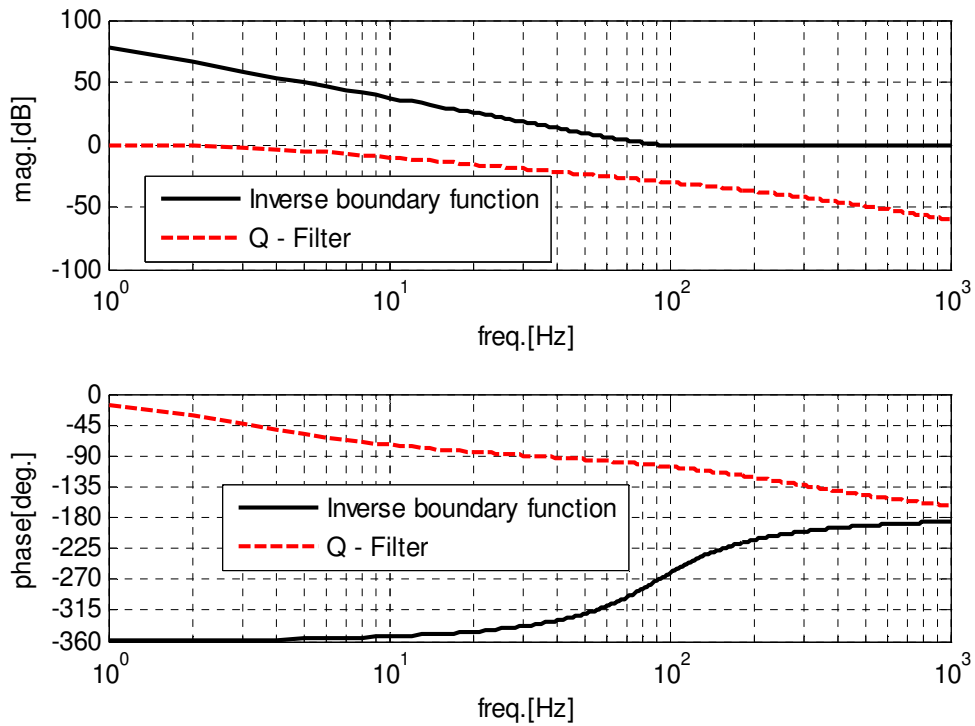Fig. 6.12 Position control loop based on PID and DOB.

Fig. 6.13 Bode diagram for Q-filter design.

In this thesis, Q-filter is designed with $q = 0.1$ and $\omega_n = 200$ [rad/s]. The Bode diagram of Q-filter and the inverse boundary function are shown in Fig. 6.13. The PID is designed by pole placement. If the inner loop including the real plant and the DOB can be approximately the nominal plant in (6.34), the PID gains can be calculated as follows:

$$\begin{cases} K_p = M_n \left(s_1 s_2 + s_2 s_3 + s_3 s_1 \right) \\ \qquad K_i = -M_n s_1 s_2 s_3 \\ \quad K_d = -M_n \left(s_1 + s_2 + s_3 \right) \end{cases} \tag{6.38}$$

where s_1, s_2, and s_3 are the desired poles of the close-loop.

6.6 Experimental results

6.6.1 Results of target position estimation

The experiments are conducted as described in section 6.3. Three target position estimation methods are designed and performed for comparison:

- Standard Kalman filter: Using the state space model (6.12) ~ (6.14), the standard Kalman filter algorithm is implemented. The estimated states are obtained as follows:

+ Predicted state:

$$\hat{x}_{k|k-1} = A_{k-1}\hat{x}_{k-1|k-1} + B_{k-1}u_{k-1} \tag{6.39}$$

+ Corrected state:

$$\hat{x}_{k|k} = \hat{x}_{k|k-1} + L_{1,k}\left(y_{1,k} - C_{1,k}\hat{x}_{k|k-1} \right) + L_{2,k}\left(y_{2,k} - C_{2,k}\hat{x}_{k|k-1} \right) \tag{6.40}$$

- Cascade estimation: As introduced in section 1.4 of the Chapter 1, this method has two stages, the Kalman filter and the d-step predictor. The configuration of the cascade estimation is shown in Fig. 6.14. In this configuration, the input and the non-delayed measurement y_1 are intentionally delayed and stored. In the first stage, the past time state $\hat{x}^*_{k-d|k-d}$ is estimated using the standard Kalman filter. In the second stage, the current state $\hat{x}^*_{k|k}$ is obtained through the d-step predictor using the dynamics model.

- Upper-bound Kalman filter: This is the proposed estimation method presented in the previous section.

Experimental results of three methods are shown in Fig. 6.15. Because the standard Kalman filter does not handle the delayed measurement, the estimation of the target position using this method is considerably inaccurate. Both the cascade estimation and the upper-bound Kalman filter can compensate the delayed measurement. However, the estimated target from the upper-bound Kalman filter is close to the true values than that of the cascade estimation (Fig. 6.16). As discussed in the Chapter 2, the inaccuracy of the cascade estimation can be explained by the influence of the model uncertainty to the d-step predictor in the cascade estimation.

Experimental results show the advances of the upper-bound Kalman filter in comparisons with other two methods. For this reason, we will use the upper-bound Kalman filter for providing the estimated target position in the visual servo control system in Fig. 6.10

6.6.2 Results of target tracking control

Target tracking control based on the proposed upper-bound Kalman filter is conducted as explained in section 6.3. The experimental results are shown in Fig. 6.17. By using the DOB based controller, the control system can suppress the vibration considerably. Therefore, the relative position between target and camera can quickly reach the desired value of zero. The final tracking error is less than 3µm which is the goal of this visual servo system.

6.7 Discussion

In this chapter, we introduce the basics of the chip mounting machine. A visual servo control system which is the key technology of the chip mounting is designed and tested. To compensate the large-time-delay and improve the update rate of the image processing unit, the upper-bound Kalman filter is utilized to estimate the target position. The control system includes the upper-bound Kalman filter and the position control loop based on PID and DOB. Experiments are performed to evaluate the effectiveness of the proposed control system. Experimental results show that the upper-bound Kalman filter is more accurate than the standard Kalman filter and the cascade estimation. The target tracking accuracy less than 3µm is successfully attained using the proposed control system.
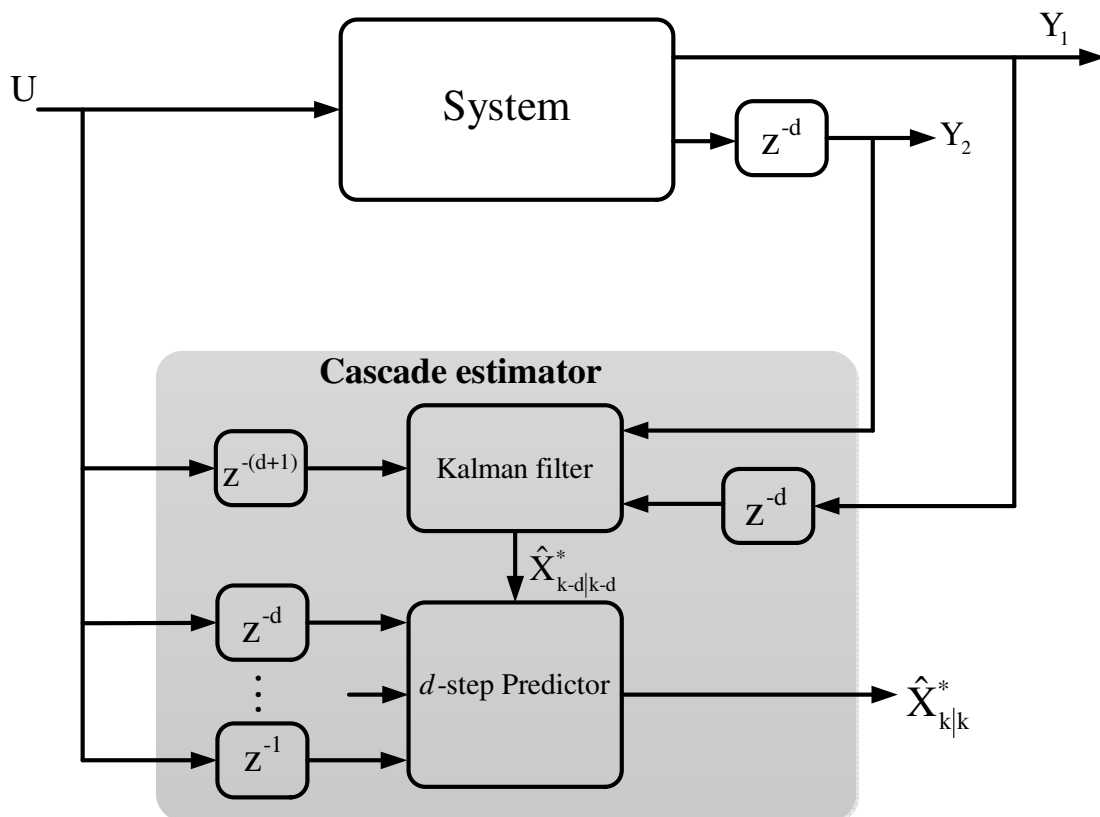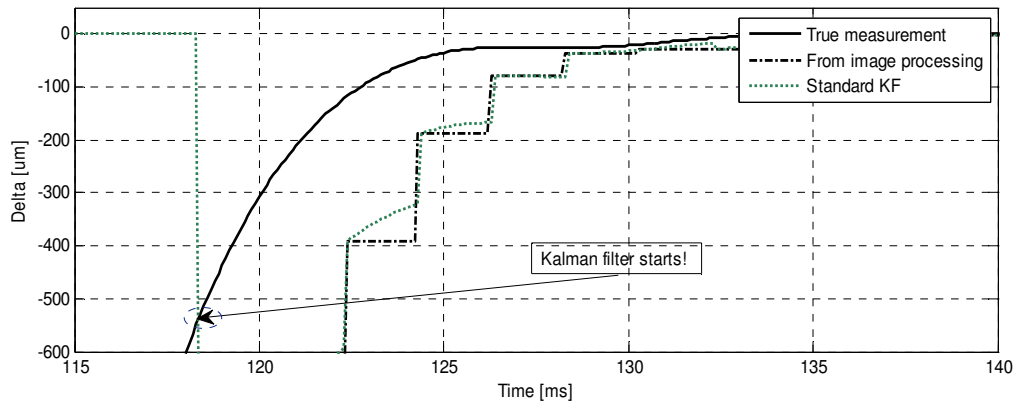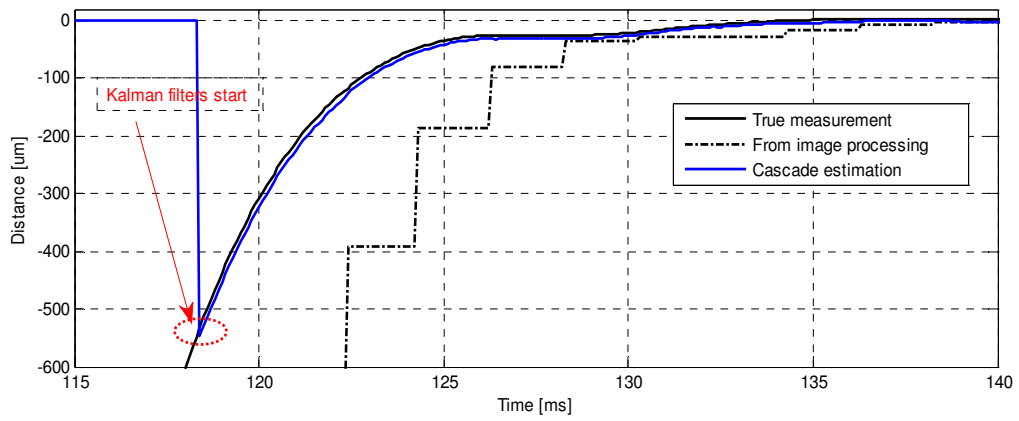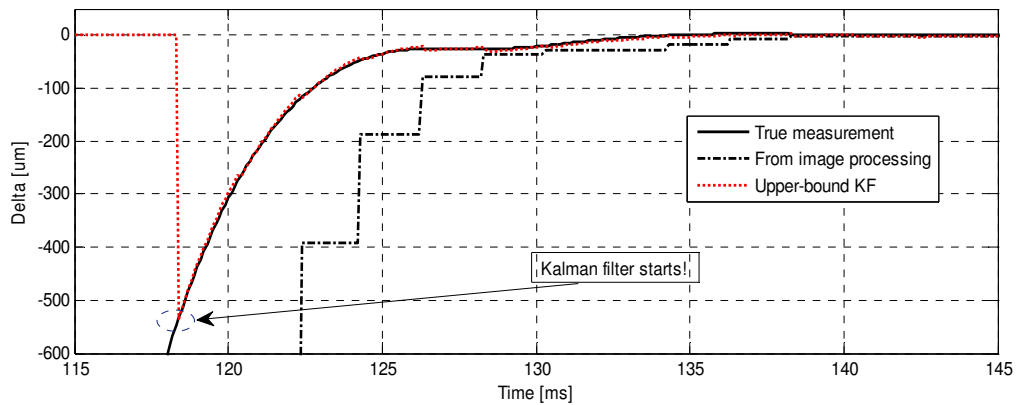

Fig. 6.14 Cascade estimation of the target position.

(a)   Target position estimation using standard Kalman filter.

(b)   Target position estimation using cascade estimation.

(c)   Target position estimation using upper-bound Kalman filter.

Fig. 6. 15 Experimental results of target position estimation by different methods.
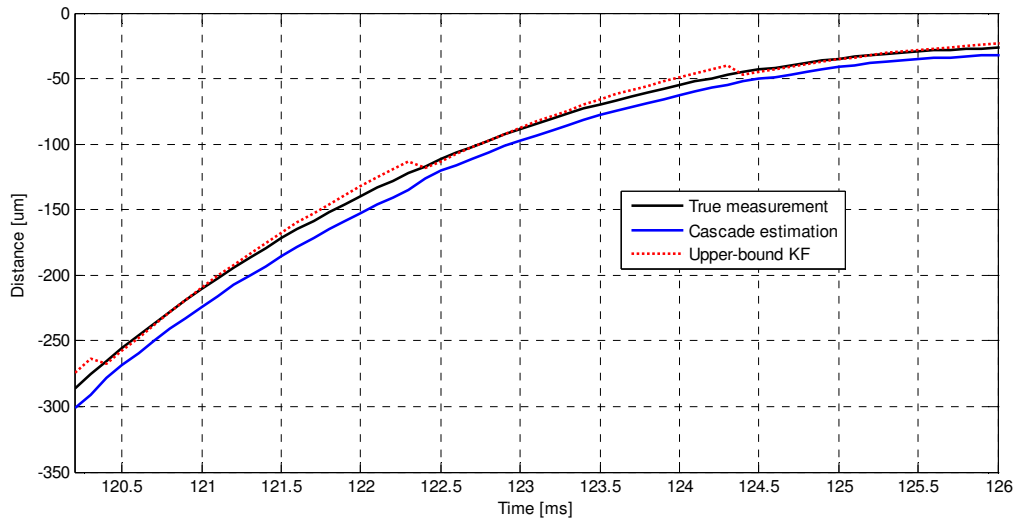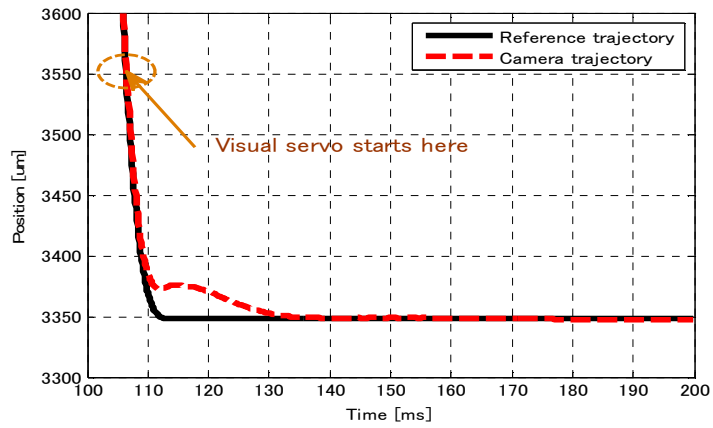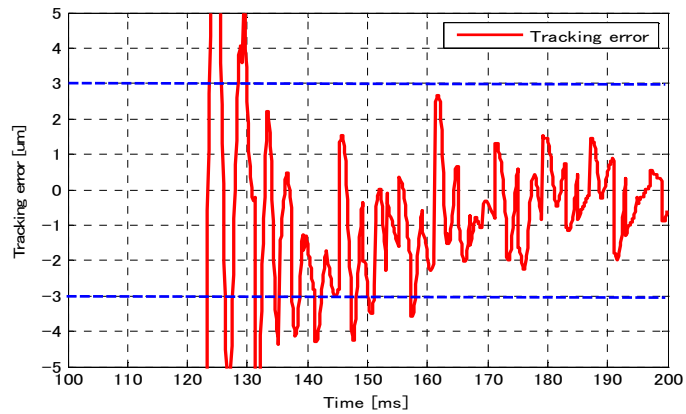
Fig. 6.16 Performance of the upper-bound KF and the cascade estimation.

(a)   Trajectory

(b)   Tracking error

Fig. 6. 17 Experimental results of target tracking control.

Chapter 7:

Estimation of Cornering Stiffness and Sideslip Angle

"We need something more than mere theory and preaching now, though·"

Sherlock Holmes (A Study in Scarlet)

7.1 Introduction

In this chapter, we will study the application of unscented Kalman filter (UKF) for state and parameter estimation. The goal of this study is to verify that if the UKF can be used to simultaneously estimate the state and parameter instead of the conventional adaptive estimator with RLS identification. The case of study is presented as follows.

As introduced in Chapter 5, it is essential to control the sideslip angle of a vehicle to stabilize its lateral motion. Besides that, the understanding of tire cornering stiffness is also important. Online estimation of tire cornering stiffness can be used for adaptive lateral motion control, tire force distribution, or range extension control [69]. In Chapter 5, a robust estimation of sideslip angle using GPS is proposed. Thanks to the disturbance accommodation Kalman filter, the accurate estimation is maintained while using the constant nominal values of the tire cornering stiffness. In this chapter, sideslip angle estimation is studied from another point of view, adaptive estimation instead of robust estimation.

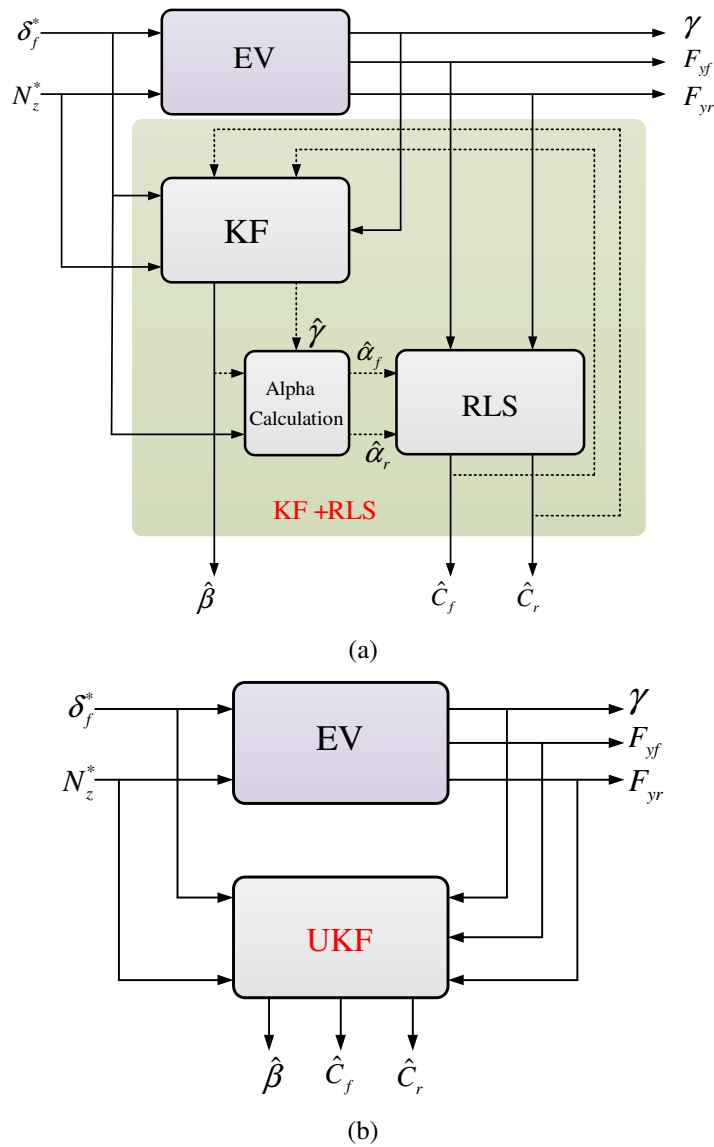Fig. 7.1 The hub-bearing unit produced by NSK Ltd.

(a)

(b)

Fig. 7.2 Sideslip angle and cornering stiffness estimation:

a) Kalman filter + RLS Identification, b) Unscented Kalman filter.

The key sensors for this estimation are the tire-lateral force sensors. Fig. 7.1 shows a novel tire-lateral force sensor which is designed as a hub-bearing-unit by NSK Ltd. In [78], based on the difference between the left and right side tire lateral forces, the sideslip angle is obtained through RLS identification. However, this conventional RLS algorithm is just suitable for estimating the "parameter" which is supposed to change slightly. Unluckily, the sideslip angle is a time-varying variable which can vary sharply and quickly according to the operation of the vehicle. If the dynamics model is neglected and only the measurement based RLS algorithm is used, the stable estimation is not assured. Moreover, this RLS algorithm cannot be utilized if the time delay or data missing is found in the force sensor measurements.

In this chapter, two schemes for estimating the sideslip angle and the cornering stiffness using tire lateral force sensors are proposed and compared.

- Method 1: Adaptive estimation - The Kalman filter with a RLS identification of cornering stiffness (KF + RLS).
- Method 2: Simultaneous estimation based on the unscented Kalman filter (UKF).

7.2 Estimation design

The two estimation configurations are shown in Fig. 7.2. The inputs are the front steering angle and the yaw moment, while the output measurements including the yaw-rate and the lateral tire forces.

7.2.1 Adaptive estimation using KF + RLS

The estimator includes three main blocks:

Kalman filter:

The Kalman filter is based on the linear bicycle model presented in Chapter 5. The output measurement of the Kalman filter is the yaw-rate sensor.

Tire slip angle calculator:

Using the estimated sideslip angle and yaw-rate from the Kalman filter, the tire slip angles are computed as follows:

$$\hat{\alpha}_f = \hat{\beta} + \frac{l_f}{v_x}\hat{\gamma} - \hat{\delta}_f \tag{7.1}$$

$$\hat{\alpha}_r = \hat{\beta} - \frac{l_r}{v_x}\hat{\gamma} \tag{7.2}$$

Cornering stiffness identification:

The general front and rear lateral forces (F_{yf} and F_{yr}) are calculated from the tire-force sensor as follows:

$$F_{yf} = F_{y\_fl} + F_{y\_fr} \tag{7.3}$$
$$F_{yr} = F_{y\_rl} + F_{y\_rr} \tag{7.4}$$

where F_{y_fl}, F_{y_fr}, F_{y_rl}, and F_{y_rr} are the lateral force at each wheels: front-left, front-right, rear-left, and rear-right, respectively.

The front and rear cornering stiffness are identified using the following equations:

$$y_k = \varphi_k^T \theta_k \tag{7.5}$$

where

$$y_k = \begin{bmatrix} F_{yf} \\ F_{yr} \end{bmatrix}, \quad \varphi_k^T = \begin{bmatrix} -2\hat{\alpha}_{f,k} & 0 \\ 0 & -2\hat{\alpha}_{r,k} \end{bmatrix}, \quad \theta_k = \begin{bmatrix} C_f \\ C_r \end{bmatrix} \tag{7.6}$$

The RLS algorithm is expressed as follows with the forgetting-factor λ.

$$\hat{\theta}_k = \hat{\theta}_{k-1} + L_k \left(y_k - \varphi_k^T \hat{\theta}_{k-1} \right) \tag{7.7}$$

$$L_k = P_{k-1}\varphi_k \left(\lambda I + \varphi_k^T P_{k-1}\varphi_k \right)^{-1} \tag{7.8}$$

$$P_k = \frac{1}{\lambda}\left(I - L_k \varphi_k^T \right)P_{k-1} \tag{7.9}$$

7.2.2 Simultaneous estimation using UKF

From the linear bicycle model presented in Part B, the following equations are written:

Dynamic equations (the cornering stiffness is assumed to be a random-walk).

$$\dot{\beta} = \frac{-2\left(C_f + C_r\right)}{mv_x}\beta + \left[-1 - \frac{2\left(C_f l_f - C_r l_r\right)}{mv_x^2}\right]\gamma + \frac{2C_f}{mv_x}\delta_f \tag{7.10}$$

$$\dot{\gamma} = \frac{-2\left(C_f l_f - C_r l_r\right)}{I_z}\beta + \frac{-2\left(C_f l_f^2 + C_r l_r^2\right)}{I_z v_x}\gamma + \frac{2C_f l_f}{I_z}\delta_f + \frac{1}{I_z}N_z \tag{7.11}$$

$$\dot{C}_f = 0 \tag{7.12}$$

$$\dot{C}_r = 0 \tag{7.13}$$

Measurement equation:

$$\gamma = \gamma \tag{7.14}$$

$$F_{yf} = -2C_f \left(\beta + \frac{l_f}{v_x}\gamma - \delta_f \right) \tag{7.15}$$

$$F_{yr} = -2C_r \left(\beta - \frac{l_r}{v_x}\gamma \right) \tag{7.16}$$

From (7.10) ~ (7.16), a discrete-time nonlinear stochastic model is established with the fundamental sampling time of 1 millisecond:

$$\begin{cases} x_{k+1} = f\left(x_k, u_k\right) + w_k \\ y_k = h\left(x_k, u_k\right) + v_k \end{cases} \tag{7.17}$$

$$x_k = \begin{bmatrix} \beta_k & \gamma_k & C_{f,k} & C_{r,k} \end{bmatrix}^T, \; u_k = \begin{bmatrix} \delta_{f,k} & N_{z,k} \end{bmatrix}^T, \; y_k = \begin{bmatrix} \gamma_k & F_{yf,k} & F_{yr,k} \end{bmatrix}^T \tag{7.18}$$

where $f(x_k, u_k)$ and $h(x_k, u_k)$ are nonlinear functions, x_k is the state vector, u_k is the input vector, y_k is the measurement vector, w_k and v_k are Gaussian noises with zero means and covariance $R_{w,k}$ and $R_{v,k}$, respectively.

Using the nonlinear model (7.17), the UKF algorithm is applied to estimate the sideslip angle and the cornering stiffness simultaneously.
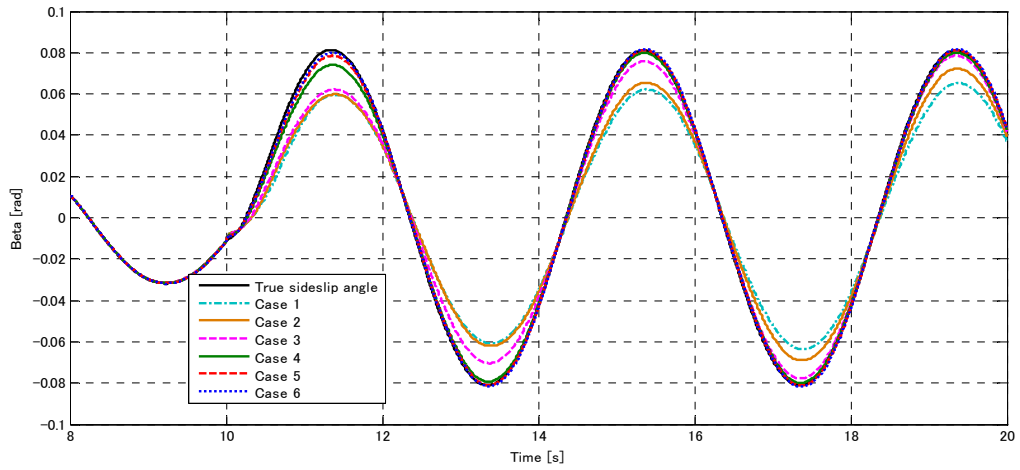
(a)
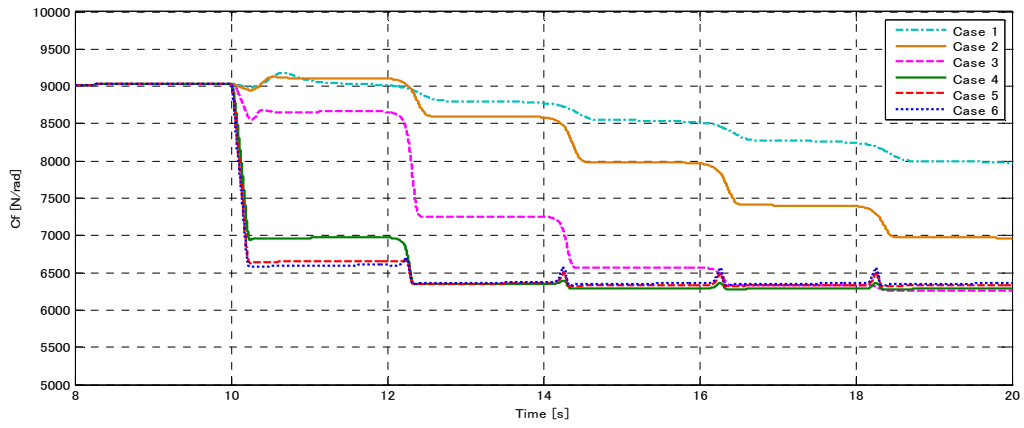
(b)
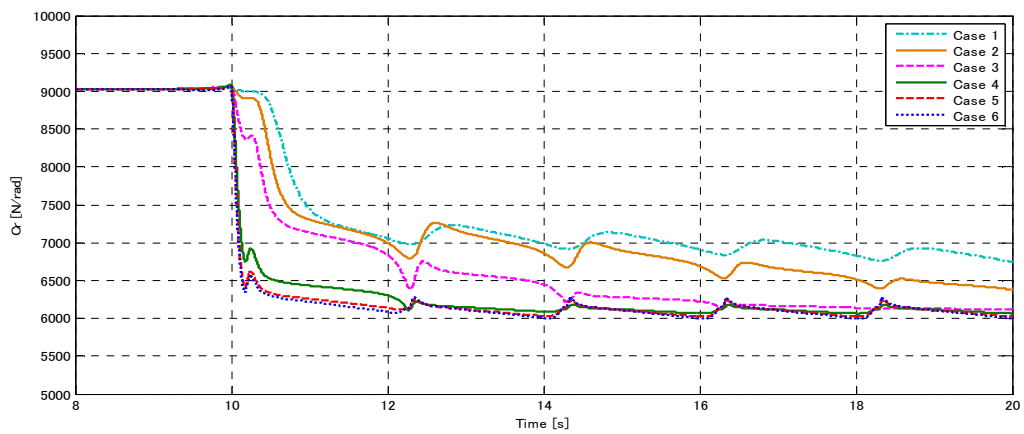
(c)

Fig. 7.3. Simulation results of the UKF at different tuning parameters:

a) Sideslip angle, b) front cornering stiffness, c) rear cornering stiffness.
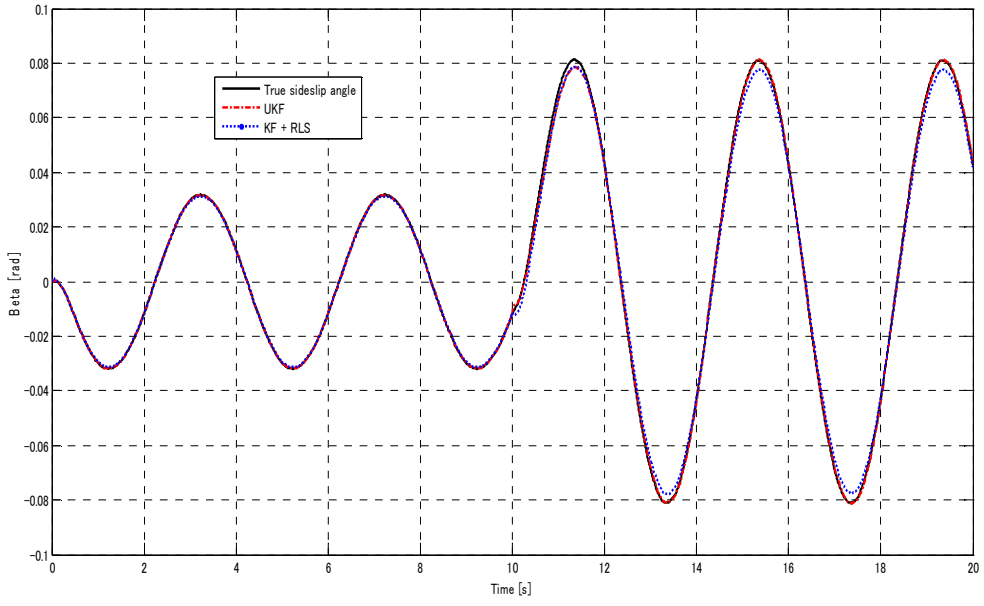
(a)
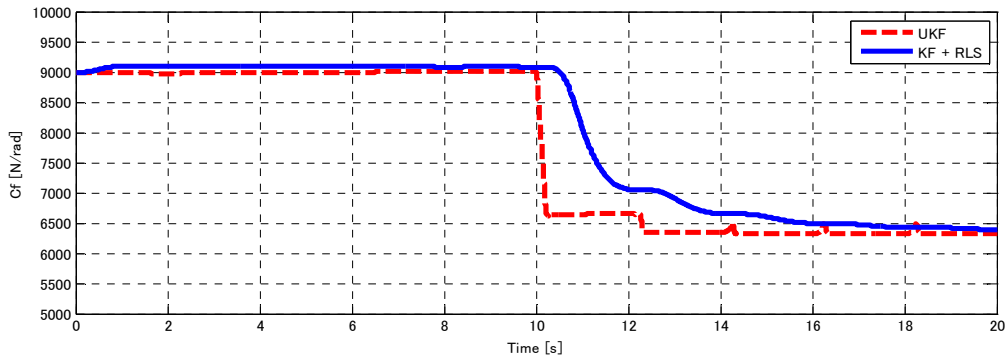
(b)
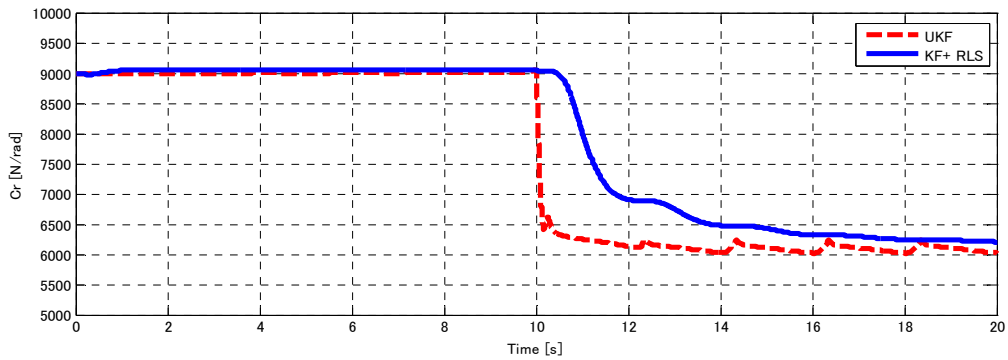
(c)

Fig. 7.4 Simulation results of UKF and KF + RLS ($\lambda = 0.9997$):

a) Sideslip angle, b) front cornering stiffness, c) rear cornering stiffness.

(a)

(b)

(c)

Fig. 7.5 Simulation results of UKF and KF + RLS (λ= 0.998):

a) Sideslip angle, b) front cornering stiffness, c) rear cornering stiffness.
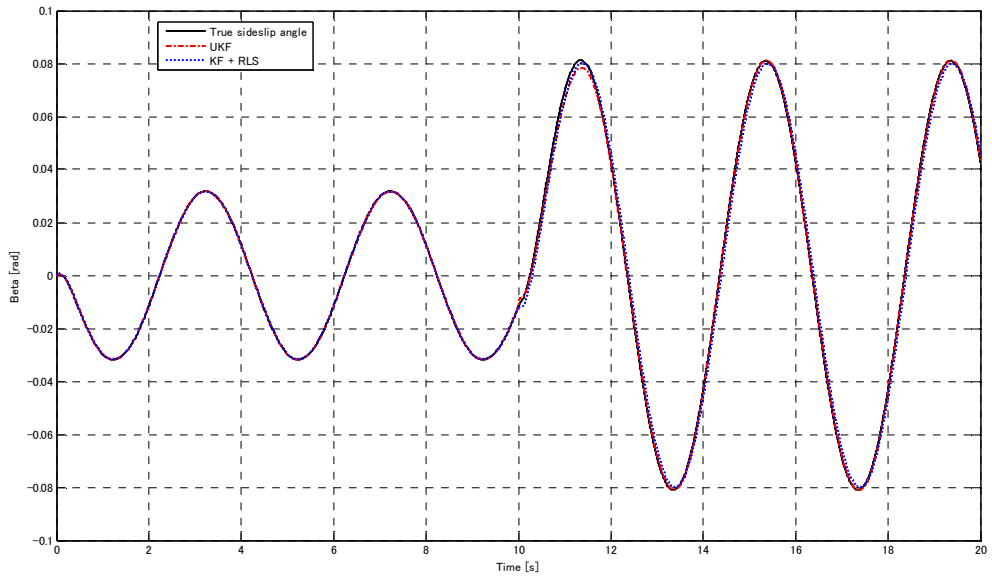
(a)
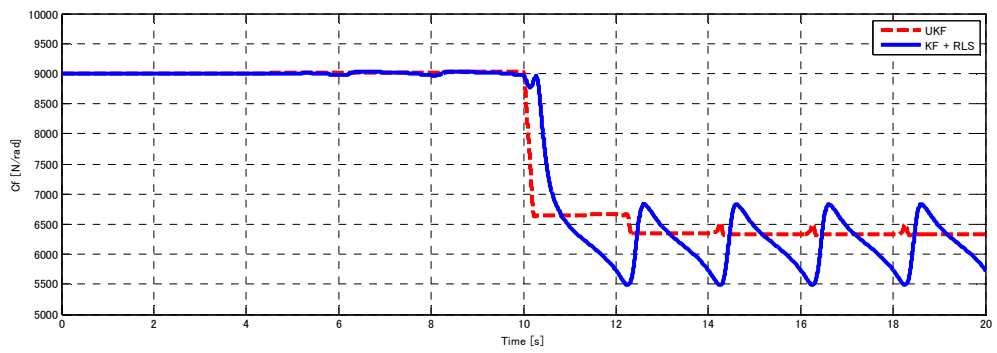
(b)
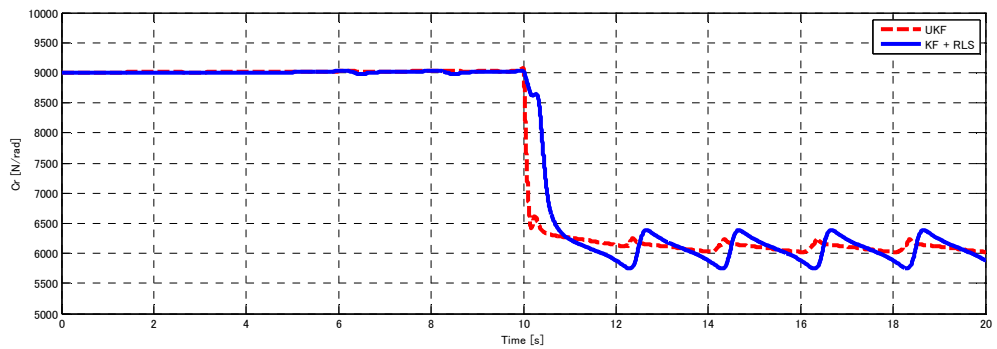
(c)

Fig. 7.6 Simulation results of UKF and KF + RLS (λ= 0.995):
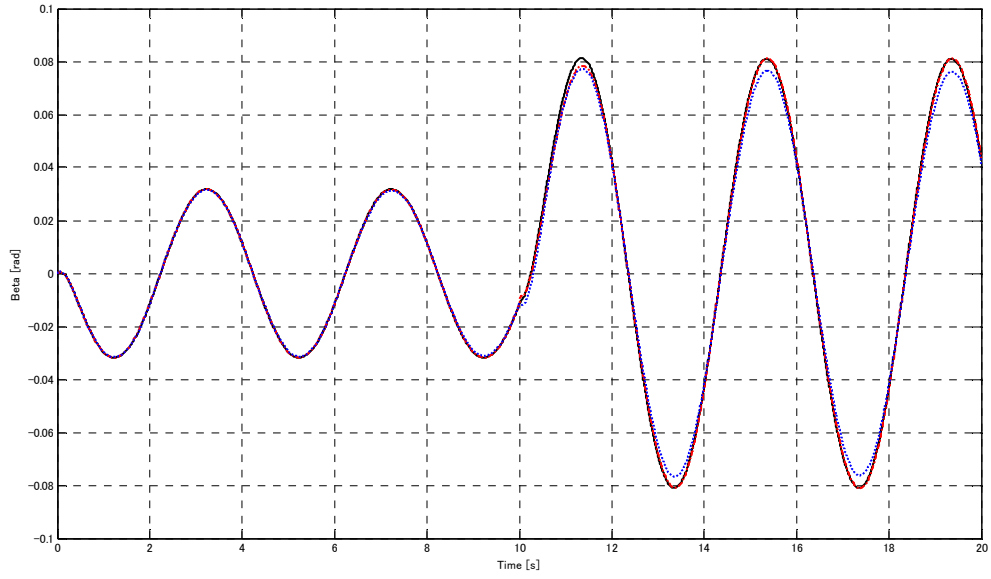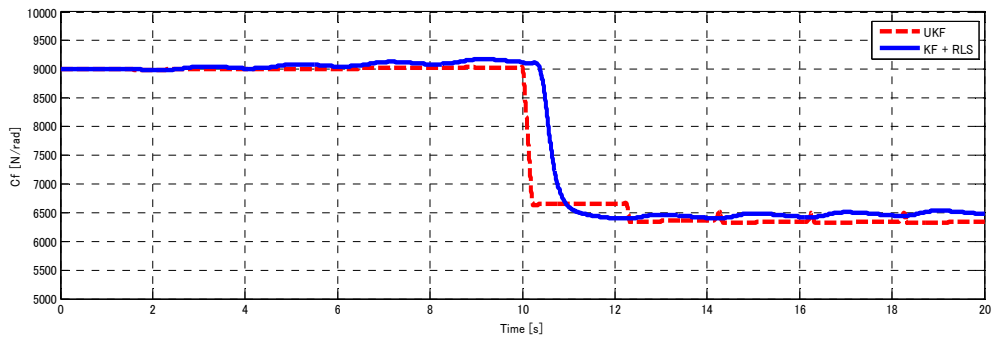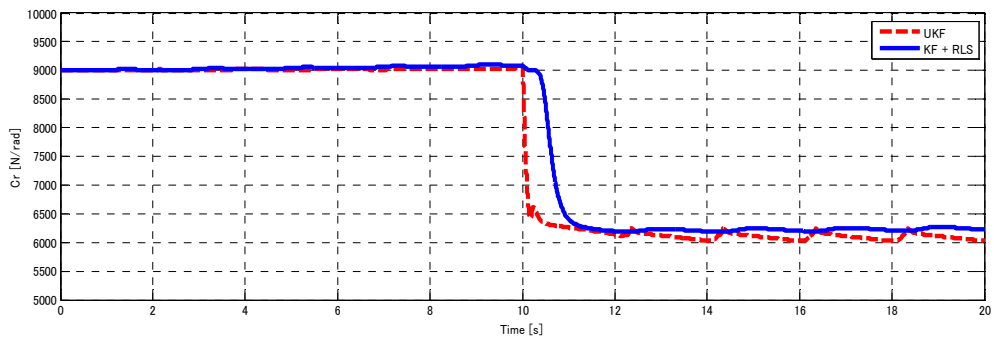
a) Sideslip angle, b) front cornering stiffness, c) rear cornering stiffness.
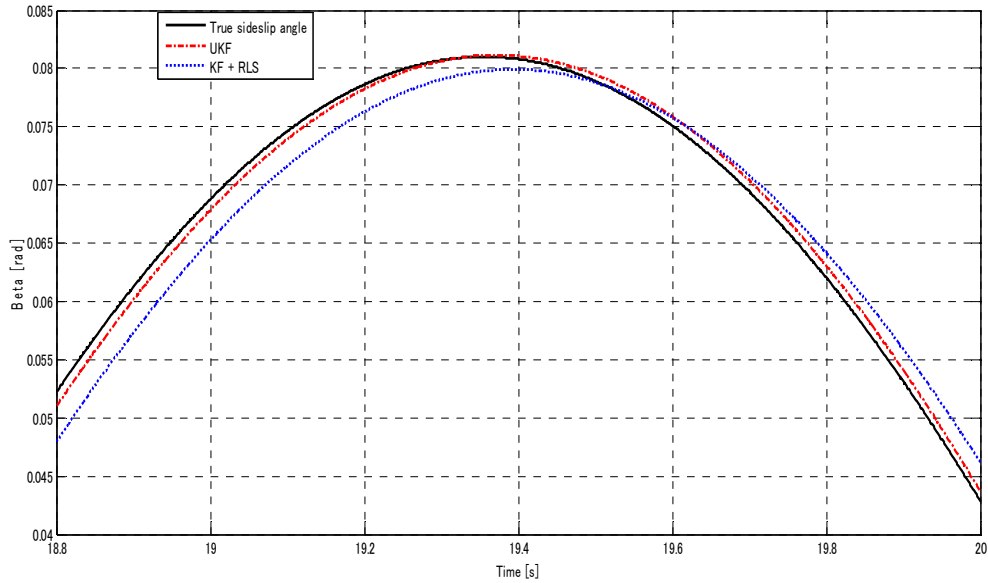
Fig. 7.7 Sideslip angle estimation by UKF and KF + RLS ($\lambda = 0.995$).

7.3 Simulation results

Simulations conditions:

- The vehicle model is based on the experimental vehicle COMS in Chapter 5.
- The vehicle runs in the slalom-test with sinusoidal steering angle at the speed of 25 kph.
- The initial values of the cornering stiffness in the estimation models are $C_f(0) = C_r(0) = 9000$ [N/rad]. From the beginning, the vehicle runs on the high friction road such that the true cornering stiffness is set the same as the initial values. *Since 10 second*, the vehicle enters the slippery road where the cornering stiffness is set as $C_f = 6400$ [N/rad], $C_r = 6000$ [N/rad]. This means a sharp change of the tire characteristics is simulated.
- The covariance matrices of the process and measurement noises are assumed to be diagonal. The sets of tuning parameter of two estimation model are as follows:

$$KF + RLS: R_{w,KF} = diag\left(\varepsilon_{11}, \varepsilon_{22}\right), \ R_{v,KF} = \sigma_{gyro}, \ \lambda_{RLS} \tag{7.19}$$

$$UKF: R_{w,UKF} = diag\left(\rho_{11}, \rho_{22}, \rho_{33}, \rho_{44}\right), \ R_{v,UKF} = diag\left(\sigma_{gyro}, \sigma_{F_{yf}}, \sigma_{F_{yr}}\right) \tag{7.20}$$

where $\sigma_{gyro}, \sigma_{F_{yf}}$, and $\sigma_{F_{yr}}$ are the covariance values of the Gaussian noises associating with the yaw-rate measurement, front and rear tire force measurements.

Tuning of the UKF:

In the set of tuning parameters of the UKF, $\sigma_{F_{yf}}, \sigma_{F_{yr}}$ and σ_{gyro} depend on the noise levels of the yaw-rate sensor and the tire force sensors. The values of ρ_{11} and ρ_{22} are obtained through the noise associated with the input to the bicycle model. For the sake of simplicity, it is assumed that the covariance of these measurement noise and process noises are constant. Therefore, it is only essential to tune the values of ρ_{33} and ρ_{44} which associate with the dynamics of the cornering stiffness. Six cases of the pair (ρ_{33}, ρ_{44}) are performed:

- Case 1: $(\rho_{33}, \rho_{44}) = (1, 4)$
- Case 2: $(\rho_{33}, \rho_{44}) = (10, 40)$
- Case 3: $(\rho_{33}, \rho_{44}) = (100, 400)$
- Case 4: $(\rho_{33}, \rho_{44}) = (1000, 4000)$
- Case 5: $(\rho_{33}, \rho_{44}) = (2000, 8000)$
- Case 6: $(\rho_{33}, \rho_{44}) = (2500, 10000)$

The simulation results of UKF tuning are shown in Fig. 7.3. In case 1, after entering the low friction road, the estimated values of the cornering stiffness converge very slowly to the true values. Therefore, the estimated sideslip angle of case 1 is very inaccurate. In case 2, because (ρ_{33}, ρ_{44}) is bigger than that of case 1, the speed of convergence of the estimated cornering stiffness is increased. This explains the more accurate sideslip angle estimation of case 2. Again, from case 3 to case 6, as the pair (ρ_{33}, ρ_{44}) is increased, the convergence of the tire cornering stiffness estimation becomes better and better.

Comparing the UKF with the KF + RLS:

The UKF with the pair $(\rho_{33}, \rho_{44}) = (2000, 8000)$ is compared with the KF + RLS. To make the fair comparison, we will find the optimal tuning parameters of the KF + RLS. Notice that $\varepsilon_{11}, \varepsilon_{22}$ and σ_{gyro} depend on the process noises of the bicycle model and the measurement noise of the yaw-rate sensor. For the sake of simplicity, we can assume that they are constant as in the UKF algorithm. The forgetting factor of the KF + RLS is tuned and the following cases are demonstrated:

- Case 1: $\lambda_{RLS} = 0.9997$
- Case 2: $\lambda_{RLS} = 0.998$
- Case 3: $\lambda_{RLS} = 0.995$

The simulation results of Case 1, Case 2, and Case 3 are presented in Fig. 7.4, Fig. 7.5, and Fig. 7.6, respectively.

Case 1: From the beginning, the UKF and the KF + RLS have the same estimation performance. When the vehicle suddenly enters the slippery road, the estimates from the UKF quickly converge to their true values with little errors. As the forgetting factor of the KF + RLS is too close to 1.0, the cornering stiffness identification is too slow, and the sideslip angle estimation of the KF + RLS is less accurate than that of the UKF.

Case 2: The forgetting factor is reduced to 0.998. Consequently, the cornering stiffness

identification is faster than in Case 1. However, the UKF still attains smaller estimation errors in comparison with the KF + RLS.

Case 3: The forgetting factor is even reduced to 0.995. The cornering stiffness identification of the KF + RLS is much faster than that in Case 1. It seems to be the best selection of the tuning forgetting factor for the KF + RLS. However, the trade-off occurs as the fluctuation of the identified cornering stiffness is found. If the forgetting factor is even smaller than 0.995, the fluctuation of the cornering stiffness identification is even worse and the sideslip angle estimation is considerably degraded.

Case 3 seems to be the limitation that the forgetting factor should not be reduced anymore. Comparing the KF + RLS at $\lambda_{RLS} = 0.995$ with the UKF at $(\rho_{33}, \rho_{44}) = (2000, 8000)$, the sideslip angle estimations of two methods are almost the same. If we plot a part of the simulation data in the steady status, the UKF still achieves the better tracking to the true sideslip angle (Fig. 7.7).

From the above simulation results, we can conclude that:

- The UKF has the simpler estimation structure.
- The UKF is more flexible to design than the KF + RLS because its set of tuning parameter is bigger ((ρ_{33}, ρ_{44}) v.s λ_{RLS}).
- The UKF provide better estimations of sideslip angle and cornering stiffness. Especially, the convergence of the cornering stiffness from the UKF is very quick. Tuning the forgetting factor of the KF + RLS over the range $[0.995 \leq \lambda_{RLS} \leq 0.9997]$, we can always tune the UKF such that it achieves the better performance than the KF + RLS.
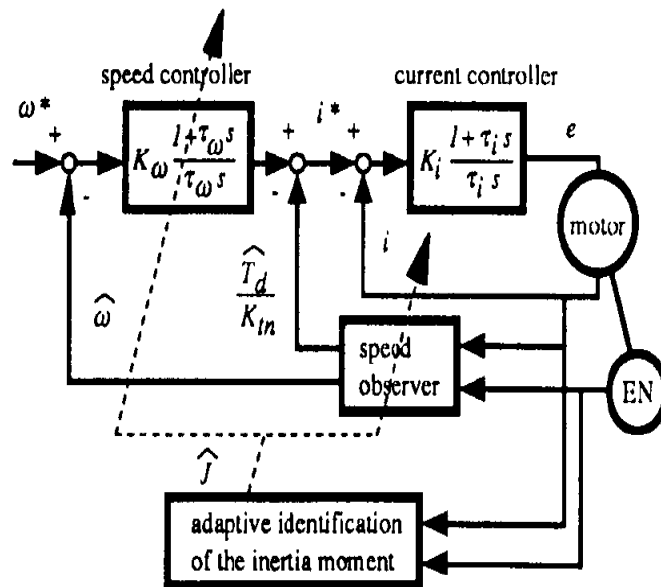
Fig. 7.8 Hori's adaptive servomotor control system (from [106]).

7.4 Discussion

In this chapter, a new configuration for sideslip angle and cornering stiffness estimation is proposed. It does not require a Kalman filter and RLS identification. There is only one unscented Kalman filter to estimate the sideslip angle and cornering stiffness simultaneously. Thanks to its quick convergence and simple estimation design, this estimation scheme can be developed for other motion control application in which state estimation and parameter adaptation are desirable.

For instance, in [106], Hori proposed the adaptive servomotor control system utilizing the low precision shaft encoder. As shown in Fig. 7. 8, the instantaneous speed observer is used to estimate the motor rotational speed at every control period. The inertia moment is obtained separately through the RLS identification to update the speed observer and the controller. In such kind of motion control system, we may think about the proposed state-parameter estimation based on UKF.

Certainly, other cases of study and experiments should be conducted to answer the question: should we separate or combine the estimation of the state and the parameter. This chapter is only the very first step to this question.

Chapter 8:
Conclusion

"A conclusion is simply the place where you got tired of thinking."
Dan Chaon (Stay Awake)

8.1 Contributions of this study

From the side of Kalman filter and estimation theory, this thesis has three contributions:

1) By using the disturbance accommodation, it is possible to enhance the robustness and the accuracy of dual-rate estimation using Kalman filter. Through both simulations and experiments, the disturbance accommodation dual-rate Kalman filter is shown to be more robust than the conventional dual-rate estimation or innovation-handling dual-rate estimation.

2) By using the upper-bound of estimation error covariance, a new Kalman filter that can handle the large-time-delay measurement is proposed. The upper-bound Kalman filter has two main advantages: First, it does not increase the dimension of the system. Second, with the μ-gain, it is more flexible to design the estimation gain and the robustness of the algorithm is improved. By simulations and experiments, the upper-bound Kalman filter is proved to be more accurate and stable than other delay-compensation-estimation methods, such as the cascade estimation and measurement extrapolation Kalman filter.

3) By using the unscented Kalman filter (UKF), adaptive state estimation is suggested to be designed simply instead of combining the state estimation with parameter identification. Moreover, the accuracy and the convergence of the new algorithm can be effectively improved.

Three applications are developed and verified using the above theories:

1) Electric vehicle motion control system using GPS: In this system, the sampling time of the GPS measurements are multiples of the actuator control periods. Thus, the disturbance accommodation Kalman filter is applied for accurately estimating the states which is fed back to the motion controllers. Three motions variables are estimated: sideslip angle, yaw angle, and longitudinal velocity. Three motion controls are demonstrated: lateral stability control, autonomous attitude control, and wheel slip-ratio control.

2) Visual servo control for chip-mounting system: In this system, the target's position is detected through the FPGA based image processing unit. However, the vision measurement is delayed and the delay time is equal to 30 times of the control period of the linear servo drive. The upper-bound Kalman filter is utilized in this case to estimate the target position accurately for target tracking control.

3) Simultaneous estimation of sideslip angle and cornering stiffness using tire force sensors: The conventional estimation scheme is the combination of the Kalman filter and the RLS identification. By using the UKF, the estimation algorithm is simpler, but better estimation performance is achieved.

8.2 Limitations of this study

In Chapter 2, besides the disturbance accommodation, the robust issue of the dual-rate estimation is also examined thorough another point of view: design of the robust filter parameters ($\Delta A_{e,k}$ and $L_{e,k}$) considering the upper-bound of the estimation error covariance. However, we have not decided the applications and performed experimental verifications for this method. Moreover, we only study the case that the dual-rate ratio is a constant.

In Chapter 3, the μ-gain is introduced to obtain the estimation gain of the upper-bound Kalman filter for handling the measurement with large time delay. However, the μ-gain is obtained by trial-and-error test and it is designed in advance. What is the optimal μ-gain and how to tune it in on-line experiment is a nontrivial question to solve. The delayed-time is assumed to be constant in this thesis. Therefore, it is desirable to evaluate the upper-bound Kalman filter with random-time-delay.

In all the Kalman filter algorithms proposed in this thesis, the covariance matrices of the process noises and measurement noises are kept constant. The on-line tuning of noise covariance matrices is not studied in this thesis.

In Chapter 5, the experiments of electric vehicle motion control are not conducted at high speed due to the limitation of the maximum speed at the test course in our university campus. In Chapter 6, the visual servo is only conducted in case the target is fixed. Actually, in our joint-research project, the chip mounting machine is designed such that the target position if fixed. However, the time-delay compensation Kalman filter proposed in this thesis could be applied in the general case that the target is moved. In this case, the position, the velocity and the acceleration should be added into the modelling of the visual servo system.

8.3 Kalman filter and model predictive control

Model predictive control (MPC) is a type of optimal control which has been developed for decades [111], [112], [113]. Visual servo based on MPC was proposed in [117], [118]. Unlike PID or LQR controller, MPC has the ability to anticipate the future events. MPC can enable the shorter development time in comparison with PID or LQR. It can handle the constraints and the designed is explicit thanks to the straightforward formulation.

In MPC, it is essential to minimize the objective function with the respect to the future control vectors considering some constraints:

$$J_k = \sum_{i=1}^{L}\left[\left(y_{k+i} - r_{k+i}\right)^T Q_i \left(y_{k+i} - r_{k+i}\right) + u_{k+i-1}^T P_i u_{k+i-1} + \Delta u_{k+i-1}^T R_i \Delta u_{k+i-1}\right] \tag{8.1}$$

where L is the prediction horizon, Q_i, P_i, R_i are symmetric and positive demi-definite weighting matrices specified by the designer.

Although they have different purposes, the Kalman filter and the MPC share the background that both of them consists of an objective function to minimize, and a prediction model which is based on the dynamics of the system. The upper-bound Kalman filter proposed in Chapter 3 is based on the minimization of the cost function considering a certain horizontal interval defined by the delay time. This horizontal interval is used to taken into account the past covariance, while in the MPC, the horizontal interval is to predict the future.

Literature review shows that Kalman filter has a tight relationship with MPC. In order to realize the prediction model, it is important to know the states of the system. If the state x_k is not measured, Kalman filter could be utilized. Various researches that combining the Kalman filter and MPC can be found, such as in [114], [115], [116]. The proposed Kalman filter in this thesis could be applied to MPC to overcome the dual-rate and time-delay problem. Moreover, the main disadvantage of MPC is that it relies on the model. In Chapter 4, we propose the UKF based simultaneous estimation of system state and parameter. This method can be a solution to improve the robustness of MPC.

8.4 Future works

In future works we will study the following issues in theory side:

1) Experimental verification of the robust dual-rate filter considering the upper-bound of estimation error covariance.

2) On-line optimization of the μ-gain in the upper-bound Kalman filter for handing delayed measurement.

3) Develop the upper-bound Kalman filter for the random-time-delay case.

4) Examine the on-line tuning of the process and measurement noise covariance matrices.

5) Examine the possibility of the proposed Kalman filter in this thesis to the MPC system.

Think about the applications, we will try to expand and apply the Kalman filters designed in this thesis to other motion control applications. From our opinion, the unscented Kalman filter (UKF) may contribute a new scheme for adaptive estimation and motion control. In any system such that we need to feed back both the state and the parameter, the UKF can be utilized.

Appendix 1

Lemma L1

For any matrices X, Y with appropriate dimensions, for any positive constant μ, we have:

$$X^T Y + Y^T X \leq \mu X^T X + \frac{1}{\mu} Y^T Y$$

The lemma L1 is presented in [105].

Lemma L2

If we have the following matrices A, H, E, F where $FF^T \leq I$, X is a positive definite matrix and there exists arbitrary α that satisfies $\alpha^{-1}I - EXE^T > 0$, then the following inequality holds:

$$\left(A + HFE \right) X \left(A + HFE \right)^T \leq AXA^T + AXE^T \left(\alpha^{-1}I - EXE^T \right)^{-1} EXA^T + \alpha^{-1}HH^T$$

The lemma L2 is presented in [100].

Appendix 2

In this appendix, we present more simulation results of the disturbance accommodation Kalman filter proposed in Chapter 2. The results appear in the journal No. 1 in our publication list.

In this simulation, we verify the proposed Kalman filter in comparison with other estimation methods. As the simulation of the lane change test is shown in Chapter 5, in this Appendix we present the simulation results of the cornering test. The following driving conditions are set:

1) The longitudinal velocity is 25 km/h.

2) From 4 second, a strong lateral wind force starts to act on the vehicle. It introduces lateral force disturbance F_d and yaw moment disturbance N_d.

3) The cornering stiffness of vehicle model are $C_f = C_r = 7000$ N/rad. However, the estimation model is designed with the nominal values $C_{fn} = C_{rn} = 10,000$ N/rad. This means a big error is introduced to cornering stiffness of the estimation model.

4) The disturbance terms d_1 and d_2 are simulated using the following formulations:

$$d_1 = \frac{-2(\Delta C_f + \Delta C_r)}{mu_x}\beta + \frac{-2(\Delta C_f l_f - \Delta C_r l_r)}{mu_x^2}\gamma + \frac{2\Delta C_f}{mu_x}\delta_f + \frac{1}{mu_x}F_d$$

$$d_2 = \frac{-2(\Delta C_f l_f - \Delta C_r l_r)}{I_z}\beta + \frac{-2(\Delta C_f l_f^2 + \Delta C_r l_r^2)}{I_z u_x}\gamma + \frac{2\Delta C_f l_f}{I_z}\delta_f + \frac{1}{I_z}N_d$$

The disturbance accommodation multi-rate Kalman filter (DAMRKF) is compared to the following two methods. The first is the sideslip angle estimation using linear observer (LOB). Yaw rate and lateral acceleration are selected as output measurements. The second method is multi-rate Kalman filter (MRKF). This method uses the yaw rate and course angle as output measurement. These two methods are described in Chapter 5.

Simulation results are shown in Fig. 1 in the following page. The results include sideslip angle estimations and disturbance estimations. The influence of lateral wind force can be demonstrated by the change of sideslip angle and disturbance terms from 4 second. In both tests, LOB shows the poorest estimation performance. By using course angle from GPS, MRKF provides better estimation than LOB. However, the results degrade under the influence of both model error and lateral wind force. By using the proposed DAMRKF method, the disturbances are estimated as the extended states. Although the tracking of disturbance estimation is not perfect, sideslip angle estimation performance is improved considerably. Therefore, the assumption that the dynamics of disturbances is random-walk is acceptable.
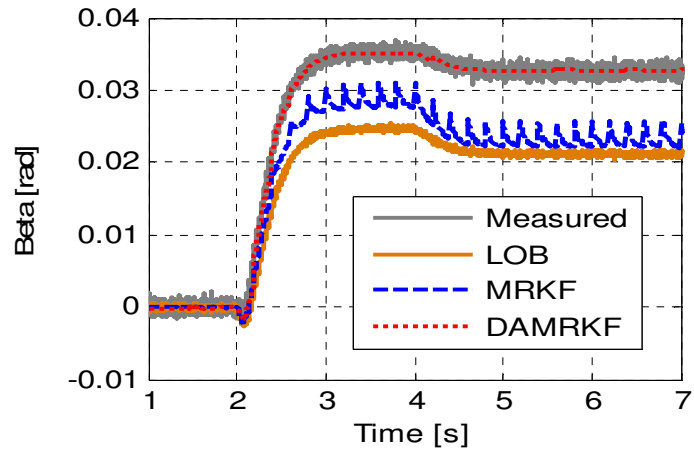
(a)
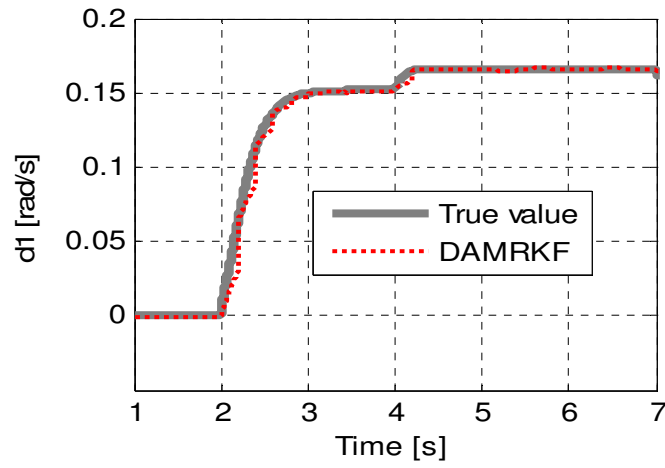
(b)
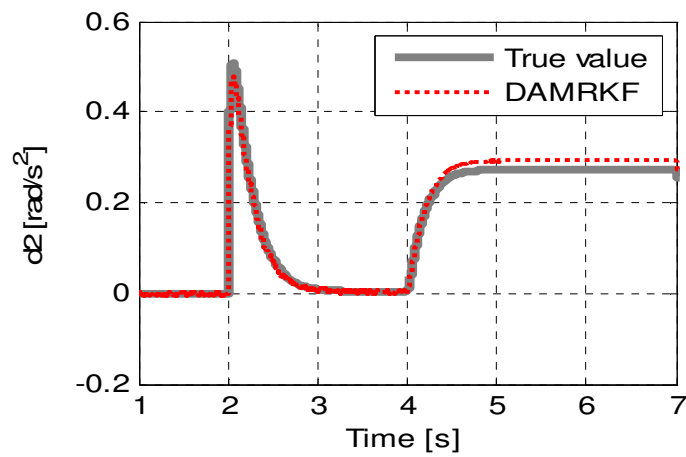
(c)

Fig. 1. Simulation results of sideslip angle estimation: *Cornering test*.

(a) Sideslip angle. (b). Disturbance term d_1. (c). Disturbance term d_2.

References

[1] H. S. Black: "Inventing the Negative Feedback Amplifier," *IEEE Spectrum*, vol. 14, pp. 54-60 (1977). (50th anniversary of Black's invention of negative feedback amplifier).

[2] K. K. Tan, T. H. Lee, and S. Huang: "Precision Motion Control: Design and Implementation," *Advances in Industrial Control*, Springer, 2nd edition (2008).

[3] History of motion control: http://www.a-m-c.com/university/history.html

[4] J. Fang, H. Li, and B. Han: "Torque Ripple Reduction in BLDC Torque Motor with Nonideal Back EMF," *IEEE Transactions on Power Electronics*, vol. 27, no. 11, pp. 4630-4637 (2012).

[5] J. S. Lawler, J. M. Bailey, J. W. McKeever, and J. Pinto, "Extending the Constant Power Speed Range of the Brushless DC Motor Through Dual-Mode Inverter Control," *IEEE Transactions on Power Electronics*, vol. 19, no. 3, pp. 783-793 (2004).

[6] K. Ohnishi, M. Shibata, and T. Murakami: "Motion Control for Advanced Mechatronics," IEEE/ASME Transactions on Mechatronics, vol. 1, no. 1, pp. 56-57 (1996).

[7] Y. Ochi, H. Kondo: "PID Controller Design Based on Optimal Servo and V-gap Metric," *Proceedings of American Control Conference*, pp. 1091-1096, 2010.

[8] Y. Oh and W. K. Chung: "Disturbance-observer-based Motion Control of Redundant Manipulators using Inertially Decoupled Dynamics," IEEE/ASME Transactions on Mechatronics, vol. 4, no. 2, pp. 133-146 (1999).

[9] F. J. Lin and P. H. Shen: "Robust Fuzzy Neural Network Sliding-mode Control for Two-axis Motion Control System," *IEEE Transactions on Industrial Electronics*, vol. 53, no. 4, pp. 1209-1225 (2006).

[10] B. M. Nguyen, Y. Wang, H. Fujimoto, and Y. Hori: "Sideslip angle Estimation using GPS and Disturbance Accommodating Multi-rate Kalman Filter for Electric Vehicle Stability Control," *Proceedings of Vehicle Power and Propulsion Conference*, pp. 1323-1328 (2012).

[11] G. Ellis: "Observer in control system: A practical guide," *Academic Press*, 1st edition (2002).

[12] R. E. Kalman: "A New Approach to Linear Filtering and Prediction Problems," *Transactions of the ASME-Journal of Basic Engineering*, vol. 82, series D, pp. 35-45 (1960).

[13] P. E. Moraal and J. W. Grizzle: "Observer Design for Nonlinear Systems with Discrete-time Measurements," *IEEE Transactions on Automatic Control*, vol. 40, no. 3, pp. 395-404 (1995).

[14] A. Benchaib, A. Rachid, E. Audrezet, and M. Tadjine: "Real-time Sliding-mode Observer and Control of an Induction Motor," *IEEE Transactions on Industrial Electronics*, vol. 46, no. 1, pp. 128-138 (1999).

[15] G. A. Einicke and L. B. White: "Robust Extended Kalman Filtering," *IEEE Transactions on Signal Processing*, vol. 47, no. 9, pp. 2596-2599 (1999).

[16] S. Särkkä: "On Unscented Kalman Filtering for State Estimation of Continuous-time Nonlinear

Systems," *IEEE Transactions on Automatic Control*, vol. 52, no. 9, pp. 1631-1641 (2007).

[17] J. Y. Wong: "Theory of Ground Vehicles," *Wiley*, 4th edition (2008).

[18] B. C. Chen and F. C. Hsieh: "Sideslip Angle Estimation using Extended Kalman Filter," *Vehicle System Dynamics*, vol. 46, no. 1, pp. 353-364 (2006).

[19] C. Geng, L. Mostefai, M. Denai, and Y. Hori: "Direct Yaw Moment Control of an In Wheel Motored Electric Vehicle Based on Body Slip Angle Fuzzy Observer," *IEEE Transactions on Industrial Electronics*, vol. 56, pp. 1411-1419 (2009).

[20] B. Wang, Q. Cheng, A. C. Victorino, and A. Charara: "Nonlinear Observer of Tire Forces and Sideslip Angle Estimation Applied to Road Safety: Simulation and Experimental Validation," *Proceedings of 15th International IEEE Conference on Intelligent Transportation Systems*, pp. 1333-1338 (2012).

[21] Z. Wu, M. Yao, H. Ma, and W. Jia: "Improving Accuracy of the Vehicle Attitude Estimation for low-cost INS/GPS Integration Aided by the GPS-measured Course Angle," *IEEE Transactions on intelligent transportation systems*, vol. 14, no. 2, pp. 553-564 (2013).

[22] D. M. Bevly, J. Ryu, and J. C. Gerdes: "Integrating INS Sensors with GPS Measurements for Continuous Estimation of Vehicle Sideslip, Roll, and Tire Cornering Stiffness," *IEEE Transactions on Intelligent Transportation System*, vol. 7, no. 4, pp. 483-493 (2006).

[23] H. Namie, K. Nishikawa, K. Sasano, C. Fan, and A. Yasuda: "Development of Network-based RTK-GPS Positioning System using FKP via a TV Broadcast in Japan," *IEEE Transactions on Broadcasting*, vol. 54, no. 1, pp. 106-111 (2008).

[24] R. Anderson and D. M. Bevly: "Using GPS with a Model-based Estimator to Estimate Critical Vehicle States," *Vehicle System Dynamics*, vol. 48, no. 12, pp. 1413-1438 (2010).

[25] K. Ito, B. M. Nguyen, Y. Wang, H. Fujimoto, Y. Hori, M. Odai, H. Ogawa, E. Takano, T. Inoue, and M. Koyama: "Fast and Accurate Vison-based Positioning Control Employing Multi-rate Kalman Filter," in *Proc. 39th Annual Conference of the IEEE Industrial Electronics Society (IECON)*, pp. 6466-6471 (2013).

[26] Y. He, Z. Ye, D. She, B. Mesman, and H. Corporaal: "Feasibility Analysis of Ultra High Frame Rate Visual Servoing on FPGA and SIMD Processor," *Proceedings of the Advanced Concepts for Intelligent Vision System*, pp. 623-634 (2011).

[27] H. Elliott and W. A. Wolovich: "Parameter Adaptive Identification and Control," *IEEE Transactions on Automatic Control*, vol. 24, no. 4, pp. 592-599 (1979).

[28] K. Nam, H. Fujimoto, and Y. Hori: "Lateral Stability Control of In-wheel-motor-driven Electric Vehicles Based on Sideslip Angle Estimation Using Lateral Tire Force Sensors," *IEEE Transactions on Vehicular Technology*, vol. 61, no. 5, pp. 1972-1984 (2012).

[29] H. Fujimoto, N. Takahashi, A. Tsumasaka, and T. Noguchi: "Motion Control of Electric Vehicle Based on Cornering Stiffness Estimation with Yaw-Moment Observer," *Proceedings of IEEE International Workshop on Advanced Motion Control*, pp. 206-211 (2006).

[30] Y. Hori: "Robust and Adaptive Control of a Servomotor Using Low Precision Shaft Encoder," *Proceedings of International Conference on Industrial Electronics, Control, and Instrumentation* (IECON 93), Vol. 1, pp. 73-38 (1993).

[31] L. Kovudhikulrungsri and T. Koseki: "Precise Speed Estimation from Low Resolution Encoder by Dual-Sampling-Rate Observer," *IEEE/ASME Transactions on Mechatronics*, Vol. 11, No. 6, pp. 661-670 (2006).

[32] M.-W. L. Thein and E. A. Misawa: "A Parallel Observer System for Multirate State Estimation," *Proceedings of American Control Conference*, vol. 6, pp. 3885-3889 (1999).

[33] M-W. L. Thein: "A Variable Structure Parallel Observer System for Robust State Estimation of Multirate System with Noise," Proceedings of 42nd IEEE Conference on Decision and Control, pp. 1303-1308 (2003).

[34] F. Ding and T. Chen: "Hierarchical Identification of Lifted State-Space Models for General Dual-Rate Systems," *IEEE Transactions on Circuits and Systems*, vol. 52, no. 6, pp. 1179-1187 (2005).

[35] W. Li and S. Shah: "Data-driven Kalman Filters for Non-uniformly Sampled Multirate System with Applications to Fault Diagnosis," *Proceedings of the 2005 American Control Conference*, vol. 4, pp. 2768-2772 (2005).

[36] J. Sheng, T. Chen, and S. L. Shah: "Optimal Filtering for Multirate Systems," *IEEE Transactions on Circuits and Systems-II; Express Briefs*, vol. 52, no. 4, pp. 228-232 (2005).

[37] T. Hara and M. Tomizuka: "Performance Enhancement of Multi-rate controller for Hard Disk Drives," *IEEE Transactions on Magnetics*, Vol. 35, No. 2, pp. 3033-3037 (1999).

[38] S. Oh and Y. Hori: "Development of a Novel Instantaneous Speed Observer and its Application to the Power-Assisted Wheelchair Control," *Proceedings of the 4th International Conference on Power Electronics and Motion Control Conference*, Vol. 3, pp. 1471-1476 (2004).

[39] B. M. Nguyen, Y. Wang, S. Oh, H. Fujimoto, and Y. Hori: "GPS Based Estimation of Vehicle Sideslip Angle Using Multi-rate Kalman Filter with Prediction of Course Angle Measurement Residual," *Proc. of the FISITA 2012 World Automotive Congress*, pp. 597-609 (2012).

[40] H. P. Rotstein: "Optimal Filtering with Delayed and Non-Delayed Measurements," *Proceedings of 15th IFAC World Congress* (2002).

[41] F. H. Hsiao and S. T. Pan: "Robust Kalman Filter Synthesis for Uncertain Multiple Time-Delay Stochastic Systems," *Journal of Dynamic Systems, Measurement, and Control*, vol. 118, no. 4, pp. 803-808 (1996).

[42] E. Kaszkurewicz and A. Bhaya: "Discrete-time State Estimation with Two Counters and Measurement Delay," 35th IEEE CDC, vol. 2, pp. 1472-1476 (1996).

[43] M. Choi, J. Choi, W. K. Chung: "State Estimation with Delayed Measurements Incorporating Time-Delay Uncertainty," *IET Control Theory and Applications*, vol. 6, no. 15, pp. 2351-2361 (2012).

[44] T. D. Larsen, N. A. Andersen, and O. Ravn: "Incorporation of Time Delayed Measurements in a

Discrete-Time Kalman Filter," *Proceedings of the 37th IEEE Conference on Decision and Control*, pp. 3972-3977 (1998).

[45] J-H. Yoon and H. Peng: "Sideslip Angle Estimation Based on GPS and Magnetometer Measurements," *Proceedings of 11th Intertional Symposium on Advanced Vehicle Control*, Seoul, Korea (2012).

[46] H. Zhang, X. Lu, and D. Cheng: "Optimal Estimation for Continuous-Time Systems with Delayed Measurements," *IEEE Transactions on Automatic Control*, vol. 51, no. 5, pp. 823-827 (2005).

[47] X. Lu, H. Zhang, W. Wang, and K-L. Teo: "Kalman Filtering for Multiple Time-Delay Systems," *Automatica*, vol. 41, no. 8, pp. 1455-1461 (2005).

[48] X. Lu, H. Zhang, H. Wang, W. Wang, and L. Xie: "Kalman Filtering for Continuous-Time Systems with Multiple Delayed Measurements," *IET Signal Processing*, vol. 2, no. 1, pp. 37-46 (2008).

[49] H. Zhang, G. Feng, G. Duan, and X. Lu: "H∞ Filtering for Multiple-Time-Delay Measurements," *IEEE Transactions on Signal Processing*, vol. 54, no. 5, pp. 1681-1688 (2005).

[50] N. Kazantzis and R. A. Wright: "Nonlinear Observer Design in the Presence of Delayed Output Measurements," *Systems & Control Letters*, vol. 54, no. 9, pp. 877-886 (2005).

[51] A. Gopalakrishnan, N. S. Kaisare, and S. Narasimhan: "Incorporating Delayed and Infrequent Measurements in Extended Kalman Filter Based Nonlinear State Estimation," *Journal of Process Control*, vol. 21, no. 1, pp. 119-129 (2011).

[52] M. Schultze and J. Horn: "State Estimation for PEM Fuel Cell Systems with Time Delay by an Unscented Kalman Filter and Predictor Strategy," *Proceedings of 21st Mediterranean Conference on Control & Automation*, pp. 104-112 (2013).

[53] X. Lu, L. Xie, H. Zhang, and W. Wang: "Robust Kalman Filtering for Discrete-Time Systems with Measurement Delay," *IEEE Transactions on Circuits and Systems-II; Express Briefs*, vol. 54, no. 6, pp. 522-526 (2007).

[54] Robust H-infinity Filtering for Time-Delay Systems with Missing Measurements: A Parameter-Dependent Approach," *Journal of Control Theory and Applications*, vol. 5, no. 4, pp. 336-344 (2007).

[55] M. Choi, J. Choi, J. Park, and W. K. Chung: "State Estimation with Delayed Measurements Considering Uncertainty of Time Delay," *Proceedings of IEEE Conference on Robotics and Automation*, pp. 3987-3992 (2009).

[56] B. Chen, L. Yu, W. A. Zhang: "Robust Kalman Filtering for Uncertain State Delay Systems with Random Observervation Delay and Missing Measurements," *IET Control Theory and Applications*, vol. 5, no. 17, pp. 1945-1954 (2011).

[57] Y. Hori: "Future Vehicle Driven By Electricity and Control-Research on 4 Wheel Motored UOT March II," *IEEE Transactions on Industrial Electronics*, vol. 51, no. 5, pp. 954-962 (2004).

[58] K. Furukawa and Y. Hori: "Recent Development of Road Condition Estimation Techniques for

Electric Vehicle and Their Experimental Evaluation Using the Test EV UOT March I and II," *Proceedings of 29th IEEE Annual Conference on Industrial Electronics*, pp. 925-930 (2003).

[59] H. Fujimoto, A. Tsumasaka, and T. Noguchi: "Direct Yaw Moment Control of Electric Vehicle Based on Cornering Stiffness Estimation," *Proceedings of 31st IEEE Annual Conference on Industrial Electronics*, pp. 2626-2631 (2005).

[60] H. Eric Tseng, L. Xu, and D. Hrovat: "Estimation of Land Vehicle Roll and Pitch Angle," *Vehicle System Dynamics*, vol. 45, no. 5, pp. 433-443 (2007).

[61] J. Kosecka, R. Blasi, C. J. Taylor, and J. Malik: "Vision Based Lateral Control of Vehicles," *Proceedings of IEEE Conference on Intelligent Transportation System*, pp. 900-905 (1997).

[62] A. J. Tuononen: "Vehicle Lateral State Estimation Based on Measured Tire Forces," *Sensors*, vol. 9, no. 11, pp. 8761-8775 (2009).

[63] Japan's Strategic Headquarters for Space Policy: "Future Plan of Quasi-Zenith Satellite System," (http://www.unoosa.org/pdf/sap/2012/un-latvia/ppt/1-3.pdf).

[64] Y. Hori, Y. Toyoda, and Y. Tsuruoka: "Traction Control of Electric Vehicle: Basic Experimental Results Using the Test EV 'UOT Electric March'," *IEEE Transactions on Industry Applications*, vol. 34, no. 5, pp. 1131-1138 (1998).

[65] H. Fujimoto and Y. Yamauchi: "Advanced Motion Control of Electric Vehicle Based on Lateral Force Observer with Active Steering," *Proceedings of IEEE International Symposium on Industrial Electronics*, pp. 3627-3632 (2010).

[66] L. Xu and H. Eric Tseng: "Robust Model-Based Fault Detection for a Roll Stability Control System," *IEEE Transactions on Control System Technology*, vol. 15, no. 3, pp. 519-528 (2007).

[67] S. Sato and H. Fujimoto: "Proposal of Pitching Control Method Based on Slip-Ratio Control for Electric Vehicle," *Proceedings of 34th IEEE Annual Conference on Industrial Electronics*, pp. 2823-2828 (2008).

[68] K. Maeda, H. Fujimoto, and Y. Hori: "Four-wheel Driving-force Distribution Method for Instantaneous or Split Slippery Roads for Electric Vehicle," *Automatika-Journal for Control, Measurement, Electronics, Computing and Communications*, vol. 54, no. 1, pp. 103-113 (2013).

[69] H. Fujimoto and H. Sumiya: "Range Extension Control System of Electric Vehicle Based on Optimal Torque Distribution and Cornering Resistance Minimization," *Proceedings of 37th IEEE Annual Conference on Industrial Electronics*, pp. 3858-3863 (2011).

[70] B. M. Nguyen, V. Alexander, H. Fujimoto, and Y. Hori: "Basic Design of Electric Vehicle Motion Control System Using Single Antenna GPS Receiver," *Proceedings of 7th IFAC Symposium on Advances in Automotive Control*, pp. 612-619 (2013).

[71] M. Abe: "Vehicle Handling Dynamics," *Published by Elsevier Ltd.* (2009).

[72] E. Bakker, L. Nyborg, and H. B. Pacejka: "Tyre Modelling for Use in Vehicle Dynamics Studies," *SAE Technical Paper*, no. 870421 (1987).

[73] D. N. Piyabongkarn, R. Rajamani, J. A. Grogg, and J. Y. Lew: "Development and Experimental

Evaluation of Slip Angle Estimator for Vehicle Stability control," *IEEE Transactions on Control Sysem Techno*logy, vol. 17, no. 1, pp. 78-88 (2009).

[74] L. Imsland, T. A. Johansen, T. I. Fossen, H. F. Grip, J. C. Kalkkuhl, and A. Suissa: "Vehicle Velocity Estimation Using Nonlinear Observer," *Automatica*, vol. 42, no.12, pp. 2091-2103 (2006).

[75] J. Stephant, A. Charara, and D. Meizei: "Evaluation of a Sliding Mode Observer for Vehicle Sideslip Angle," *Control of Engineering Practice*, vol. 15, no. 7, pp. 803-812 (2007).

[76] Y. Aoki, Z. Li, and Y. Hori: "Robust Design of Body Slip Angle Observer with Cornering Stiffness Power Identification at Each Tire for Vehicle Motion Stabilization," *Proceedings of 9th IEEE Workshop on Advanced Motion Control*, pp. 590-595 (2006).

[77] Y. Wang, B. M. Nguyen, H. Fujimoto, and Y. Hori: "Multirate Estimation and Control of Body Slip Angle for Electric Vehicles Based on Onboard Vision System," *IEEE Transactions on Industrial Electronics*, vol. 61, no. 2, pp. 1133-1143 (2014).

[78] K. Nam, S. Oh, H. Fujimoto, and Y. Hori: "Estimation of sideslip and roll angles for electric vehicles using lateral tire force sensors through RLS and Kalman filter approaches," *IEEE Transactions on Industrial Electronics,* vol. 60, no. 3, pp. 988-1000 (2013).

[79] D. M. Bevly: "Global Positioning System (GPS): A Low-cost Velocity Sensor for Correcting Inertial Sensor Errors on Ground Vehicles," *Trans. ASME, Journal of Dynamics, System, Measurement and Control*, vol. 126, no. 2, pp. 255-264 (2004).

[80] J. Ryu, E. J. Rossetter, and J. C. Gerdes: "Vehicle Sideslip and Roll Parameter Estimation Using GPS," *Proceedings of 6th International Symposium on Advanced Vehicle Control*, pp. 1–8 (2002).

[81] J. H. Yoon and H. Peng: "Robust Vehicle Sideslip Angle Estimation Through a Disturbance Rejection Filter that Integrates a Magnetometer with GPS," *IEEE Transactions on Intelligent Transportation System*, vol. 15, no. 1, pp. 191-204 (2014).

[82] D. M. Bevly, J. C. Gerdes, and C. Wilson: "The Use of GPS Based Velocity Measurements for Measurement of Sideslip and Wheel slip," *Vehicle System Dynamics*, vol. 38, no. 2, pp. 127–147 (2003).

[83] C. D. Johnson: "Accommodation of External Disturbances in Linear Regulator and Servomechanism Problems," *IEEE Transactions on Automatic Control*, vol. 16, no. 6, pp. 635-644 (1971).

[84] J. George, P. Singla, and J. L. Crassidis: "Stochastic Disturbance Accommodating Control Using a Kalman Estimator," *Proceedings of the AIAA Guidance, Navigation and Control Conference and Exhibit* (2008).

[85] S. Suzuki: "Autonomous Navigation, Guidance and Control of Small 4-wheel Electric Vehicle," *Journal of Asian Electric Vehicles*, vol. 10, no. 1, pp.1575-1582 (2012).

[86] J. Connors and G. H. Elkaim: "Trajectory Generation and Control Methodology for an Autonomous Ground Vehicle," *Proceedings of AIAA Guidance, Navigation, and Control Conference and Exhibit*, vol. 8, pp.5704-5722 (2008).

[87] G. V. Raffo, G. K. Gomes, J. E. Normey-Rico, C. R. Kelber, and L. B. Becker: "A predictive Controller for Autonomous Vehicle Path Tracking," *IEEE Transactions on Intelligent Transportation System*, vol. 10, vo. 1, pp. 92-102 (2009).

[88] J. Kang, R. Y. Hindiyeh, S. W. Moon, J. C. Gerdes, and K. Yi: "Design and Testing of a Controller for Autonomous Vehicle Path Tracking Using GPS/INS Sensors," *Proceedings of 17th World Congress-The International Federation of Automatic Control*, pp. 2093-2098 (2008).

[89] T. Keviczky, P. Kalcone, F. Borrelli, J. Asgari, and D. Hrovat: "Predictive Control Approach to Autonomous Vehicle Steering," *Proceedings of the 2006 American Control Conference*, p.4670-4675 (2006).

[90] R. W. Wall, J. Bennett, and G. Eis: "Creating a Low-cost Autonomous Vehicle," *Proceedings of 28th Annual Conference of the Industrial Electronics Society*, vol. 4, pp.3112-3116 (2002).

[91] M. E. Holden: "Low-Cost Autonomous Vehicles Using Just GPS," *Proceedings of the 2004 American Society for Engineering Education Annual Conference & Exposition* (2004).

[92] W. Travis and D. M. Bevly: "Trajectory Duplication Using Relative Position Information for Automated Ground Vehicle Convoys," *Proceedings of IEEE Position, Location and Navigation Symposium*, pp.1022-1032 (2008).

[93] H. Suppachai, C. Silawatchananai, M. Parnichkun, and C. Wuthishungwong: "Double Loop Controller Design for the Vehicle's Heading Control," *Proceedings of the 2009 IEEE International Conference on Robotics and Biometrics*, pp.989-994 (2009).

[94] A. D. Luca and G. Oriolo: "Feedback Control of a Nonholonomic Car-like Robot," Chapter 4 of Planning Robot Motion, J. P. Laumond Ed., Springer-Verlag (1997).

[95] K. Ohnishi: "A New Servo Method in Mechatronics," *Transactions of Japanese Society of Electrical Engineers*, vol. 107-D, pp.83-86 (1987).

[96] Y. Shirai and H. Inoue: "Guiding a Robot by Visual Feedback in Assembling Tasks," *Pattern Recognit*, vol. 5, pp. 99-108 (1973).

[97] I. R. Petersen and D. C. McFarlane: "Robust State Estimation for Uncertain Systems," *Proceedings of the 30th IEEE Conference on Decision and Control, Brighton,* vol. *3,* pp. 2630–2631 (1991).

[98] I. R. Petersen and D. C. McFarlane: "Optimal Guaranteed Cost Filtering for Uncertain Discrete Time Systems," *International Journal of Robust and Nonlinear Control*, vol. 6, no. 4, pp. 267–280 (1996).

[99] S. M. K. Mohamed and S. Nahavandi: "Robust Finite-Horizon Kalman Filtering for Uncertain Discrete-time Systems," *IEEE Transactions on Automatic Control*, vol. 57, no. 6, pp. 1548-1552 (2012).

[100] L. Xie, Y. C. Soh, and C. E. de Souza: "Robust Kalman Filtering for Uncertain Discrete-time Systems," *IEEE Transactions on Automatic Control*, vol. 39, no. 6, pp. 1310-1314 (1994).

[101] J. V. Candy: "Bayesian Signal Processing: Classical, Modern, and Particle Filtering Methods," *A

John Wiley & Sons, Inc., Publication (2009).

[102] J. L. Crassidis and J. L. Junkins: "Optimal Estimation of Dynamic Systems," *CRC Press*, *Taylor & Francis Group*, LLC, 2nd Edition (2012).

[103] S. J. Julier, J. K. Uhlmann, and H. F. Durrant-Whyte: "A New Approach for the Nonlinear Transformation of Means and Covariances in Filters and Estimators," *IEEE Transactions on Automatic Control*, vol. 45, no. 3, pp. 477-482 (2000).

[104] S. J. Julier, J. K. Uhlmann, and H. F. Durrant-Whyte: "A New Approach for Filtering Nonlinear Systems," *Proceedings of the American Control Conference*, pp. 1628-1632 (1995).

[105] M. S. Mahmoud: "Robust Control and Filtering for Time-Delay System," *Control Engineering Series*, Marcel Dekker, Inc., ISBN 0-8247-0327-8 (2007).

[106] Y. Hori: "High Performance Control of Servomotors with Low Precision Shaft Encoder Using Instantaneous Speed Observer and Adaptive Identification of Inertia Moment," *Proceedings of Asia-Pacific Workshop on Advances in Motion Control*, pp. 7-12 (1993).

[107] H. Fujimoto, Y. Hori, and A. Kawamura: "Perfect Tracking Control based on Multirate Feedforward Control with Generalized Sampling Periods," *IEEE Transactions on Industrial Electronics*, vol. 48, no. 3, pp. 636-644 (2001).

[108] H. Fujimoto and Y. Hori: "High Speed Robust Visual Servoing based on Intersample Estimation and Multirate Control," *Proceedings of the 7th IEEE International Workshop on Advanced Motion Control*, pp. 104-109 (2002).

[109] H. Fujimoto and Y. Hori: "Visual Servoing Based on Intersample Disturbance Rejection by Multirate Sampling Control – Time Delay Compensation and Experimental Verification," *Proceedings of the 40th IEEE Conference on Decision and Control*, vol. 1, pp. 334-339 (2001).

[110] H. Fujimoto: "General Framework of Multirate Sampling Control and Applications to Motion Control Systems," PhD Thesis, the University of Tokyo (2000).

[111] J. B. Rawlings and D. Q. Mayne: "Model Predictive Control: Theory and Design," Nob Hill Publishing, LLC (2009).

[112] L. D. Rei, F. Allgoewer, L. Glielmo, and C. Guardiola: "Automotive Model Predictive Control: Models, Methods and Applications," *Lecture Notes in Control and Information Sciences*, Springer London (2010).

[113] P. O. M. Scokaert, D. Q. Mayne, and J. B. Rawlings: "Suboptimal Model Predictive Control (Feasibility Implies Stability)," *IEEE Transactions on Automatic Control*, vol. 44, no. 3, pp. 648-654 (1999).

[114] J. H. Lee and N. L. Ricker: "Extended Kalman Filter Based Nonlinear Model Predictive Control," *Proceedings of the American Control Conference*, pp. 1895-1899 (1993).

[115] S. Rezvanian, F. Towhidkhah, and N. Ghahramani: "Controlling the Depth of Anesthesia Using Model Predictive Controller and Extended Kalman Filter," *Proceedings of the 1st Middle East Conference on Biomedical Engineering*, pp. 213-216 (2011).

[116] S. Roshany-Yamchi, M. Cychowski, R. R. Negenborn, B. De Schutter, K. Delaney, and J. Connell: "Kalman Filter-Based Distributed Predictive Control of Large-Scale Multi-Rate Systems: Application to Power Networks," *IEEE Transactions on Control System Technology*, vol. 21, no. 1, pp. 27-39 (2011).

[117] M. Sauvee, P. Poignet, E. Dombre, and E. Courtial: "Image Based Visual Servoing through Nonlinear Model Predictive Control," *Proceedings of the 45th IEEE Conference on Decision and Control*, pp. 1776-1781 (2006).

[118] S. Heshmati-Alamdari, A. Eqtami, G. C. Karras, D. V. Dimarogonas, and K. J. Kyriakopoulos: "A Self-Triggered Visual Servoing Model Predictive Control Scheme for Under-Actuated Underwater Robotic Vehicles," *Proceedings of the IEEE International Conference on Robotics and Automation*, pp. 3826-3831 (2014).

[119] K. Natori and K. Ohnishi: "A Design Method of Communication Disturbance Observer for Time-Delay Compensation, Taking the Dynamic Property of Network Disturbance Into Account," *IEEE Transactions on Industrial Electronics*, vol. 55, no. 5, pp. 2152-2168 (2008).

Publication

Journal

Published journal

[1] **B. M. Nguyen**, Y. Wang, H. Fujimoto, and Y. Hori: "Lateral Stability Control of Electric Vehicle Based on Disturbance Accommodating Kalman Filter Using the Integration of Single Antenna GPS Receiver and Yaw Rate Sensor," *Journal of Electrical Engineering & Technology*, vol. 8, no. 4, pp. 899-910 (2013).

Co-authored journal

[2] Y. Wang, **B. M. Nguyen**, H. Fujimoto, and Y. Hori, "Multi-rate Estimation and Control of Body Slip Angle for Electric Vehicles based on On-board Vision System," *IEEE Transactions on Industrial Electronics,* vol. 61, no.2, pp. 1133-1143 (2014).

[3] Y. Wang, **B. M. Nguyen**, P. Kotchapansompote, H. Fujimoto, and Y. Hori: "Image-Processing-Based State Estimation for Vehicle Lateral Control Using Multi-rate Kalman Filter," *Recent Patent on Signal Processing*, vol. 2, no. 2, pp. 140-148 (2012).

Being prepared journal

[4] **B. M. Nguyen**, H. Fujimoto, and Y. Hori: "Upper-bound based Discrete-time Filter Considering Delayed Measurement," *IEEE Transaction on Automatic Control.*

Conference

[5] **B. M. Nguyen**, Y. Wang, H. Fujimoto, and Y. Hori: "Sideslip Angle Estimation Using GPS and Disturbance Accommodating Multi-rate Kalman Filter for Electric Vehicle Stability Control," *Proc. of Vehicle Power and Propulsion Conference*, pp. 1323-1328 (2012).

[6] **B. M. Nguyen**, Y. Wang, S. Oh, H. Fujimoto, and Y. Hori: "GPS Based Estimation of Vehicle Sideslip Angle Using Multi-rate Kalman Filter with Prediction of Course Angle Measurement Residual," *Proc. of the FISITA 2012 World Automotive Congress*, pp. 597-609 (2012).

[7] **B. M. Nguyen**, Y. Wang, H. Fujimoto, and Y. Hori: "Electric Vehicle Stability Control Based on Disturbance Accommodating Kalman Filter Using GPS," *Proc. 2013 IEEE International Conference on Mechatronics*, pp. 382-387 (2013).

[8] **B. M. Nguyen**, V. Alexander, H. Fujimoto, and Y. Hori: "Advanced Multi-rate Kalman Filter for Double Layer State Estimator of Electric Vehicle Based on Single Antenna GPS and Dynamic Sensor," *Proc. 6th IFAC Symposium on Mechatronic Systems*, pp. 437-444 (2013).

[9] **B. M. Nguyen**, H. Fujimoto, and Y. Hori: "Active Safety Control of Electric Vehicle Based on the Fusion of GPS Receiver and Dynamic Sensor," *Proc. 2nd International Symposium on Future Active Safety Technology (FAST-zero'13)* (2013).

[10] **B. M. Nguyen**, V. Alexander, H. Fujimoto, and Y. Hori: "Basic Design of Electric Vehicle Motion Control System Using Single Antenna GPS Receiver," *Proc. 7th IFAC Symposium on Advances in Automotive Control*, pp. 612-619 (2013).

[11] **B. M. Nguyen**, H. Fujimoto, and Y. Hori: "A Framework of Autonomous Electric Vehicle with Advanced Motion Control based on the Integration of GPS Receiver and On-board Dynamic Sensors," *Proc. 20th Intelligent Transportation System (ITS) World Congress* (2013).

[12] **B. M. Nguyen**, K. Ito, W. Ohnishi, Y. Wang, H. Fujimoto, Y. Hori, M. Odai, H. Ogawa, E. Takano, T. Inoue, and M. Koyama: "Dual Rate Kalman Filter Considering Delayed Measurement and Its Application in Visual Servo," *Proc. of 13th International Workshop on Advanced Motion Control*, pp. 494-499, (2014).

[13] **B. M. Nguyen**, H. Fujimoto, and Y. Hori: "Enhancement of Dual-Rate Estimation and Its Application Demonstration," *Proc. 19th IFAC World Congress*, pp. 11728-11733 (2014).

[14] **B. M. Nguyen**, H. Fujimoto, and Y. Hori: "Fusion of Large-Time-Delayed Measurement with Non-Delayed Measurement Based on Norm-Bound Method," *Accepted to 2015 IEEE International Conference on Mechatronics* (2015).

Co-authored conference

[15] Y. Wang, **B. M. Nguyen**, P. Kotchapansompote, H. Fujimoto, and Y. Hori: "Vision-Based Vehicle Body Slip Angle Estimation with Multi-rate Kalman Filter Considering Time Delay," *Proc. 2012 IEEE International Symposium on Industrial Electronics*, pp. 1506-1511 (2012).

[16] Y. Wang, **B. M. Nguyen**, H. Fujimoto, and Y. Hori: "Multi-rate Kalman Filter Design for Electric Vehicles Control based on Onboard Vision System with Uneven Time Delay," *Proc. 6th IFAC Symposium on Mechatronic Systems*, " pp. 431-436, (2013).

[17] Y. Wang, **B. M. Nguyen**, H. Fujimoto, and Y. Hori: "Vision-based Integrated Lateral Control System for Electric Vehicles Considering Multi-rate and Measurement Uneven Time Delay," *Proc. IEEE International Symposium on Industrial Electronics*, pp. 1-6 (2013).

[18] K. Ito, **B. M. Nguyen**, Y. Wang, H. Fujimoto, Y. Hori, M. Odai, H. Ogawa, E. Takano, T. Inoue, and M. Koyama: "Fast and Accurate Vison-based Positioning Control Employing Multi-rate Kalman Filter," in *Proc. 39th Annual Conference of the IEEE Industrial Electronics Society (IECON)*, pp. 6466-6471 (2013).

[19] M. Galvani, F. Biral, **B. M. Nguyen**, and H. Fujimoto: "Four Wheel Optimal Autonomous Steering for Improving Safety in Emergency Collision Avoidance Manoeuvres," *Proc. of IEEE 13th International Workshop on Advanced Motion Control*, pp. 362-367 (2014).

[20] P. Sukpraset, **B. M. Nguyen**, and H. Fujimoto: "Estimation of Lateral Displacement of Electrical Vehicle to An Alignment of Wireless Power Transmitters," *Proc. IEE of Japan Industry Applications Society Conference* (2014).

[21] P. Sukpraset, **B. M. Nguyen**, and H. Fujimoto: "Estimation of Lateral Displacement of Electric Vehicle to Wireless Power Transmitter in Dynamic Charging Scenario," *Accepted to present at the*

*2014 IEEE/SICE International Symposium on System Integration* (2014).

[22] P. Sukpraset, **B. M. Nguyen**, and H. Fujimoto: "Estimation and Control of Lateral Displacement of Electric Vehicle Using WPT Information," *Accepted to the IEEE International Conference on Mechatronics* (2015).

Achievement

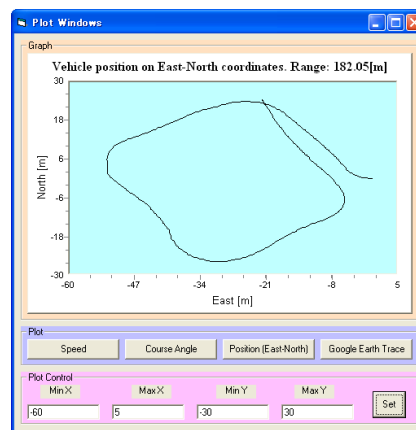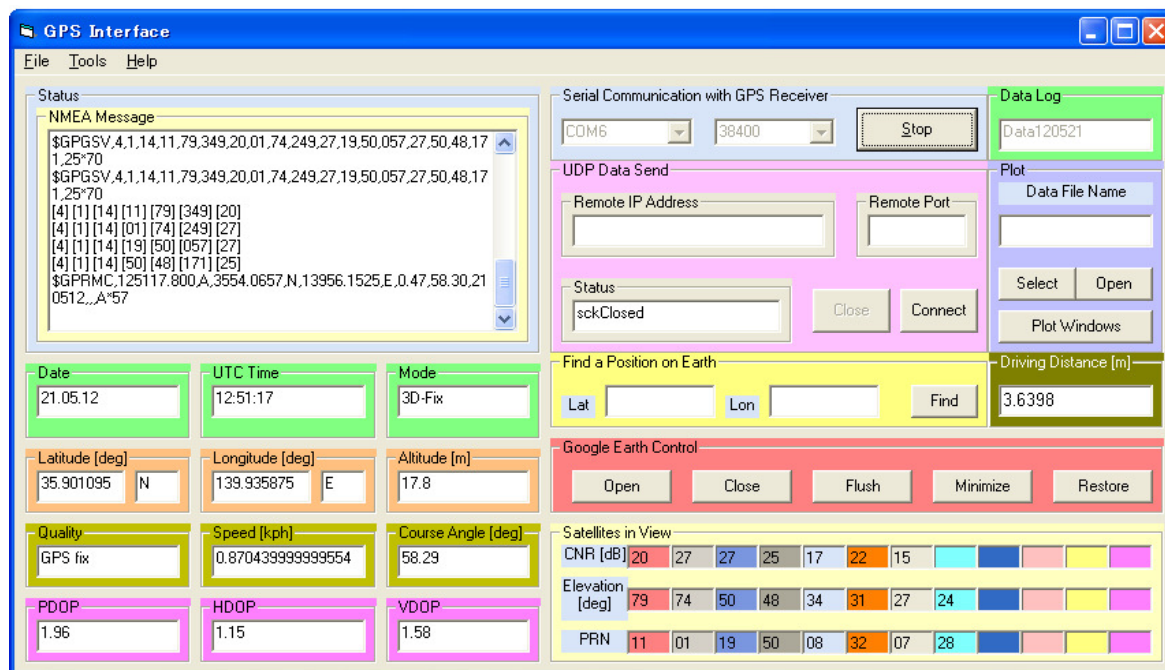1. **Paper Award (The 8th IEEE Vehicle Power and Propulsion Conference)**

2. **A Patent on Visual servo control for chip mounting machine (submitted)**
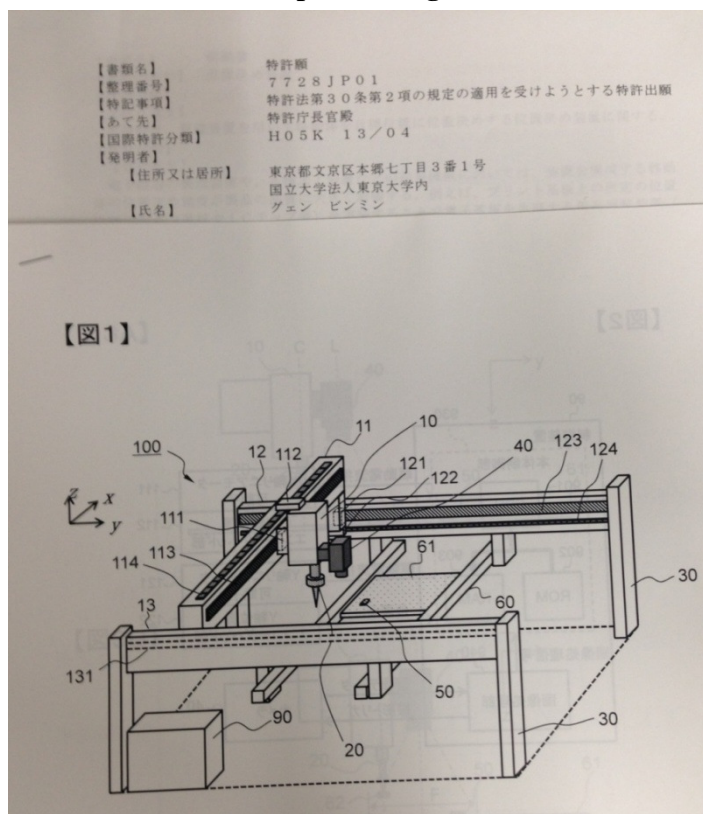
Practical Application

1. **GPS Interface Software**

Memory Photo

Photo 1: On the experimental electric vehicle COMS used in this study (Winter 2011).

Photo 2: With my supervisors and EV team members at Hori – Fujimoto Lab (Winter 2011).

Photo 3: Preparing the experiment beside the garage (Spring 2012). The vehicle is placed on four load sensors which are used to measure the weight (at each wheel) of the vehicle. By this way, we can find the center of gravity of the vehicle.
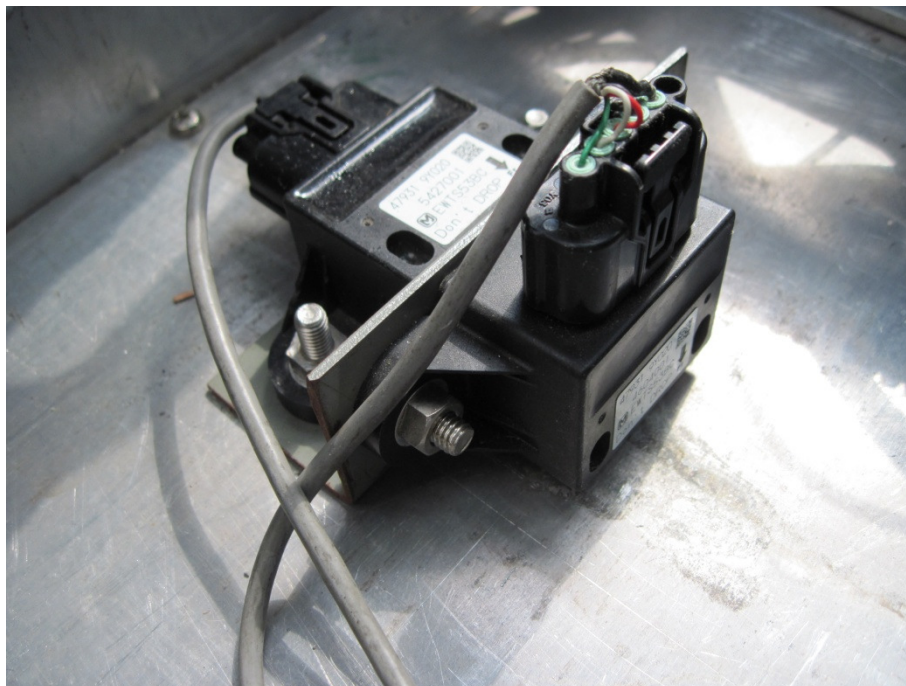

Photo 4: Inertial measurement unit place at the center of gravity of the vehicle.
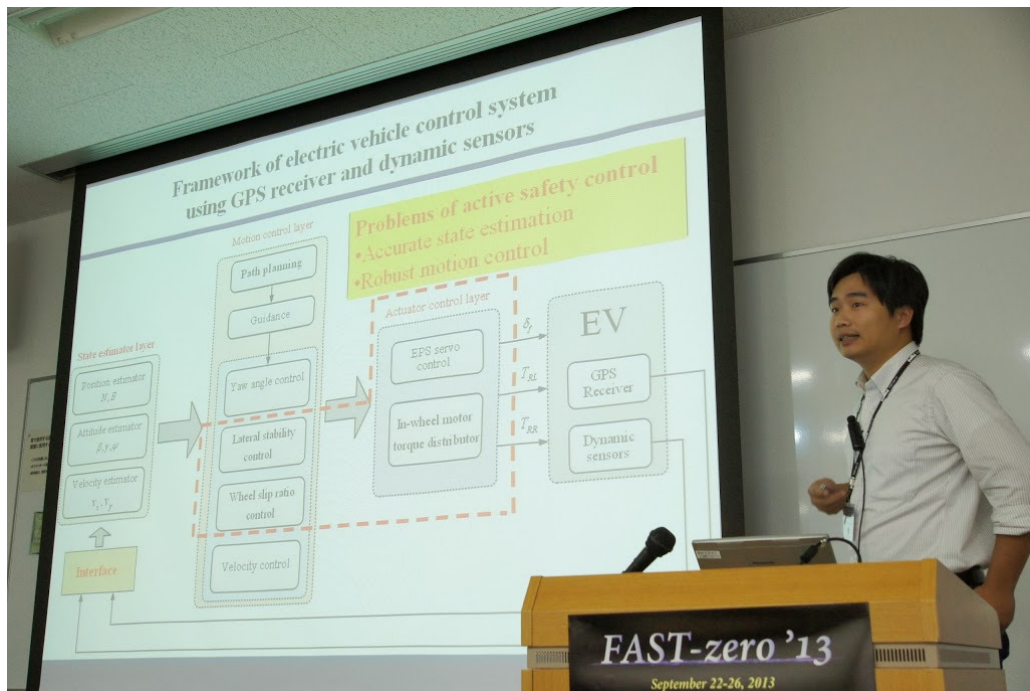
Photo 5: Presenting my research at FAST-zero (Summer 2013).

Photo 6: Trying the driving simulator at Zhejiang University, China (Spring 2013).

Photo 7: With 2014 Honda Prize Laureate, Dr. Clemens. He is famous for inventing new materials applied to engine design. Say thanks to him if you are using eco-technology car or flight (Winter 2014).

Photo 8: With Professor J. Christian Gerdes (Stanford University) at the 7th IFAC Symposium on Advances in Automatic Control. Gerdes is researching on autonomous vehicle and application of GPS in automotive control.

Curriculum Vitae

Nguyen Binh Minh was born in Hai Phong, Viet Nam on February 23, 1984. He received B. S. Degree in Electrical Engineering from Hanoi University of Science and Technology in the Autumn of 2007. In the Spring of 2009, he received the scholarship from Panasonic Corporation to study in Japan. After one year studying as research student, in the Spring of 2010, he entered the Graduate School of the University of Tokyo in pursuit of the Master's Degree in Electrical Engineering, and then Doctor of Science in Advanced Energy. His research interests are state estimation theory and its applications to motion control, such as electric vehicles, visual servo system, etc.